# Substrate Integrated Waveguide (SIW) and Superconducting Filters

by

Armin Smajevic

A thesis

presented to the University of Waterloo

in fulfillment of the

thesis requirement for the degree of

Master of Applied Science

in

Electrical and Computer Engineering

Waterloo, Ontario, Canada, 2022

## Author's Declaration

I hereby declare that I am the sole author of this thesis. This is a true copy of the thesis, including any required final revisions, as accepted by my examiners.

I understand that my thesis may be made electronically available to the public.

## Abstract

Substrate integrated waveguides (SIW) provide an excellent compromise between size and loss reduction for applications in planar circuits. SIW filters provide a better Q-factor than microstrip filters and a significant reduction in size compared to waveguide filters. The use of multi-band filters has become increasingly more common because they provide the opportunity to reduce the total footprint in both RF transmitters and receivers. This thesis investigates the design process of a single-band quasi-elliptic and dual-band SIW filter. We use several methods to design the single-band SIW, and compare the simulated results of each. These filters are designed on 0.508mm thick Rogers4003C substrate, fabricated, and measured.

The introduction of negative cross-coupling in SIW structures is achieved by using etched coplanar waveguide (CPW) lines. This negative cross-coupling allows for the introduction of transmission zeros in both designed filters. We carefully investigate the transition technology to ensure that we achieve a wideband match between microstrip and SIW. The thickness of the substrate provides some challenges in the matching, so we take extra consideration to overcome this.

The second part of this thesis explores the design of lumped element superconducting bandpass filters. When designing filters in the kHz and MHz range, several challenges arise.

The first is the ability to use certain software: Sonnet and HFSS both have a limited ability to simulate low-frequency components. More specifically, Sonnet demonstrates an inability to accurately simulate inductors, while simulation times in HFSS are prohibitively long. Momentum thus proves to be the best EM simulator for this task. The second challenge is the need to miniaturize these filters. At such low frequencies, the filter's footprint is quite large, therefore the reduction in size is extremely important. We implement traditional methods, such as stacked spiral inductors and vertically integrated capacitors, and achieve further size reduction by modifying the circuit topology to reduce the components with the largest footprints. We also introduce transmission zeros to improve the upper and lower band rejection. We then design a three-pole classical Chebyshev filter and a three-pole quasi-elliptic filter that uses a miniaturized circuit topology.

Finally, we design a 10% six-pole superconducting slotline resonator filter. Slotline resonators provide an excellent quality factor, even at higher frequencies. A CPW-to-slotline transition is implemented so that the device can be measured using a ground-signal-ground probe. The resonators implemented use dual-spiral inductors and interdigital capacitors. This allows for flexibility when choosing the resonant frequency.

All superconducting filters are fabricated using the MIT-Lincoln Lab (MIT-LL) multilayer niobium fabrication process.

**Acknowledgements**

I would like to thank Professor Raafat R. Mansour for accepting me as an MASc student and allowing me to become involved in the CIRFE group. His mentorship, support, and understanding made my time within this research group memorable. The insight he provided throughout my degree will not be forgotten. It has been my honor to be a member of CIRFE and his student.

I would also like to thank Dr. Paul Laforge for introducing me to the field of RF engineering. I would like to provide a special thank you to Johnny for training me on the cryogenic probe station. A special thank you to Navjot and Tejinder for being fantastic teammates whenever we had to test devices. A thank you to Edward for being my closest and most supportive friend in the CIRFE group.

To my colleagues and friends within the CIRFE group, thank you as well. The things you've all taught me and the memories we've shared here will not be forgotten.

I would like to thank my family. Also, I'd like to thank the friends I've made in Waterloo; thank you Aidan, Andrew, Daniel, Matt, Jonah, and Jordan, I couldn't have asked for better friends to do my master's alongside with.

Thank you to Kate for identifying 1355 revisions to this thesis. Finally, I would like to thank my closest friends back in Regina. You guys have been with me since day one.

## Dedication

To Archie, Ena, and Una. You three are the future. This one is for you.

# Table of Contents

# List of Figures

# List of Tables

# Chapter 1

# Introduction

## 1.1 Motivation

The microwave filters of today are required to follow stringent constraints that require limiting physical size while also minimizing the loss of energy. Multi-band substrate integrated waveguide (SIW) filters can be used to greatly reduce the size of filters while maintaining an acceptable quality factor. Planar technology that uses multiple layers can also be used to reduce the overall size of a filter design.

Several transmission technologies are available for filter design, such as microstrip, dielectric resonators, waveguides, and even superconductors. While dielectric resonators and

waveguides provide excellent Q-factors, the size of these filters limits their applications. Microstrip technology is relatively smaller in size, but the loss in energy for filters at higher frequencies is too great. Superconductors provide minimal loss in energy with minimal size, but are limited to low-temperature applications. SIWs provide an acceptable compromise in terms of energy loss and size reduction, as shown in Figure 1.1. An SIW is created by taking microstrip planar technology and drilling vias in to mimic the appearance of a waveguide.

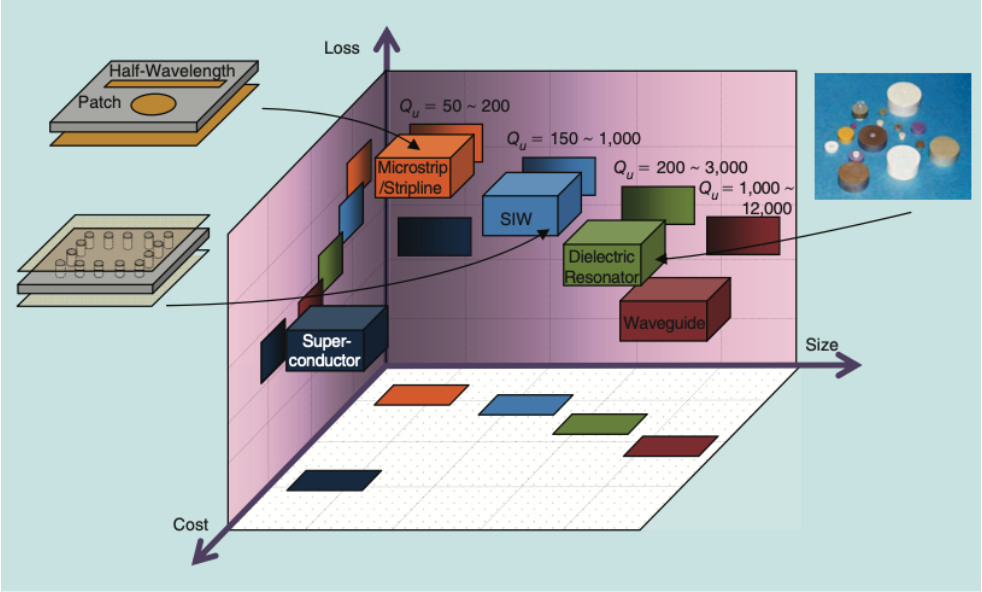


Figure 1.1: The loss of energy, resonator size, and cost of resonators in different transmission technologies. [1]

For systems that support several frequency bands, multi-band filters are an excellent option

to help reduce the overall size. A single filter can be used in place of multiple filters. The use of multi-band filters in diplexers can reduce system size, because, as is demonstrated in Figure 1.2, the communication architecture requires only a single low noise amplifier (LNA) and power amplifier (PA) on the receiving and transmitting branches, respectively.

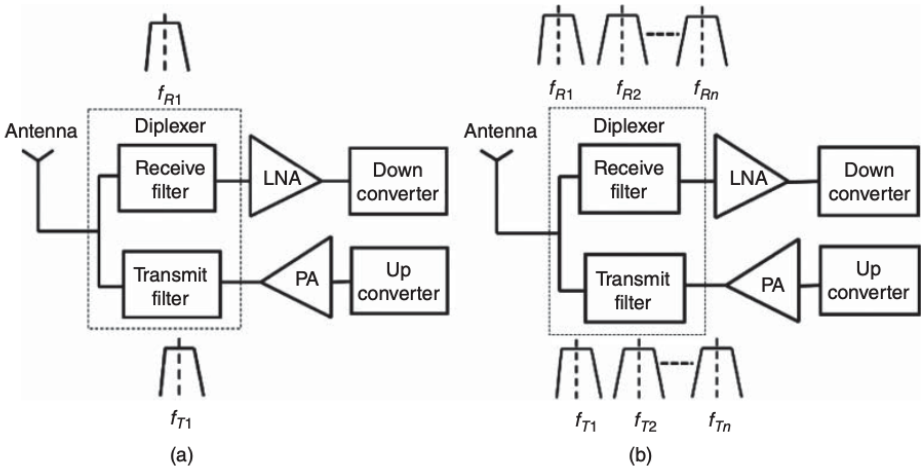


Figure 1.2: The use of (a) single-band filters and (b) dual-band filters in diplexers within a communication system. [2]

Further size reduction can be realized with the use of multi-layer planar technologies, such as printed circuit boards (PCB). These technologies allow for the design and fabrication of SIW and lumped element filters that use multiple dielectric and conducting layers. For lumped element filters, vertically integrated interdigital capacitors and stacked spiral inductors can be used to drastically reduce the size of the filter. Multi-layer SIW filters can be realized by vertically stacking filters connected in parallel, thereby reducing

the overall footprint. MIT Lincoln Labs (MIT-LL) process [3, 4] allows for the realization of superconducting lumped element filters with 4-layer and 8-layer technology using niobium-based fabrication processes. The combination of multi-layer technology and superconducting circuitry provides incredible filter performance with minimal size, even at very low frequencies.

## 1.2 Objective

The primary focus of this thesis is to investigate the characteristics, performance, and design methods for SIW filters while also realizing dual-band filters using SIW technology and exploring further miniaturization techniques using superconducting multi-layer technologies to develope low frequency, highly miniaturized filters.

Several design considerations must be addressed when dealing with SIW filters, one of which is the transition technology required. The choice in transition technology will determine the input/output impedance match. If the input match is poor, then much of the input power to the filter will be reflected. The type of transition also impacts the achievable bandwidth of the match. The frequency range of the match becomes increasingly important when designing multi-band SIW filters. Another important consideration to be made is the via pitch and via diameter. The choice of the via pitch/diameter depends on the frequency of

operation and can be used to optimize the filter performance.

The cost of implementing large-sized circuits using the MIT-LL fabrication process is quite high, therefore, the minimization of the submitted circuits essential. With low frequency lumped element circuitry, the sizes of structures can be large. As a result, to allow for these designs to be realized, several minimization strategies must be considered.

## 1.3 Outline of Thesis

Following the introduction of this thesis, a summary of SIW technology and its design considerations is presented, with summaries of dual-band filters and lumped element filters at cryogenic temperatures being highlighted in Chapter 2. Chapter 3 presents the design methods and measurements for the single and dual-band SIW filters along with the designs of the transitions. Chapter 4 highlights the design and miniaturization of lumped-element superconducting filters followed by the design of a superconducting slotline resonator filter. The conclusion is given in Chapter 5.

# Chapter 2

# Literature Survey

## 2.1 SIW Technology

### 2.1.1 Introduction

In planar technology, SIWs are created by placing equidistantly spaced vias throughout the substrate, as shown in Figure 2.1. The placement of these via arrays allows for easy and cost-effective integration of rectangular waveguide circuitry into planar circuits such as PCB.

The concept of an SIW was introduced in [6]. Since then, SIWs have been used in a multitude of RF devices such as filters [7–9], directional couplers [10, 11], and antennas

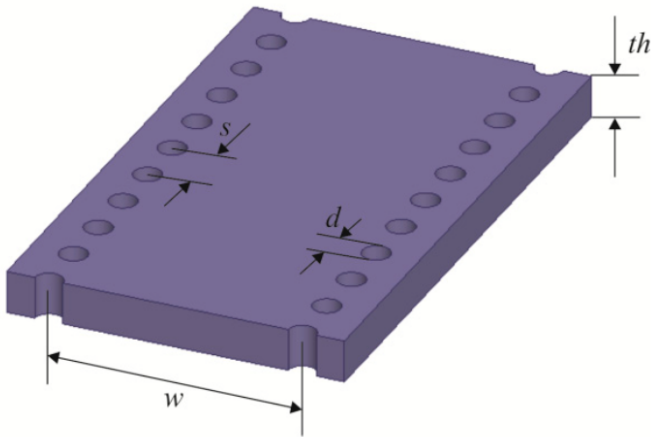


Figure 2.1: A diagram of an SIW. [5]

[12, 13]. For an SIW, the choice of the transition technology is important. The transition must successfully couple the two transmission mediums properly to ensure that the minimal amount of energy is reflected in the frequency band of interest. Alternatively, the two mediums must have matched impedances over a range of frequencies.

The diameter of the vias and the pitch between two sequential vias are extremely important design dimensions to consider. The operating frequency of the SIW will determine the absolute values of these variables, however, they are required to follow a set of design rules outlined in [1]:

1. $p > d$

2. $\frac{p}{\lambda_c} < 0.25$

3. $p \leq 2d$

4. $\frac{p}{\lambda_c} > 0.05$

Here, $p$ is the pitch between two vias, $d$ is the diameter of the vias, and $\lambda_c$ is the guided wavelength. The first condition states that the pitch between two sequential vias must be larger than the diameter of the vias. This ensures that the circuit can be physically realized. The second guideline ensures that there is no bandgap present within the bandwidth of $TE_{10}$ mode. To ensure that there are negligible leakage losses, the third rule is enforced. Finally, the number of cylinders per wavelength should not exceed 20. This rule is nonessential, however, it does ensure that the mechanical rigidity is not affected [1]. The regions of interest for the SIW such that the rules 1-3 are adhered to can be seen in Figure 2.2.

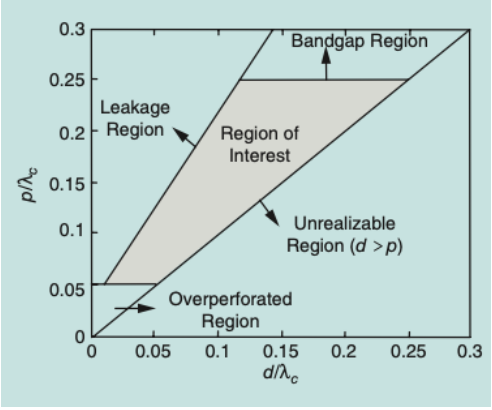


Figure 2.2: The region of interest for SIW design. [1]

### 2.1.2 Equivalent Width of SIWs

The concept of the SIWs equivalent width was introduced in [14]. Here, the SIW is shown to have the same guided wave characteristics as a conventional waveguide, and this relationship can be expressed as the equation shown below:

$$W_{SIW} = W_{waveguide} + \frac{d^2}{0.95 * p} \tag{2.1}$$

Where $W_{SIW}$ is the width of the SIW from post-to-post, $W_{waveguide}$ is the width of the corresponding waveguide, $d$ is the via diameter, and $p$ is the pitch between two adjacent vias. These findings imply that it is possible to convert any waveguide into an SIW and vice-versa by applying equation 2.1. Since this discovery, many other models for relating the width of an waveguide to the width of a SIW have been developed.

Equation 2.1 can be modified to obtain the empirical equation 2.2 [15]. The addition of an extra term $\frac{d}{W_{waveguide}}$ accounts for an error that presents itself as $d$ increases.

$$W_{SIW} = W_{waveguide} + 1.08 * \frac{d^2}{p} - 0.1\frac{d^2}{W_{waveguide}} \tag{2.2}$$

This is accurate provided that $\frac{p}{d}$ is less than three and $\frac{d}{W_{waveguide}}$ is less than 0.2. The ratio of the pitch and diameter is further restricted to match rule 3 mentioned in section 2.1.1

($\frac{p}{d} < 2$) to reduce the leakage losses. If the rules are adhered to in both equation 2.1 and 2.2, the width of the SIW will range from $W_{waveguide}$ to approximately $W_{waveguide} + d$.

A formula for normalizing the width of an equivalent waveguide is introduced in [16]. This formula provides a relative error below 1% and is shown below:

$$b = x_1 + \frac{x_2}{\frac{p}{d} + \frac{x_1 + x_2 - x_3}{x_3 - x_1}} \tag{2.3}$$

where

$$x_1 = 1.0198 + \frac{0.3465}{\frac{W_{SIW}}{p} - 1.0684} \tag{2.4}$$

$$x_2 = -0.1183 - \frac{1.2729}{\frac{W_{SIW}}{p} - 1.201} \tag{2.5}$$

$$x_1 = 1.0082 - \frac{0.9163}{\frac{W_{SIW}}{p} + 0.2152} \tag{2.6}$$

and

$$W_{waveguide} = W_{SIW} * b \tag{2.7}$$

This is more complex than equations 2.1 and 2.2 and is ideal when converting from SIW to waveguide. If converting the opposite way, it is beneficial to use a mathematical solver.

The fourth equation determined is a closed-form expression to estimate the cutoff frequency for the dominant mode under the condition that the SIW is exhibiting low leakage [17].

Equation 2.8 maintains higher accuracy for a larger range of structural parameters than equations 2.1 and 2.2. Similarly for equations 2.3 - 2.7, equation 2.8 is ideal for converting SIW to waveguide.

$$W_{waveguide} = \frac{W_{SIW}}{\sqrt{1 + (\frac{2*W_{siw}-d}{p}) * (\frac{d}{W_{SIW}-d})^2 - \frac{4*W_{SIW}}{5*p} * (\frac{d^2}{W_{SIW}-d})^3}} \tag{2.8}$$

Another formula is presented can be seen in equation 2.9 [18]; which is again required to adhere to $p < 2d$. When the radius of the vias is less than one-fourth of the pitch, $W_{waveguide}$ is larger than $W_{SIW}$.

$$W_{SIW} = \frac{2 * W_{waveguide}}{\pi}(\text{cot}^{-1}(\frac{\pi * p}{4 * W_{waveguide}} * \ln \frac{2 * p}{4 * \frac{d}{2}})) \tag{2.9}$$

In [19], a formula is developed with the goal of eliminating any iterative processes required when determining $W_{SIW}$. With the exception of equations (2.1), (2.2), and (2.9), the SIW width is buried within. This paper also analyzes and compared each of the formulas above with equation (2.10). The results of these analyses show that all equations presented, except for (2.9), provide acceptable results with equation 2.10 being the most balanced in terms of complexity and accuracy.

$$W_{SIW} = W_{waveguide} + p * (0.766 * e^{0.4482*\frac{d}{p}} - 1.176 * e^{-1.214*\frac{d}{p}}) \tag{2.10}$$

### 2.1.3 SIW Transition Technologies

The type of transition used will depend on the transmission medium of the incoming signal. This section will elaborate on the most common transitions, which include microstrip-to-SIW, grounded coplanar waveguide (GCPW)-to-SIW, and waveguide-to-SIW. The results will then be compared, and one transition will be applied to the design of the quasi-elliptic filter.

Microstrip transitions are the most common type of transition seen for devices designed on SIW. There are two primary methods of microstrip-to-SIW transitions: tapered microstrip and slot coupled. These methods allow for full bandwidth matching at higher frequencies. Methods such as defective ground structure (DGS) and via coupled transitions exist, however, they are used for SIWs with multiple layers and they do not have the ability to achieve a match as wideband as the tapered and slot transitions.

The microstrip taper is the most common microstrip-to-SIW transition [20–22]. Here, a tapered transmission line is inserted between the input microstrip line and SIW to match the impedances of the two. If the microstrip line has a larger impedance than the SIW interface, the taper size will increase from the former to the latter and vice versa. The tapered line is only used to match the impedance, therefore, if a filter is being designed, irises will be required for the input/output coupling to be realized. Tapered transitions

are the simplest to design, however, they can add significant size to the circuit, especially at lower frequencies. The addition of vias to the transition can improve matching and add several degrees of freedom to the design as well [22]. Figure 2.3 shows the topology of a tapered transition with and without the additional vias.

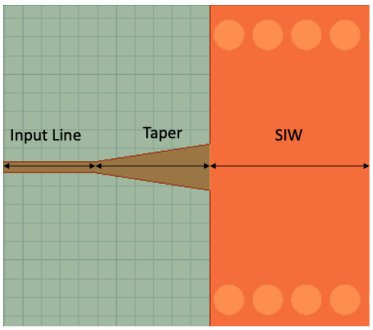


Figure 2.3: A diagram of a tapered transition from microstrip to SIW

Slot coupled transitions are very popular options for transition technology because they also act as input/output coupling [1, 7, 23]. This transition is realized by etching the top conductor of the SIW such that a slot (typically 'L' shaped) is made. Figure 2.4 shows the topology of a slot coupled transition.

The GCPW transitions are another popular method used to match SIWs to an input line on planar technology [24, 25]. This type of transition presents similar benefits as the microstrip transitions such that it can be used for wideband matching with the design complexity being similar. One benefit of the GCPW over microstrip is that the main line width is flexible. Figure 2.5 shows an example of a GCPW transition to SIW.

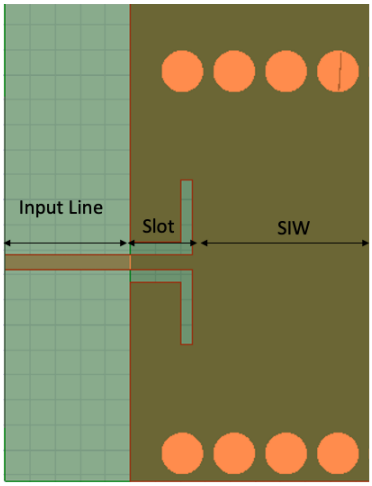


Figure 2.4: A diagram of a slot coupled transition from microstrip to SIW

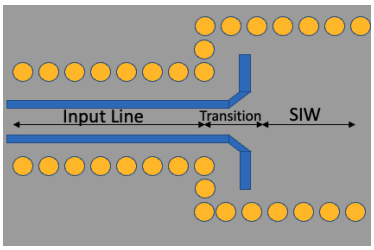


Figure 2.5: A diagram of a transition from CPW to SIW. Modified from [24]

waveguides can also be used to transition to SIW [26, 27], however, they are quite narrowband at higher frequencies compared to microstrip and GCPW transitions and they are much bulkier. One benefit is that they have more degrees of freedom in the design in the form of slot and waveguide position, width, and length. waveguide-to-SIW transitions come in two configurations: in-line and right-angle. The right-angle configuration can be seen in Figure 2.6.

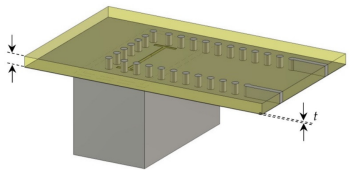

Figure 2.6: A diagram of a transition from waveguide to SIW. [27]

### 2.1.4 SIW Filters

An example of a 10GHz 4-pole linear phase SIW filter fabricated on PCB can be seen in [7]. The filter performance shows a measured return loss better than 14 dB and an insertion loss of 2.9 dB. The size of this filter is 27.43mm by 26.5mm. Figure 2.7 (a) and (b) show the fabricated filter along with the measured and simulated results. From the design, it can be seen that the use of a folded topology is to allow for inductive cross-coupling between the first and fourth resonators. An equivalent lumped element filter at this frequency would provide a larger insertion loss while an waveguide would be larger in size.

Another example is the design of an SIW filter in a box configuration operating at a center frequency of 5.25 GHz [28]. Here, a 4-pole Chebyshev filter is designed with the upper stopband being improved by the use of two transmission zeros, one realized with inductive coupling via irises and the other realized using dispersive coupling in the form of a shorted stub. The insertion loss is 2.4 dB while the measured return loss is given as 15.9 dB. The results and fabricated filter can be seen in Figure 2.8 (a) and (b) respectively. The size of

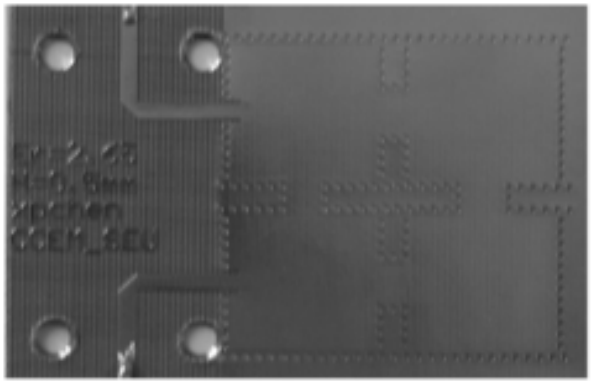

(a)

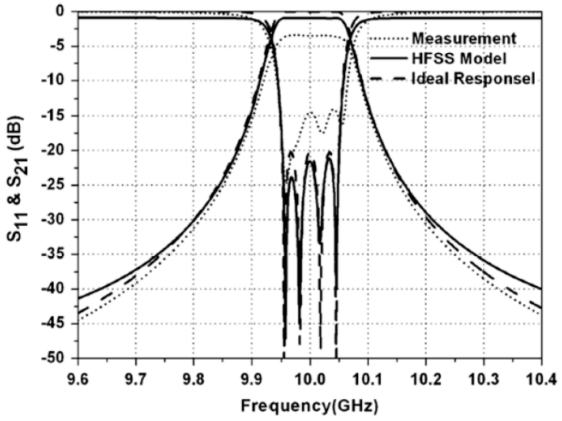


(b)

Figure 2.7: The (a) fabricated 4-pole linear phase SIW filter with the (b) ideal, EM simulation, and measured response. [7]

this filter is 62.36mm by 43.78mm.

In another work, an ultra-wideband SIW filter operating at center frequency of approximately 7.25GHz was designed with the use of a zig-zag topology [29]. The use of the zig-zag

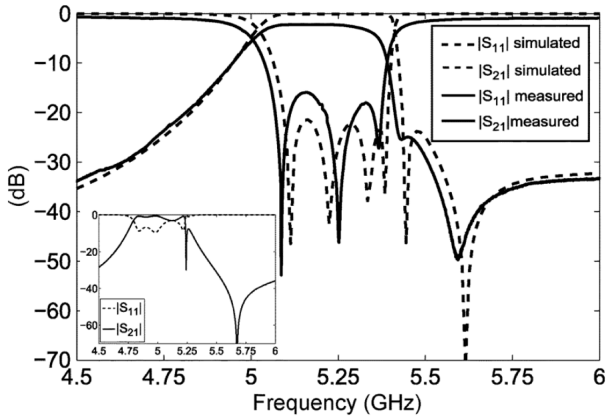


(a)

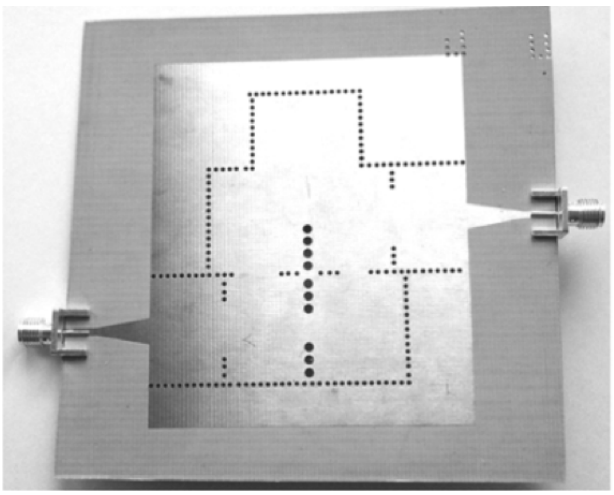

(b)

Figure 2.8: (a) The simulated and measured results of the SIW filter and (b) the corresponding fabricated design. [28]

topology allows for easy integration of cross-couplings in non-adjacent cavities and ensures the control of transmission zeros. The fabricated filter that uses the flexible cross-coupling

can be seen in Figure 2.9 (a) while the measured and simulated results of the designed filters are seen in Figure 2.9 (b).

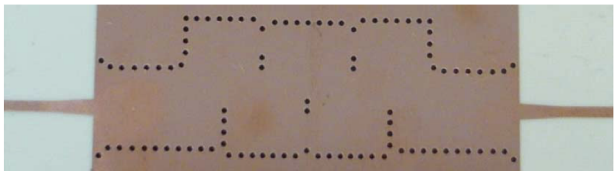

(a)

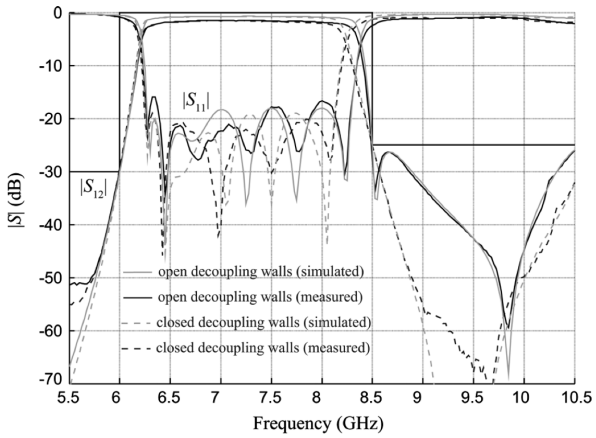


(b)

Figure 2.9: (a) The fabricated SIW zig-zag filter with flexible cross-couplings and (b) the simulated and measured results of the designed filters. [29]

As shown in the figures, the fabricated filter with flexible cross-couplings has a return loss lower than 17 dB, an insertion loss of 1.18 dB, and a bandwidth of 28%. The resonators used in the design have a Q-factor of 220 at 7.5GHz.

Each of the filters mentioned was fabricated on PCB technology and uses SIW in the design.

Also, they highlight the flexibility of SIWs and the wide range of topologies available for this technology.

## 2.2 Multi-Band Filters

Multi-band filters are used widely in communication systems with the goal of serving multiple frequency bands while reducing the footprint, cost, and complexity of the network. The first multi-band circuit was presented in [30] for dual-mode portable phones. Since then, the interest in multi-band filters has expanded. Currently, triple and even quad-band filters are being designed, and multi-band filters are being realized using different transmission architectures [31–34].

There are four methods that can be used to realize multi-band filters. The first method involves inserting in-band transmission zeros into a wideband filter. Secondly, resonators with multiple modes can be used to realize multi-band filters if each mode corresponds to a different passband. The third method uses multiple filters, which are connected in parallel. Finally, using a wideband filter with a multi-notch reject filter cascaded can result in a multi-band filter response.

An example of the first method and second method can be seen in [35]. Here, a circular waveguide dual-band filter using a canonical structure is designed. The wideband filter is

set to have six poles, but using effective cross-coupling, a transmission zero can be placed in-band in order to split the wideband filter into two 3-pole bands. Not only that, but the use of dual-mode resonators allows for further miniaturization of the filter. Figure 2.10 (a) shows the signal flow of the filter while (b) shows the physical drawing. Figure 2.11 highlights the measured and simulated results.

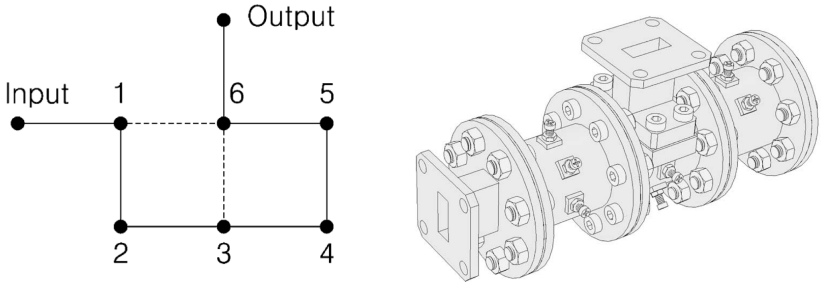


(a) (b)

Figure 2.10: (a) The signal flow of the canonical dual-band filter and (b) the physical drawing. [35]

An example of the third method is used in [36] to design a 2-port triplexer. This triplexer uses a manifold-coupler to switch between passbands. The passbands are determined by three parallel 8-pole filters designed using high temperature superconducting (HTS) microstrip technology. The resonators are realized using double spiral inductors and interdigital capacitors [37]. Figure 2.12a shows the insertion loss simulation and measured results, Figure 2.12b shows the return loss, and (c) shows the layout.

The return loss of each band is greater than approximately 13 dB. The low insertion

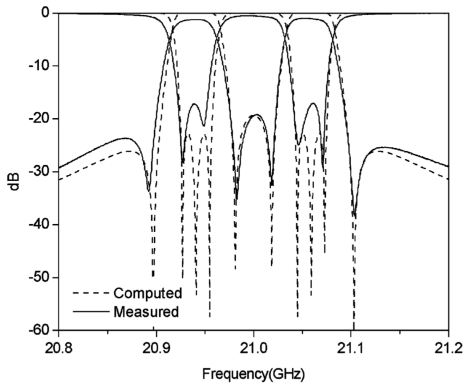


Figure 2.11: The simulated and measured results of the circular waveguide dual-band canonical filter. [35]

loss exhibited in this design is due to the superconducting and wideband nature of the circuit. As shown in Figure 1.1, superconducting filters provide the best miniaturization while keeping losses low. Unfortunately, this technology is expensive to fabricate.

Another HTS filter is designed in [38] using the fourth method. Here, a triple-band filter is realized by cascading a dual-notch filter with a wideband filter. The band-reject filter is realized by resonators spaced in such a way that the cross-coupling was minimal. The bandpass filter is realized using folded stubs. Figure 2.13a shows the layout of the filter while b shows the results of the insertion loss. Similarly to the filter in Figure 2.12, the insertion loss is quite low due to the nature of superconductors and the wideband nature of this filter. It is also noted that this filter is 42.7mm by 42.7mm.

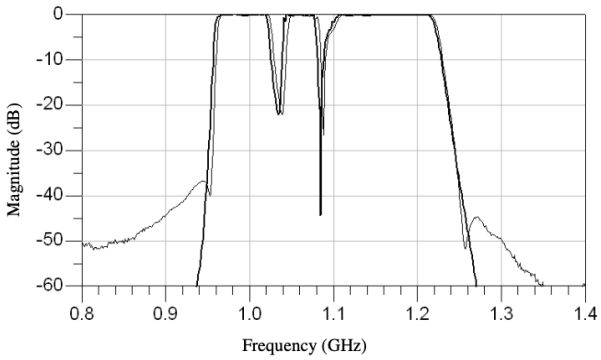


(a)

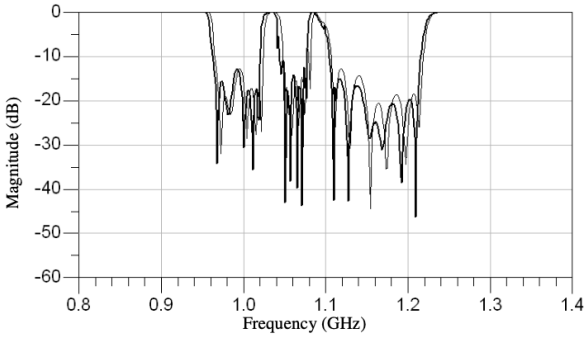


(b)

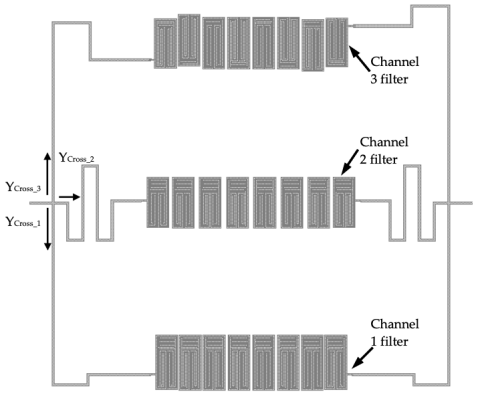


(c)

Figure 2.12: (a) The measured and simulated insertion loss, (b) the return loss, and (c) the layout of the triplexer. [36]

## 2.3 Superconductivity

Superconducting circuits have been a research interest for some time now. These circuits allow for the design of miniaturized high-Q devices due to the low resistance properties it

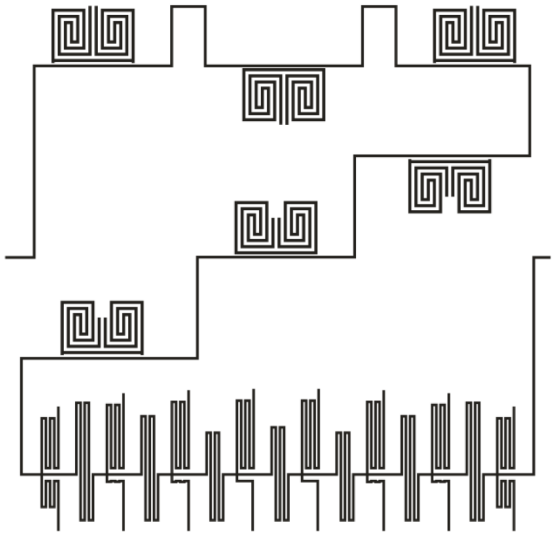

(a)

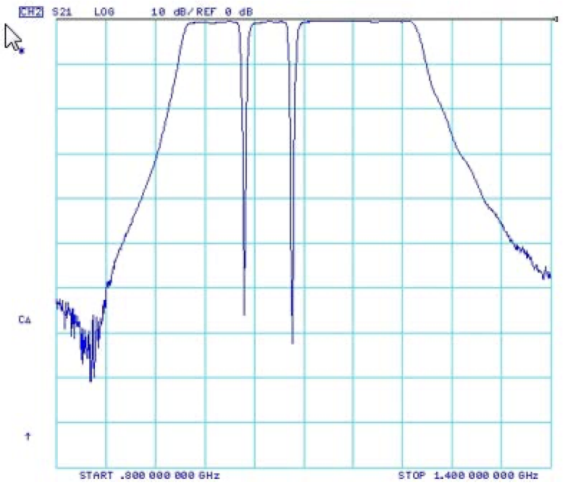


(b)

Figure 2.13: (a) The layout of the triple-band filter and (b) the insertion loss. [38]

provides.

The low resistance properties of superconducting circuits are due to the presence of electron pairs, also known as Cooper pairs. Cooper pairs do not experience resistive losses when travelling through conducting material. Normal electrons still travel through the conducting material alongside Cooper pairs. The temperature determines the ratio of normal electrons ($n_n$) and Cooper pairs ($n_s$). Once the critical temperature ($T_c$) is surpassed, the Cooper pairs will no longer be present. At temperatures below $T_c$ the number of Cooper pairs increases. Equation 2.11 and 2.12 provide a method for the calculation of the number of Cooper pairs and the number of electrons present in a superconductor.

$$n_s = n_o(1 - t^4) \tag{2.11}$$

$$n_n = n_o t^4 \tag{2.12}$$

The number of carriers is given as $n_o$ and $t = \frac{T}{T_c}$. $T$ is the actual temperature and $T_c$ is the critical temperature, as denoted above.

The equivalent circuit model for a superconductor can be seen in Figure 2.14 with equation 2.13 for the current density ($J$).

$$J = J_s + J_n \tag{2.13}$$

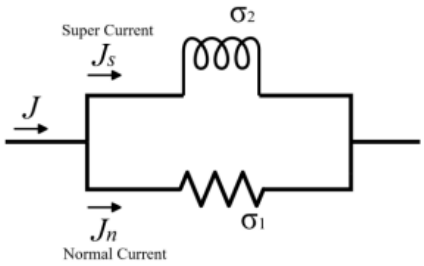


Figure 2.14: The equivalent circuit model for a superconductor. [39]

The current density $J$, is a summation of the super current ($J_s$) density and the normal current ($J_n$) density. It can also be expressed in terms of the complex conductivity shown in equation 2.15.

$$J = (\sigma_1 + j\sigma_2)E \tag{2.14}$$

When operating at DC, the inductor in Figure 2.14 becomes a short circuit with all current flowing through, meaning that the circuit is lossless. As the frequency increases, so does the reactance of the structure, causing larger losses at higher frequencies. The impedance of the superconductor is expressed in equation 2.16.

$$Z_s = \lambda_D \omega \mu (\frac{\omega \mu \sigma_1 \lambda_D^2}{2} + j) \tag{2.15}$$

Here, $\lambda_D$ is the penetration depth and can be expressed as:

$$\lambda_D = \frac{1}{\sqrt{\omega\mu\sigma_2}} \tag{2.16}$$

Given this relationship, it can be seen that superconductors have a significantly smaller skin depth when compared to their standard conducting counterparts. The surface resistance (real component of $Z_s$) of a superconductor appears to increase proportionally to the square of the frequency while the surface resistance of a normal conductor will increase with the square root of the frequency (equation 2.17). Here $\sigma_n$ is the conductivity of the normal conductor.

$$R_s = \sqrt{\frac{\omega\mu}{2\sigma_n}} \tag{2.17}$$

Referring back to equation 2.15 and Figure 2.14, it can be seen that the value of the inductor can be determined in equation 2.18. This is known as the kinetic inductance of the superconducting material.

$$L_s = \mu\lambda_D \tag{2.18}$$

Figure 2.15 shows the variations of the surface resistance of two superconducting materials and one ordinary conductor as frequency increases. Due to the squared relation of $R_s$ and frequency in superconductors, the surface resistance of the superconductors $Nb$ and

$YCBO$ increase at a much higher rate than the ordinary conductor copper ($Cu$). Eventually, at some frequency the losses in the superconductors will surpass those in the normal conductors.

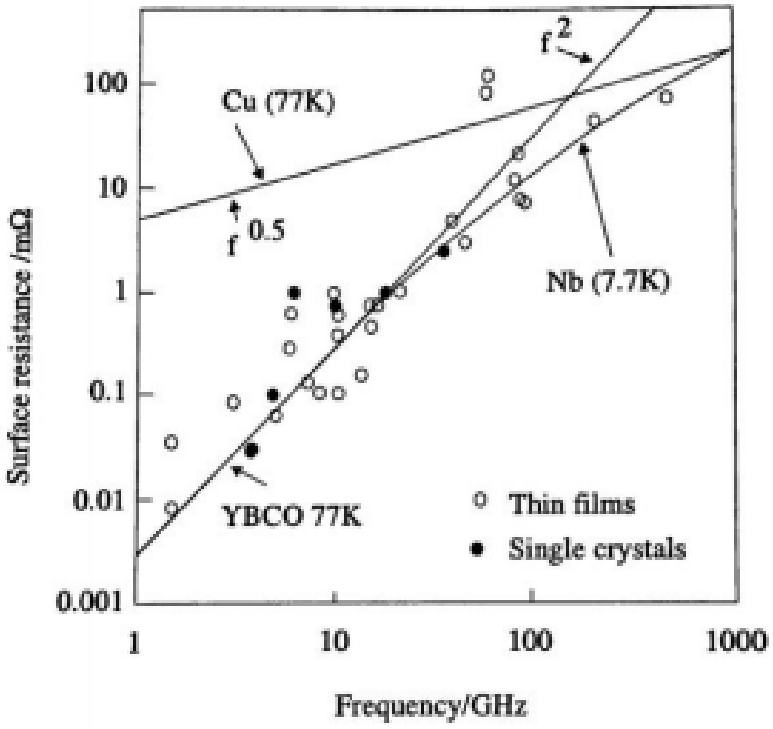


Figure 2.15: The surface resistance of superconductors (Nb and YCBO) and normal conductors (Cu) versus frequency. [39]

## 2.4 Superconducting Filters

Multilayer superconducting circuits using niobium metal layers can be realized using the MIT-LL [4] Nb process. With access to multiple layers, a designer can further reduce the footprint of their circuit. One method of doing this is through the use of vertically integrated interdigital capacitors and stacked spiral inductors. Other miniaturization methods explained in [40] include the use of substrates with high dielectric constants, coiling/meandering transmission lines, implementing internal inductance, and using slow wave transmission lines.

While superconducting filters provide designs with extremely low losses, the use of a cryogenic probe station to test these devices is required. Such a station requires cooling down to at least 4K for low-temperature superconductors and 77K for high-temperature superconductors. Unfortunately, due to these constraints, the applications of superconducting filters are very limited.

The use of MIT-LL's 8-layer Nb process to design a low-temperature superconducting filter can be seen in [41]. Here, an ultra wideband (UWB) superconducting filter is designed using CPW resonators. Even though there was only one layer that contained signal lines, the availability of the extra layers allowed for flexibility in the design of the crossovers.

These crossovers can be placed on any layer other than the signal layer to introduce stronger

or weaker parasitic capacitances. When placed on layers immediately above the signal line layer, the parasitic capacitances are at their strongest. As a result, a downward frequency shift can be observed, resulting in a size reduction of 57% for the filter. Figure 2.16a shows the layout of the superconducting filter while Figure 2.16b shows the measured and simulated results.

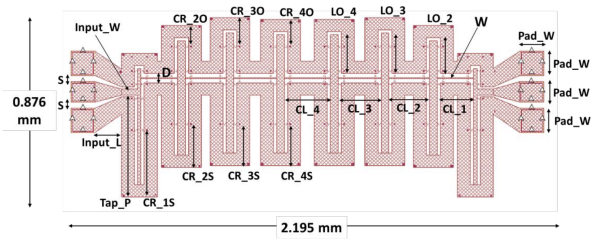


(a)

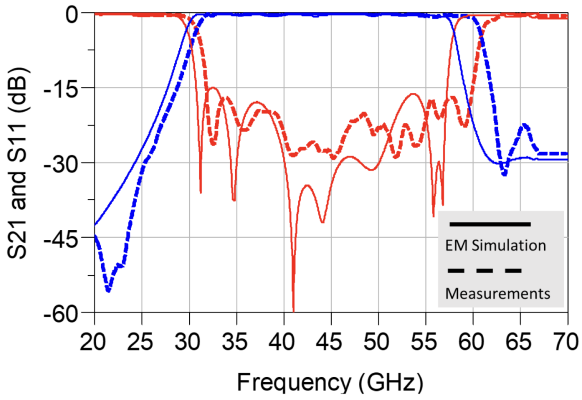


(b)

Figure 2.16: (a) The layout of the UWB filter and (b) the simulated and measured results. [41]

There are many papers on the design of high-temperature superconductors, however, the

designs primarily use distributed components since they are restricted to only a single layer. One example is given in [42], where a 610MHz filter was designed with a bandwidth of less than 1%. Here, the use of dual-spiral inductors and interdigital capacitors allows for the easy realization of resonators. The final filter layout can be seen in Figure 2.17 with the results in Figure 2.18.

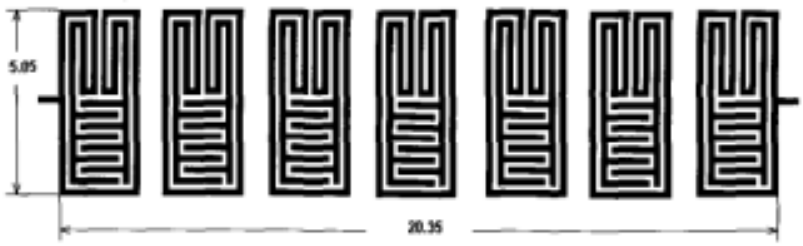


Figure 2.17: The layout of the microstrip resonator high-temperature superconducting filter. [42]

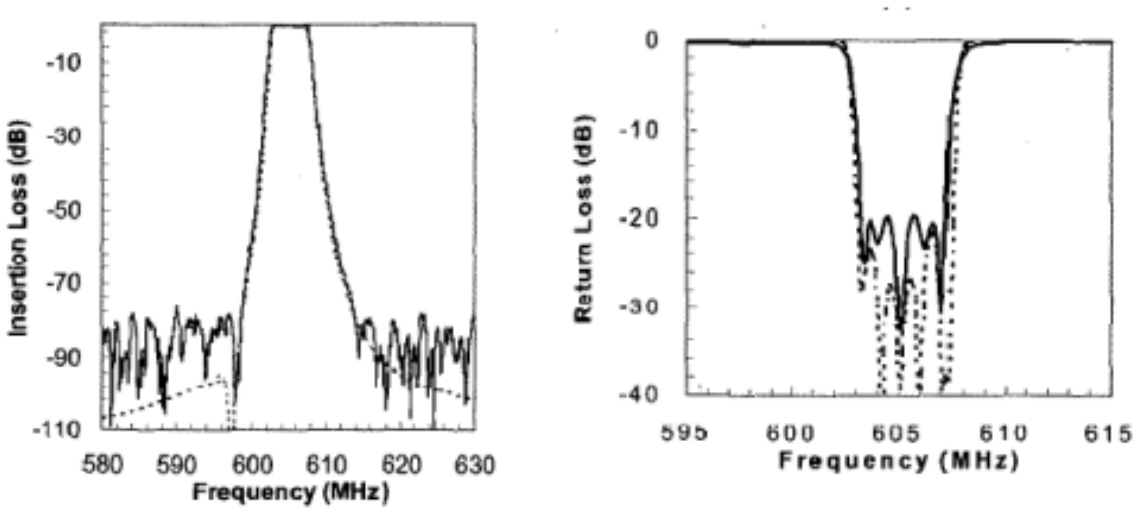


Figure 2.18: The results of the microstrip resonator high-temperature superconducting filter. [42]

# Chapter 3

# Substrate Integrated Waveguide (SIW) Filter Design

The core parameters of the SIW must be established prior to beginning the design of the filter itself. Attention must be paid to the chosen parameters such that the four design rules ($p > d$, $\frac{p}{\lambda_c} < 0.25$, $p \leq 2d$, $\frac{p}{\lambda_c} > 0.05$) are followed and the circuit is within the fabrication capabilities available at the time. Fabrication tolerances must be taken into consideration as well when the frequency of interest is increased. As the SIW circuits become smaller, the effect of absolute tolerances creates larger errors between fabrication and design.

For SIW filters, the incoming signal is likely being transmitted via a different technology

(microstrip, stripline), therefore, it is important that the impedances of the two interfacing mediums are matched. There are two techniques used to accomplish this. First, the thickness of the SIW board can be adjusted. Unfortunately, the application of this option is limited due to there being set board thicknesses, so obtaining an exact match with this method alone is difficult. The next technique is to add a transition between the two mediums. Such a transition will act as an impedance transformer.

This chapter investigates the design and fabrication of a 4 GHz 4-pole quasi-elliptic SIW filter with a bandwidth of 4.2% and a dual-band SIW filter. As part of this process, the decisions for via diameter and pitch are explored and the equations for the SIW equivalent widths are analyzed. One is then chosen and applied to the design. The SIW transition is then designed. Afterward, the filter is realized using Agilent ADS [43] and HFSS [44] as circuit and EM simulators, respectively. Three different methods of designing the sequential paths are explored; the first is a method that uses only the K-impedance inverter, the second method makes use of the coupling matrix and eigenmode analysis, and the third is a hybrid method that uses both the K-impedance inverter and eigenmode analysis. These three methods are compared. The cross-coupling is determined through eigenmode analysis and then combined with the initial model of the filter. The final simulated results and measurements will be presented as well. It is important to note that the simulations presented are for the second round of designs, in which the filters are designed with a

dielectric constant of 3.55 in mind, but the measured results are from a fabricated filter that was designed with a dielectric constant of 3.38. The corresponding simulations for the measured filter will be shown in the measurements section. The reasoning for this variability is that the material chosen was marketed with a dielectric constant of 3.38, but it is advised to design at 3.55. This detail was not noticed until after the fabrication of the filters.

## 3.1 Via Diameter and Pitch

When designing SIWs, it is important to properly select the diameter and pitch of the vias. Generally, if rules 1 to 4 from Section 2.1 are followed, the dimensions will be sufficient. However, to determine the absolute values of the pitch and the diameter, the frequency must be taken into account. From the filters shown in [7, 28, 29, 45], it can be seen that the diameter of the vias will vary depending on the given frequency, and as a result, so will the pitch. When analyzing transition technology, [22] considers SIWs in every band from the X-band to the E-band. An interesting observation in their work is that, when moving downwards through bands, both the pitch and diameter increase by factors of approximately 1.5 per band. This is in attempt to maintain $0.6 < \frac{d}{p} < 0.8$ and ensure that there are at least ten vias per guided wavelength.

Using this concept, we can determine what the appropriate via dimensions will be for the C, S, and L bands. Table 3.1 shows the diameters and pitches for these bands, along with those in the upper bands shown in [22]. Here, both the pitch and diameters were multiplied by 1.5 for every lower band. This maintains a $\frac{d}{p}$ of 0.65. These provide a range of appropriate initial values based on the center frequency.

Table 3.1: The via pitch and diameter for various frequency bands [22]

| | L-Band | S-Band | C-Band | X-Band | Ku-Band | K-Band | Ka-Band | U-Band | E-Band |
|---|---|---|---|---|---|---|---|---|---|
| Band (GHz) | 1-2 | 2-4 | 4-8 | 8-12 | 12-18 | 18-26.5 | 26.5-40 | 40-60 | 60-90 |
| p (mm) | 7.43 | 4.95 | 3.3 | 2.2 | 1.5 | 1 | 0.7 | 0.45 | 0.3 |
| d (mm) | 4.826 | 3.218 | 2.145 | 1.43 | 0.975 | 0.65 | 0.455 | 0.2925 | 0.195 |

## 3.2 Equivalent Width of SIWs

When designing waveguide filters, the choice in waveguide width is important. The width must be chosen such that the cutoff frequency is sufficiently below the desired operating frequency; this can be determined by equation 3.1.

$$W_{waveguide} = \frac{c}{2 * f_c * \sqrt{\epsilon_r}} \tag{3.1}$$

The choice in which equation to use comes down to one factor: the value of $\frac{d}{p}$. Figure 3.1 shows the values of the equivalent widths for various $\frac{d}{p}$ using the equations presented in 2.1.2, and demonstrates that there is a range of $\frac{d}{p}$ where the choice of equation does not matter, excluding equation 2.9. As $\frac{d}{p}$ approaches 0.8, the equations converge on similar values. While the ratio becomes lower than 0.8 or approaches 1, the values diverge, which will result in a difference in transmission performance. For simplicity of design, knowing that the range of $\frac{d}{p}$ should remain between 0.6 and 0.8, d and p should be chosen such that the ratio is in the higher end of the range. Figure 3.2 shows the simulation results for the different $\frac{d}{p}$. Figure 3.2d shows the HFSS model used for the simulations. Here, a waveguide-to-SIW transition is used. This transition will act as a simple transmission line if the SIW width is equivalent to the waveguide width. If it is not, reflections will be present in the discontinuity between the waveguide and SIW.

## 3.3 Quasi-Elliptic SIW Filter Design

### 3.3.1 SIW and Transition Design

As highlighted in Sections 3.1 and 3.2, the SIW pitch and via dimensions along with the transition must be designed prior to the design of the filter. Given the information in Table

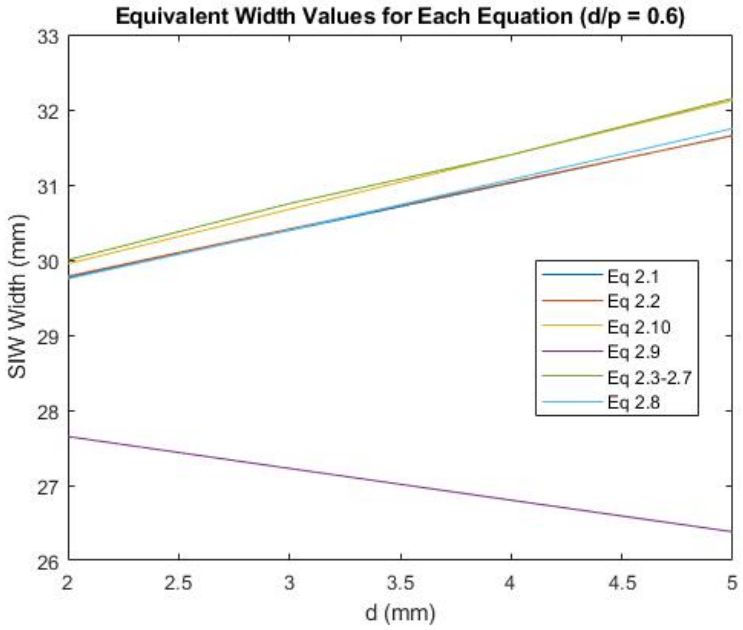
Equivalent Width Values for Each Equation (d/p = 0.6)
SIW Width (mm)
d (mm)
Eq 2.1
Eq 2.2
Eq 2.10
Eq 2.9
Eq 2.3-2.7
Eq 2.8

(a)

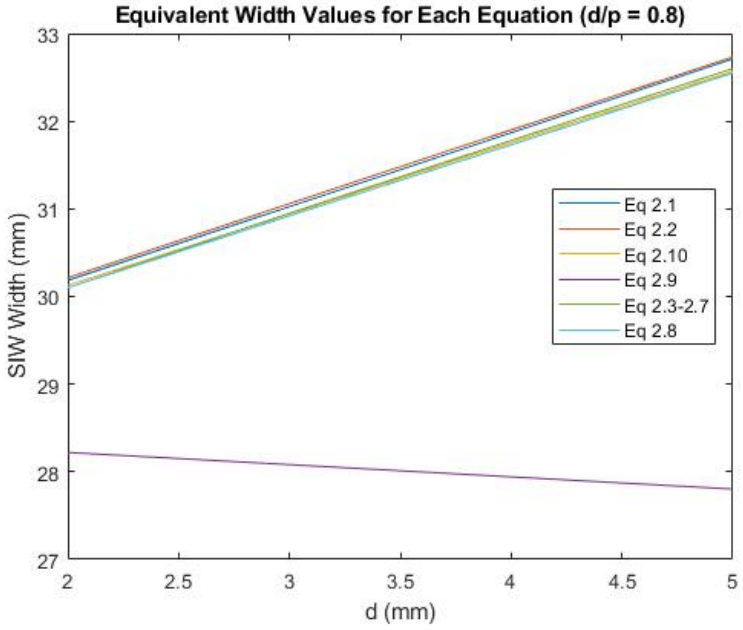
Equivalent Width Values for Each Equation (d/p = 0.8)
SIW Width (mm)
d (mm)
Eq 2.1
Eq 2.2
Eq 2.10
Eq 2.9
Eq 2.3-2.7
Eq 2.8

(b)

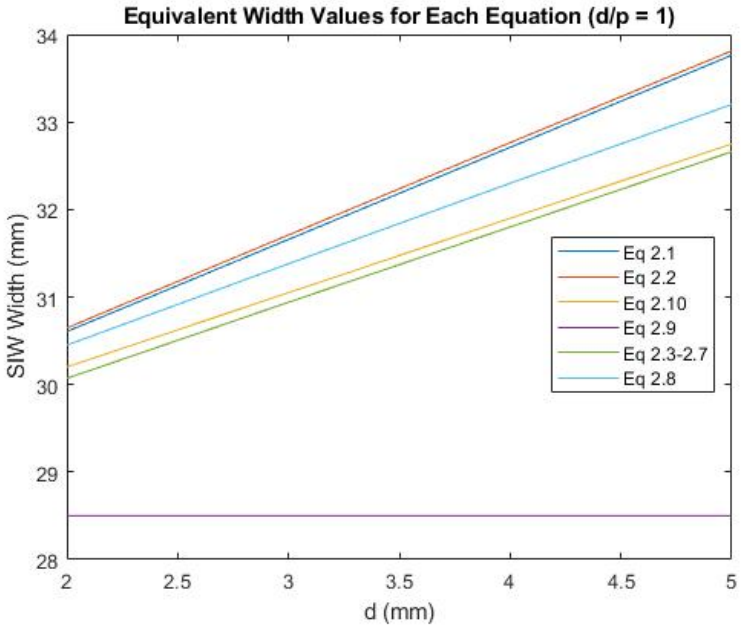


(c)

Figure 3.1: SIW equivalent widths for (a) $\frac{d}{p} = 0.6$, (b) $\frac{d}{p} = 0.8$, and (c) $\frac{d}{p} = 1$ when $W_{waveguide}$ = 28.5mm

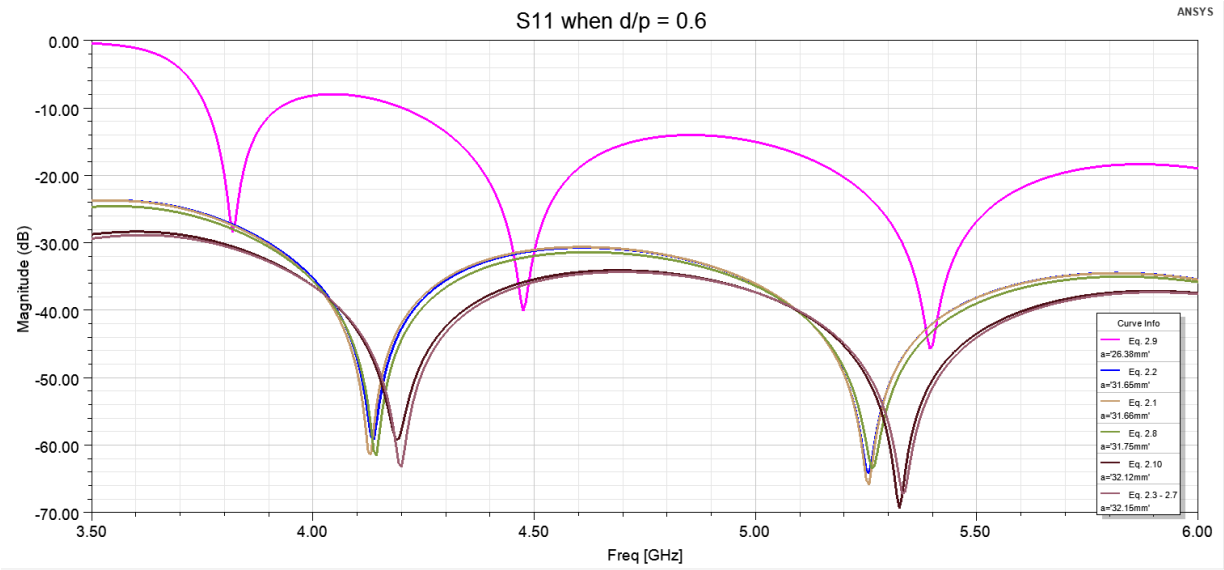
S11 when d/p = 0.6
ANSYS
0.00
-10.00
-20.00
-30.00
-40.00
-50.00
-60.00
-70.00
Magnitude (dB)
3.50
4.00
4.50
5.00
5.50
6.00
Freq [GHz]
Curve Info
Eq. 2.9
a='26.38mm'
Eq. 2.2
a='31.65mm'
Eq. 2.1
a='31.66mm'
Eq. 2.8
a='31.75mm'
Eq. 2.10
a='32.12mm'
Eq. 2.3 - 2.7
a='32.15mm'

(a)

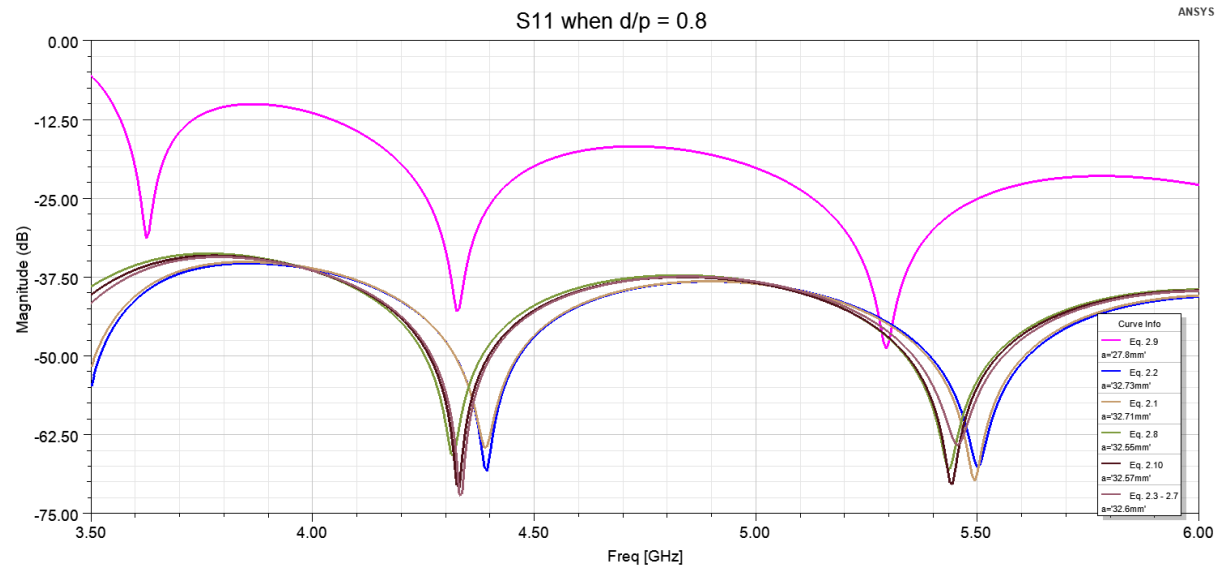
S11 when d/p = 0.8
ANSYS
0.00
-12.50
-25.00
-37.50
-50.00
-62.50
-75.00
Magnitude (dB)
3.50
4.00
4.50
5.00
5.50
6.00
Freq [GHz]
Curve Info
Eq. 2.9
a='27.8mm'
Eq. 2.2
a='32.73mm'
Eq. 2.1
a='32.71mm'
Eq. 2.8
a='32.55mm'
Eq. 2.10
a='32.57mm'
Eq. 2.3 - 2.7
a='32.6mm'

(b)

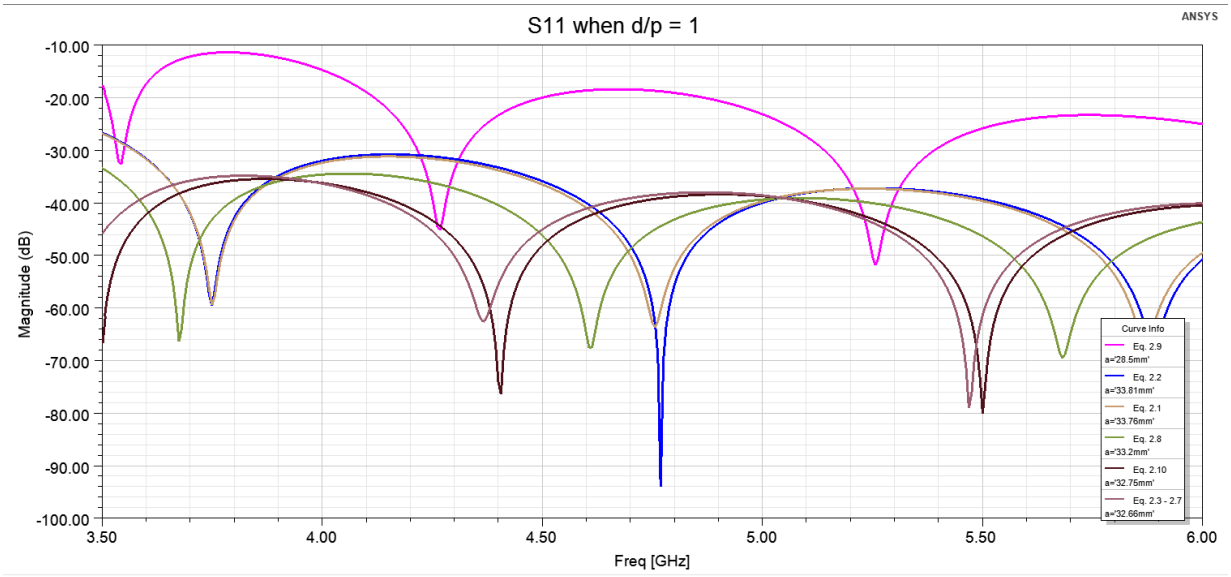


(c)

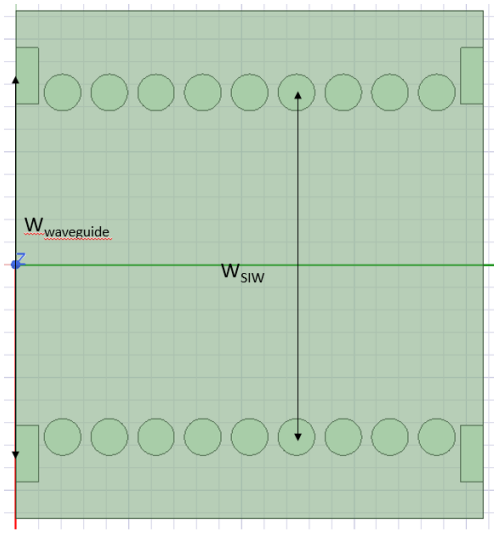


(d)

Figure 3.2: HFSS simulations for (a) $\frac{d}{p} = 0.6$, (b) $\frac{d}{p} = 0.8$, and (c) $\frac{d}{p} = 1$ when $W_{waveguide} = 28.5$ mm and d = 5 mm along with (d) the HFSS model for the simulations.

3.1 and the desired center frequency of 4 GHz, we can choose the pitch and diameter for the SIW. We initially assign the pitch to be 4.15 mm and diameter to be 2.7 mm.

We must check that these values satisfy the four rules. These $d$ and $p$ values clearly satisfy rules 1 and 3. To verify rules 2 and 4, we must find the guided wavelength. The guided wavelength can be found using equation 3.2 where $c$ is the speed of light, $f$ is the center frequency, $\epsilon_r$ is the dielectric constant, and $a_{waveguide}$ is the width of the waveguide. Here, we choose an waveguide cutoff frequency of 2.8 GHz, which gives us $a_{waveguide} =$ 28.5mm. The other parameters are: $\epsilon_r = 3.55$, and $f = 4$GHz with the resulting $\lambda_g$ being 55.61mm. With the guided wavelength we can find that $\frac{p}{\lambda_g}$ is 0.075, which satisfies rules 2 and 4. The corresponding SIW width can be found to be $a_{SIW} = 30.54$mm using equation 2.10.

$$\lambda_g = \frac{c}{f * \sqrt{\epsilon_r}} * \frac{1}{\sqrt{1 - (\frac{c}{2 * a_{waveguide} * f * \sqrt{\epsilon_r}})^2}} \tag{3.2}$$

The next step in the design is to incorporate the transition. Here, we elect to use a tapered transmission line to match the 50Ω input microstrip line to the SIW. [22] introduces equations 3.3 to 3.6, which provide initial dimensions for the taper. The dimensions for the taper are then optimized in HFSS to achieve the best possible match in the frequency band of choice. Here, $L_{t-v}$ is the length of the taper, $w_{t-v}$ is the width of the taper at the SIW interface, $p_1$ is the pitch between the periodic vias and the additional vias used for

the transition, $w_1$ is the pitch between the two added vias, $w_m$ is the width of the input microstrip line, and $\lambda_{g-ms}$ is the guided wavelength of the microstrip line. The width of the 50Ω microstrip line is found to be 1.2mm.

$$L_{t-v} = 0.2368 * \lambda_{g-ms} \tag{3.3}$$

$$w_{t-v} = w_m + 0.1547 * a_{SIW} \tag{3.4}$$

$$p_1 = 0.6561 * p \tag{3.5}$$

$$w_1 = 0.8556 * a_{SIW} \tag{3.6}$$

The values determined by equations 3.3 to 3.6 and the optimized values for performance can be seen in Table 3.2. Figure 3.3 shows the taper, while Figures 3.4 and 3.5 show the initial and optimized results, respectively.

Table 3.2: The tapered transition dimensions for the initial calculations and optimized performance.

| | $L_{t-v}(mm)$ | $w_{t-v}(mm)$ | $p_1(mm)$ | $w_1(mm)$ | $a_{SIW}(mm)$ | d (mm) | p (mm) |
|---|---|---|---|---|---|---|---|
| Initial | 10.62 | 5.93 | 2.72 | 26.15 | 30.54 | 2.7 | 4.15 |
| Optimized | 11.8 | 4.88 | 2.605 | 23.39 | 30.54 | 3.256 | 4.15 |

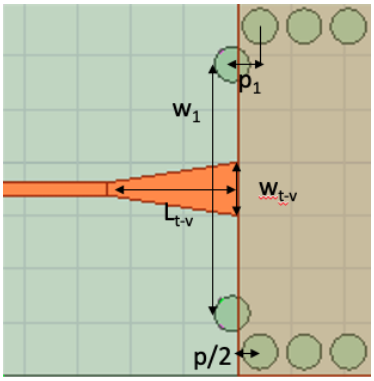


Figure 3.3: The taper transition model

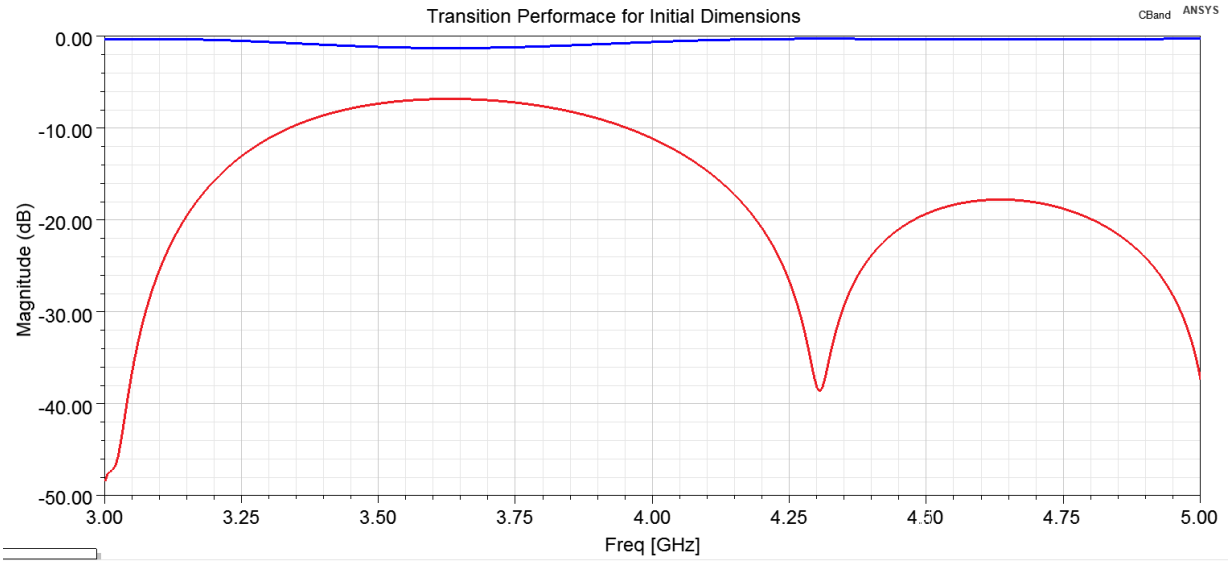


Figure 3.4: Performance of the transition using values obtained from equations 3.13 to 3.16

Based on the results, we can see that the equations do not provide us with a sufficient performance, but are a good starting point. The optimized performance gives a response better than -30 dB at 4GHz, a -20 dB fractional bandwidth of 40% between 3.1 GHz and

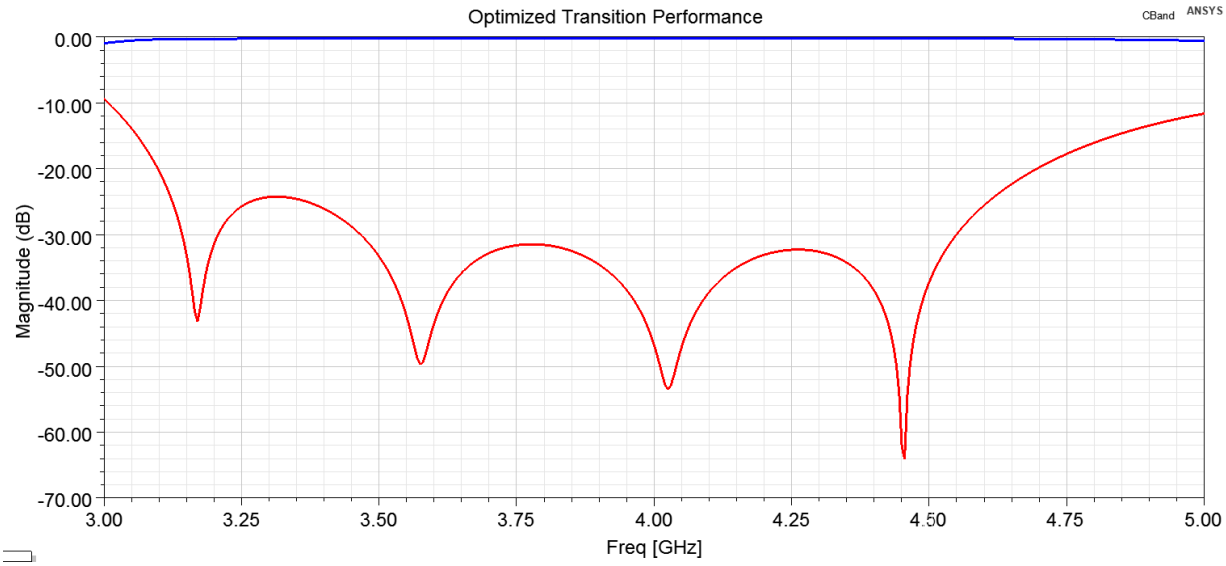


Figure 3.5: Performance of the optimized transition

4.7GHz, and an insertion loss within this band of -0.326 dB.

### 3.3.2 The Coupling Matrix

The design of this quasi-elliptic filter requires the use of cross-coupled resonators. Coupling is either defined as electric (capacitive) or magnetic (inductive); the nature of the coupling is determined by the mechanism by which two resonators are coupled. In SIWs, the main path coupling mechanisms used are irises, meaning that the coupling is inductive. In order to achieve an elliptic response, we consider the use of a capacitive quadruplet with an electric coupling between the first and fourth resonators of the filter.

The coupling matrix is used in this design to help determine the required K-impedance inverter values and to aid with tuning. The K-impedance values will then be taken and used as a reference for the design of the main path of the circuit. The purpose of this method is to model the filter in such a way that the cross-coupling can be included with minimal tuning to the rest of the filter. As a point of comparison, the coupling matrix will also be used to design the filter directly. Equations 3.7 - 3.9 are used to find the initial N+2 x N+2 coupling matrix values for the four-pole filter, assuming an RL of 25dB. The ideal Chebyshev response of this filter is obtained through ADS and can be seen in Figure 3.6.

$$R_1 = \frac{1}{g_0 * g_1} \tag{3.7}$$

$$R_N = \frac{1}{g_N * g_{N+1}} \tag{3.8}$$

$$M_{j,j+1} = \frac{1}{\sqrt{g_j * g_{j+1}}} \tag{3.9}$$

$$j = 1, 2, ..., N-1$$

$$\begin{pmatrix} 0 & 1.326 & 0 & 0 & 0 & 0 \\ 1.326 & 0 & 1.04 & 0 & 0 & 0 \\ 0 & 1.04 & 0 & 0.771 & 0 & 0 \\ 0 & 0 & 0.771 & 0 & 1.04 & 0 \\ 0 & 0 & 0 & 1.04 & 0 & 1.326 \\ 0 & 0 & 0 & 0 & 1.326 & 0 \end{pmatrix}$$

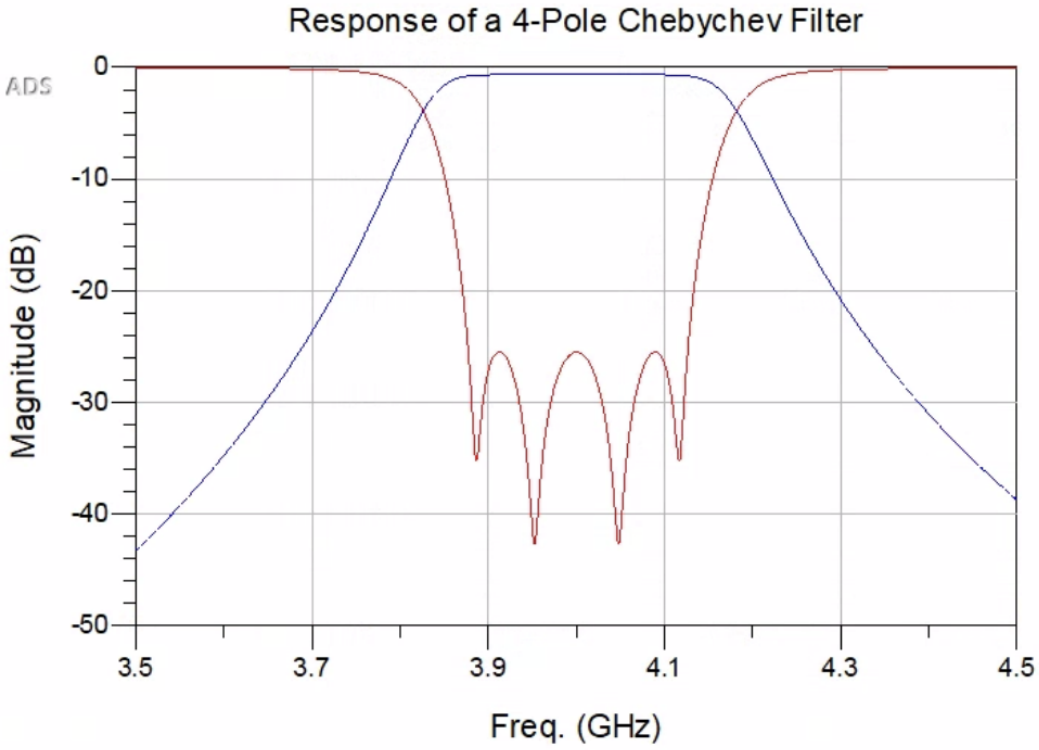


Figure 3.6: Ideal response of the 4-pole Chebychev filter in ADS

Having calculated the initial values, we can now look at incorporating the cross-coupling

into the ideal response. Alterations, however, must be made to the other coupling coefficients to compensate when this is done. Using the ADS model shown in Figure 3.7, we determine the ideal response for the 4-pole quasi-elliptic filter. The corresponding N+2 by N+2 coupling matrix is shown below, with the ideal response being presented in Figure 3.8. It can be seen that by negatively coupling resonators one and four, we can achieve one transmission zero on each side of the passband. Figure 3.9 shows the signal flow diagram for this filter, with the black lines being positive couplings and the red line being negative coupling. Only $M_{23}$ required significant change with the addition of $M_{14} = M_{41}$ = -0.19.

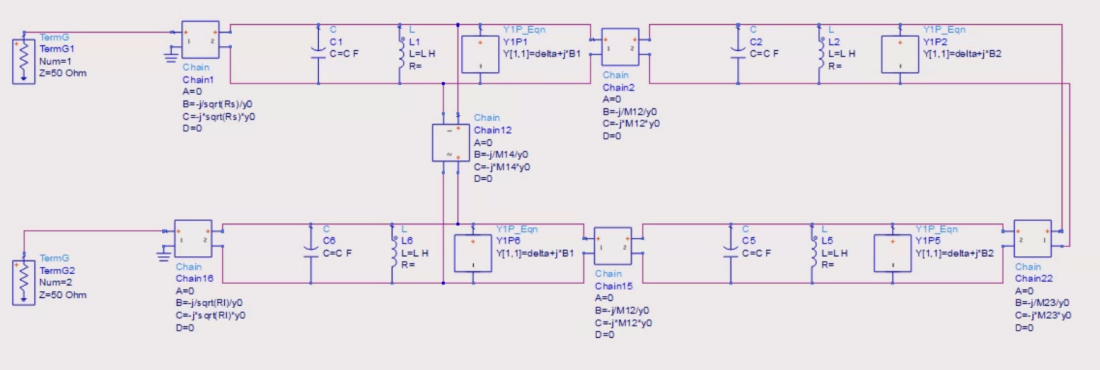


Figure 3.7: ADS model for the 4-pole quasi-elliptic filter

The ADS model uses the coupling matrix model by converting to a system of J-admittance inverters. This is done by directly substituting the coupling coefficients into the 2 x 2 J-admittance matrix. Here, each block represents the inter-resonator coupling, while the shunt elements represent the resonator itself and implement the bandpass transformation.

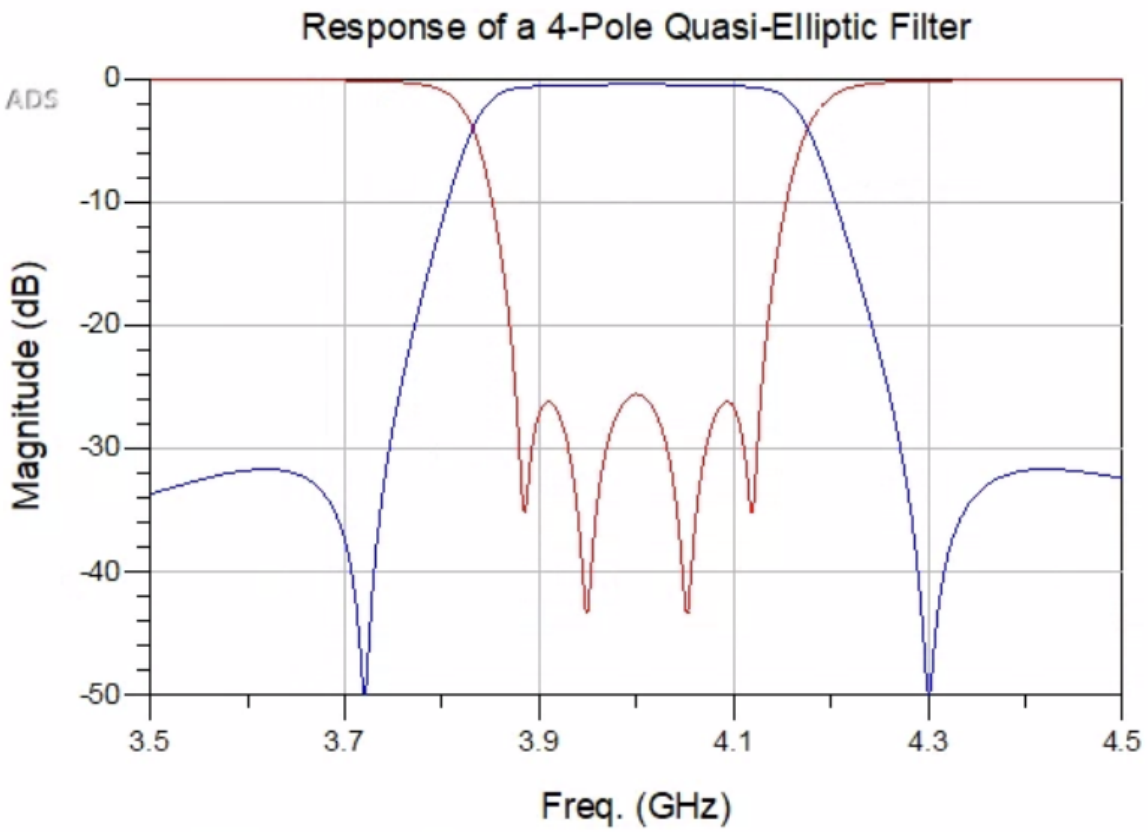


Figure 3.8: Ideal response of the 4-pole quasi-elliptic filter in ADS

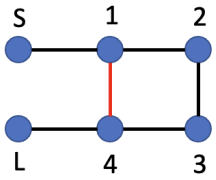


Figure 3.9: Signal flow diagram for the 4-pole quasi-elliptic filter

$$\begin{pmatrix} 0 & 1.152 & 0 & 0 & 0 & 0 \\ 1.152 & 0 & 1.02 & 0 & -0.19 & 0 \\ 0 & 1.02 & 0 & 0.851 & 0 & 0 \\ 0 & 0 & 0.851 & 0 & 1.02 & 0 \\ 0 & -0.19 & 0 & 1.02 & 0 & 1.152 \\ 0 & 0 & 0 & 0 & 1.152 & 0 \end{pmatrix}$$

### 3.3.3 K-Impedance Inverter Design Method

The K-impedance inverter is the ideal tool for designing conventional waveguide Chebyshev filters. Figure 3.10 shows a modified equivalent circuit of the K-impedance inverter. Since we are designing a quasi-elliptic filter, we are required to implement cross-coupling between the first and fourth resonators, which requires the use of a folded topology, similar to that seen in Figure 2.7. With this folded topology, we can accurately obtain the resonator lengths and iris widths for every iris, except between resonators two and three. This is because the width of the SIW before and after the bend will remain constant as $a_{SIW}$, while the width of the forward path from resonators two and three will differ. This means that the iris width will be more limited in its range. To solve this, the dimensions of all resonators and irises will be found using the K-impedance model as normal, but the third

iris will be found again using the length of resonator two as the new resonator width. The cross-coupling will not be implemented at this stage, and therefore the following results will be based purely on the sequential couplings

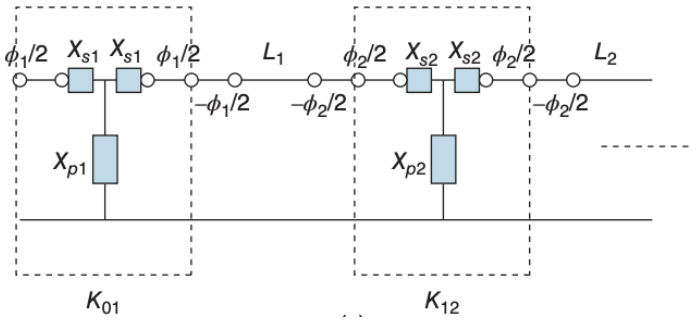


Figure 3.10: The modified equivalent circuit for a waveguide using K-impedance inverters. [2]

The K-impedance inverter values can be calculated using equations 3.10-12, where $W_\lambda$ is the guided wavelength and $Z_o$ is the characteristic impedance.

$$\frac{K_{01}}{Z_o} = M_{01} * \sqrt{\frac{\pi * W_\lambda}{2}} \tag{3.10}$$

$$\frac{K_{i,i+1}}{Z_o} = M_{i,i+1} * \frac{\pi * W_\lambda}{2} \tag{3.11}$$

$$\frac{K_{N,N+1}}{Z_o} = M_{N,N+1} * \sqrt{\frac{\pi * W_\lambda}{2}} \tag{3.12}$$

The calculated K-impedance inverter values can be seen in Table 3.3. Using HFSS, a lookup table was created to determine the iris widths and resonator lengths. Equations

3.13-3.15 were used to determine the K, $\phi$, and $l_r$. The lookup table can be found in appendix A.

From the lookup table, we are able to extract the dimensions for the SIW filter. It can be seen that when using the guided wavelength at 4 GHz (55.61 mm) to find $l_r$, the response is shifted up in frequency, however, when the guided wavelength at the lower band-edge (59.3 mm at 3.875 GHz) is used, the response is centered as expected. This is likely because the K-impedance inverter is ideal for narrowband filters ($\leq 1\%$), however, we are designing for 4.2%. Table 3.4 shows the difference in dimensions for the two guided wavelengths. Figure 3.11 shows the EM results of each compared to the ideal result from ADS.

Table 3.3: The calculated K-impedance inverter values.

| Coupling index (i,j) | K | Corresponding M |
|---|---|---|
| S,1 = 4,L | 0.5064 | 1.152 |
| 1,2 = 3,4 | 0.1971 | 1.02 |
| 2,3 | 0.1644 | 0.851 |

$$\frac{K}{Z_o} = \left| \tan\frac{\phi}{2} + \arctan\frac{X_s}{Z_o} \right| \tag{3.13}$$

$$\phi = -\arctan(2 * \frac{X_p}{Z_o} + \frac{X_s}{Z_o}) - \arctan(\frac{X_s}{Z_o}) \tag{3.14}$$

$$l_r = \frac{\lambda_g}{2\pi}\left[\pi + \frac{1}{2}(\phi_r + \phi_{r+1})\right] \tag{3.15}$$

Table 3.4: The dimensions of the SIW filter without cross-coupling using the K-impedance inverter method.

| | $L_1(mm)$ | $L_2(mm)$ | $Iris_1(mm)$ | $Iris_2(mm)$ | $Iris_3(mm)$ |
|---|---|---|---|---|---|
| $\lambda_{gL}$ | 19.75 | 22.96 | 17.1 | 12.31 | 11.56 |
| $\lambda_{go}$ | 18.52 | 21.53 | 17.1 | 12.31 | 11.53 |

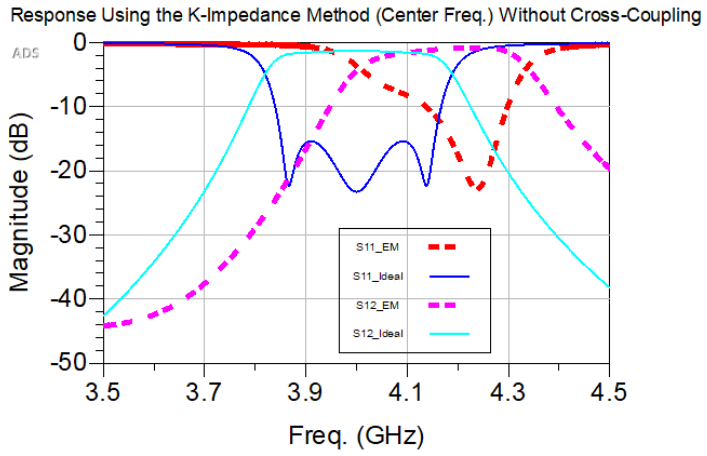


(a)

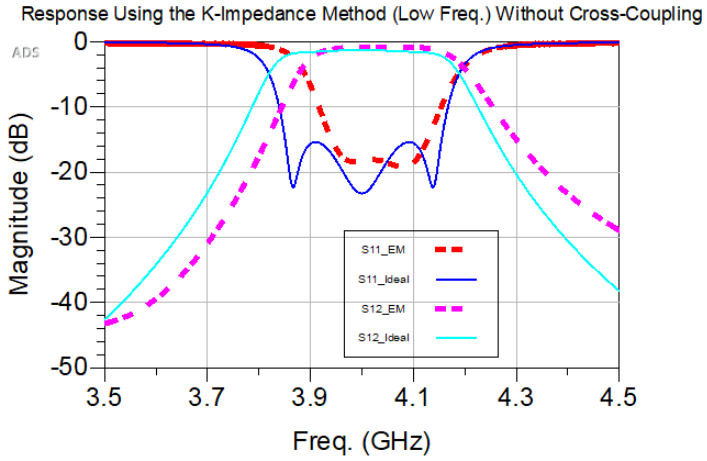


(b)

Figure 3.11: The EM simulation results of the filter with no cross-coupling using K-impedance inverter design method for (a) $\lambda_g = 55.61mm$ and (b) $\lambda_g = 59.3mm$

### 3.3.4 Coupling Matrix Method

The coupling matrix design method is a useful technique when designing filters that contain resonant cavities. While the K-impedance inverter method is preferred for SIWs, the coupling matrix method allows for easier consideration of the folded topology. The drawback of the coupling matrix method is that loading cannot be accounted for in the design, a limitation that impacts accuracy.

When designing using coupling matrix analysis, the physical dimensions of the filter can be separated into three categories: resonator dimensions, inter-resonator coupling, and input/output coupling. The inter-resonator coupling can be determined using the electrical wall and magnetic wall to find $f_e$ and $f_m$ respectively. Equation 3.16 can be used to find the coupling coefficient if the coupling is inductive, or equation 3.17 can be used if the coupling is capacitive. Eigenmode analysis is performed to determine the coupling coefficients.

$$M_{ij} = \frac{f_o}{BW}\frac{f_e^2 - f_m^2}{f_e^2 + f_m^2} \tag{3.16}$$

$$M_{ij} = \frac{f_o}{BW}\frac{f_m^2 - f_e^2}{f_e^2 + f_m^2} \tag{3.17}$$

The input/output coupling is determined through the use of the reflected group delay (see Section 4.2.2). The cavity resonance is adjusted as needed throughout the design.

The design process will begin by performing reflected group delay (RGD) analysis to determine the width of the first iris and length of the first resonator, after which eigenmode analysis will be performed to determine the second and third iris widths along with the length of the second cavity.

The dimensions determined by the RGD technique and the eigenmode analysis can be seen in Table 3.5. The EM simulation results compared to the ideal response can be seen in Figure 3.12. The eigenmode analysis table with corresponding dimensions can be found in Appendix A.

Table 3.5: The dimensions of the SIW filter without cross-coupling using the coupling matrix method.

| $L_1(mm)$ | $L_2(mm)$ | $Iris_1(mm)$ | $Iris_2(mm)$ | $Iris_3(mm)$ |
|---|---|---|---|---|
| 19.4 | 23.7 | 17.78 | 12.08 | 12.3 |

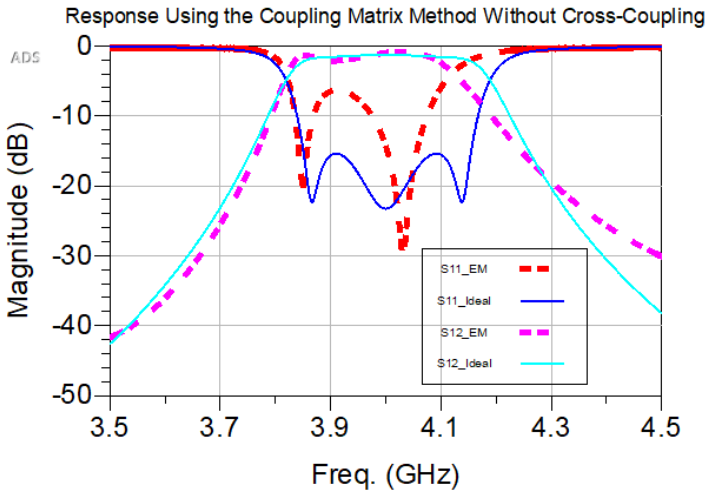


Figure 3.12: The EM simulation results of the filter with no cross-coupling using coupling matrix design method

### 3.3.5 Hybrid Design Method

As explained in Section 3.3.3, the K-impedance inverter proves to be an ideal method of choice for SIW resonators positioned in a straight line. However, the problem of accurately determining the dimensions of the iris on folded portions remains, and therefore, we investigate a hybrid method of designing folded SIW filters where the K-impedance inverter method is combined with the coupling matrix method. The K-impedance inverter will serve to determine the resonator and iris dimensions prior to the fold, and the eigenmode analysis will be used to determine the dimensions of the iris in the fold. During the eigenmode analysis, the length of the second resonator is left as the value determined by the

K-impedance inverter. Figure 3.13 shows the results of the hybrid method and Table 3.6 shows the dimensions.

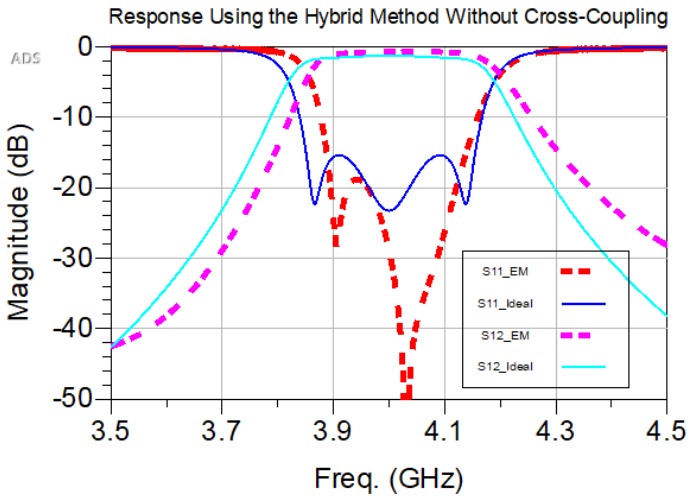


Figure 3.13: The EM simulation results of the filter with no cross-coupling using the hybrid method

Table 3.6: The initial (from hybrid method) and adjusted dimensions for the 4-pole quasi-elliptic filter without cross coupling.

| | $L_1(mm)$ | $L_2(mm)$ | $Iris_1(mm)$ | $Iris_2(mm)$ | $Iris_3(mm)$ |
|---|---|---|---|---|---|
| Initial | 19.75 | 22.96 | 17.1 | 12.31 | 12.2 |
| Adjusted | 20.3 | 23.03 | 17.1 | 12.5 | 13.03 |

It can be seen that the EM simulation results still do not match the desired ideal circuit

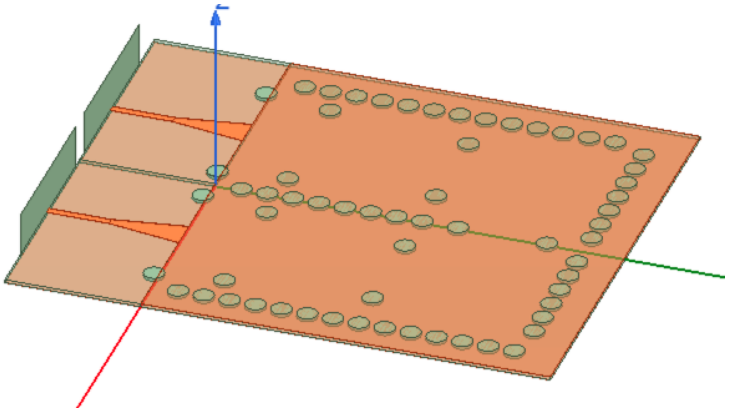

(a)

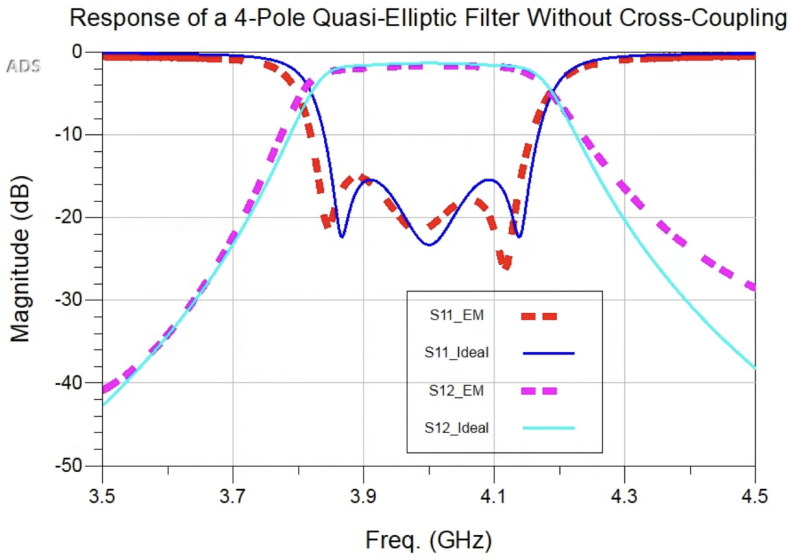


(b)

Figure 3.14: The (a) model and (b) ideal and simulated results of the 4-pole quasi-elliptic filter based on the K-impedance inverter values in Table 3.3 without cross coupling.

simulation results. To fix this, some fine tuning is performed on the irises and resonators. The adjusted dimensions can be seen in Table 3.6 and a comparison of the dimensions across all methods can be seen in Table 3.7. The filter model and adjusted EM simulated results can be seen in Figure 3.14.

Table 3.7: The dimensions for the 4-pole quasi-elliptic filter without cross coupling from each different method.

| | $L_1(mm)$ | $L_2(mm)$ | $Iris_1(mm)$ | $Iris_2(mm)$ | $Iris_3(mm)$ |
|---|---|---|---|---|---|
| K-Impedance ($\lambda_{gL}$) | 19.75 | 22.96 | 17.1 | 12.31 | 11.56 |
| K-Impedance ($\lambda_{go}$) | 18.52 | 21.53 | 17.1 | 12.31 | 11.53 |
| Coupling Matrix | 19.4 | 23.7 | 17.78 | 12.08 | 12.3 |
| Hybrid | 19.75 | 22.96 | 17.1 | 12.31 | 12.2 |
| Final | 20.3 | 23.03 | 17.1 | 12.5 | 13.03 |

When comparing the three methods, it is clear that the hybrid approach produces the most accurate results. It is worth noting that in each case, it is not possible to account for the loading from the third iris on the first resonator or to accurately determine the width of the iris in the fold. Other sources of error come from the fact that both the K-impedance and coupling matrix methods are more accurate with narrowband filters ($\leq 1\%$). It can

be concluded, then, that the hybrid and K-impedance methods are good choices when designing folded SIW filters with the requirement that $iris_{Folded}$ and $L_{(N/2-1)}$ be adjusted assuming that the order of the filter, N, is even.

### 3.3.6 Cross-Coupling

The last step prior to fine-tuning is to incorporate the cross-coupling. To accomplish this, we must enforce a negative coupling between resonators one and four. We can create this by incorporating a mixed-coupling structure, which means that we have a method of positive and negative coupling in the structure that is adjustable. The positive coupling will be in the form of irises between resonators one and four, and the negative coupling will be an etched CPW on the top metal layer. The negative coupling introduced by the etched CPW must be large enough to overtake the positive coupling that occurs between resonators one and four. We can confirm the presence of negative coupling by observing the magnetic fields of two SIW cavities split by an iris. Figure 3.15 shows the low and high mode of the cavities coupled by just an iris, while Figure 3.16 shows the low and high modes of the cavities coupled by both an iris and an etched CPW. We can see that the field distribution for the inductive coupling is rotating in the same direction for the low mode and opposite direction for the high mode; for the capacitive coupling, the low mode has the field distributions in the opposite direction, while in the high mode, they are in

the same direction. This indicates that negative coupling has been achieved by the etched CPW line.

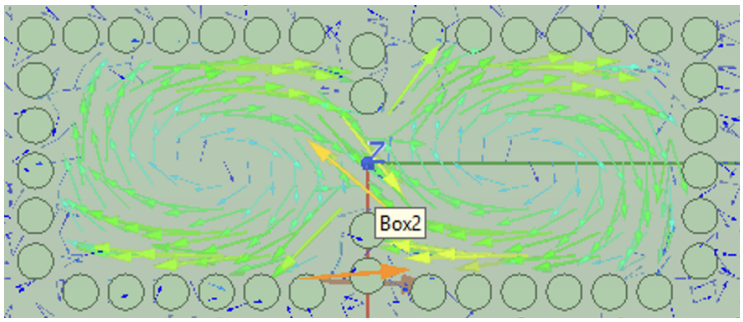


(a)

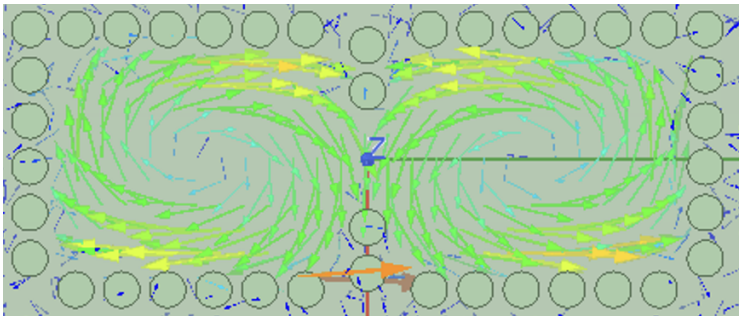

(b)

Figure 3.15: The field distributions for positive coupling in the (a) low mode and (b) high mode.

There are four adjustable variables to help find the required coupling coefficient: the length of the CPW, the width of the center signal path, the width of the etch, and the iris width. We limit the iris width to it's minimum in order to reduce inductive coupling. Figure 3.17 shows the effect on the strength of the coupling when each aspect of the coupling structure is changed. As the length of the CPW line, the width of the CPW line, and the width of

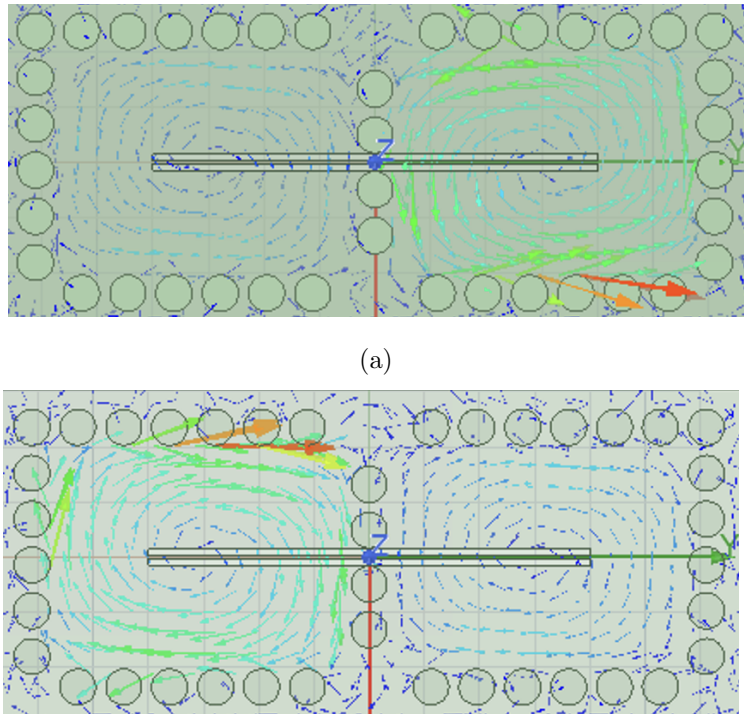

(a)

(b)

Figure 3.16: The field distributions for negative coupling in the (a) low mode and (b) high mode.

the CPW increase, the cross-coupling becomes more negative, resulting in the transmission zeros being pushed closer to the passband. As the width of the iris increases, the positive coupling becomes stronger, resulting in the transmission zeros being pushed away.

The etched CPW line is added to the full model obtained in Section 3.3.5 and fine-tuned to achieve the desired result using ADS and HFSS together. The model was simulated with Rogers4003C with a loss tangent of 0.0027, thickness of 0.508mm, and dielectric constant of 3.55. Figure 3.18 shows the simulated results in HFSS and Figure 3.19a shows the model

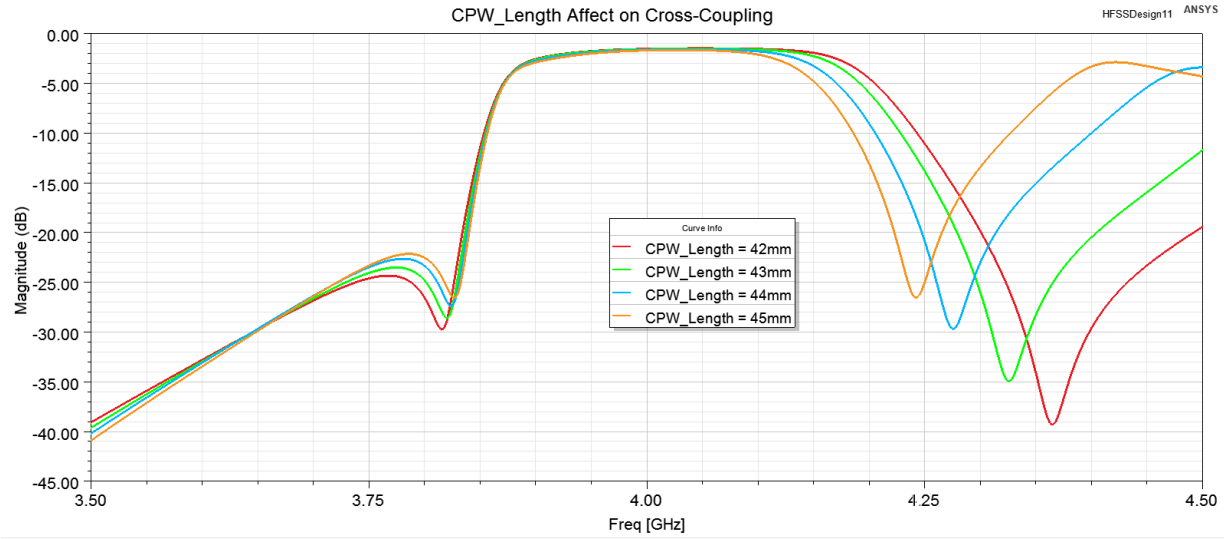


(a)

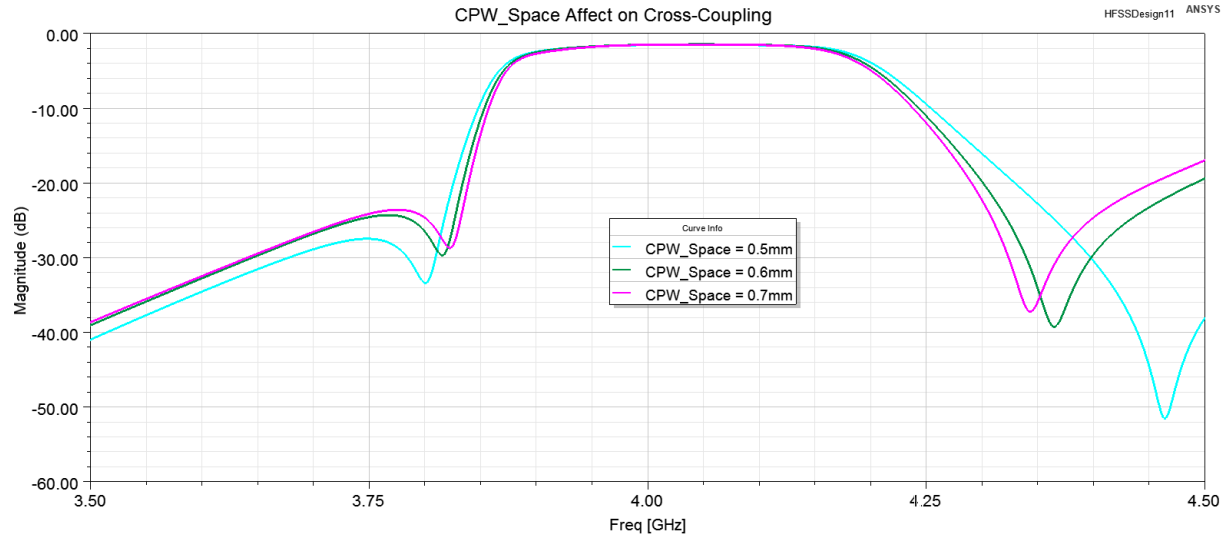


(b)

dimensions while 3.19b shows the fine dimensions for the CPW etch. The dimensions of the filter are listed in Table 3.8, where the lengths and iris widths are all from the edge of

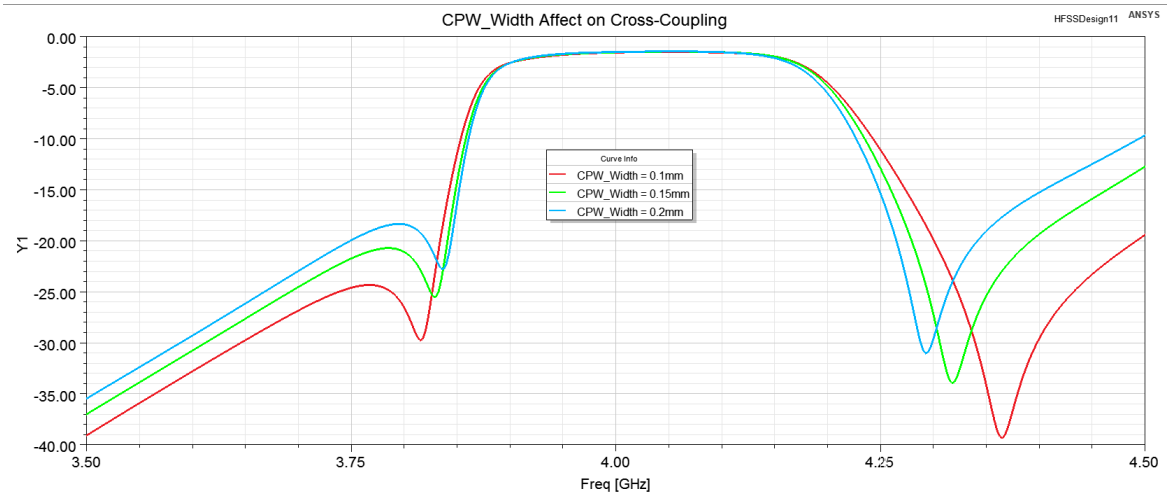


(c)

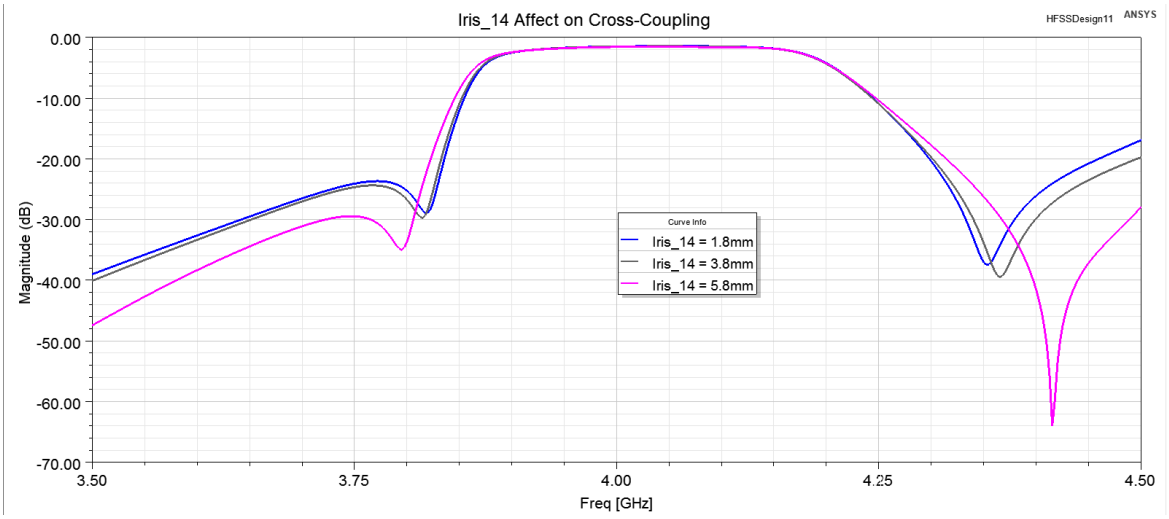


(d)

Figure 3.17: The strength of the cross-coupling when there is a change in (a) $CPW_{Length}$, (b) $CPW_{Space}$, (c) $CPW_{Width}$, and (d) $Iris_{14}$.

the vias, and $a_s$ is from the center of the vias.

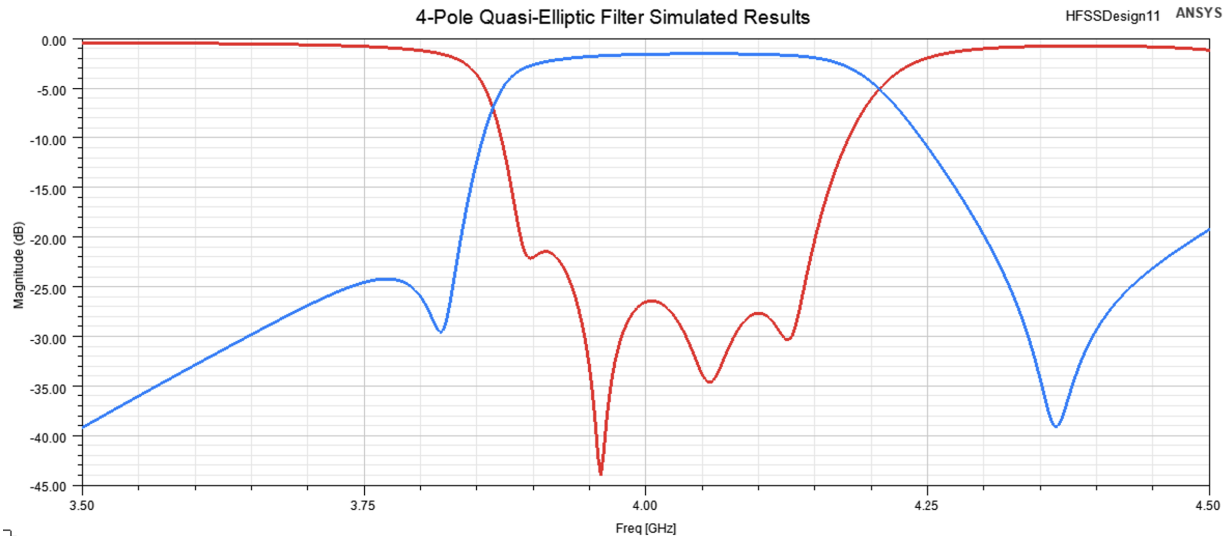


Figure 3.18: The EM simulated results of the 4-pole quasi-elliptic filter

Table 3.8: The dimensions for the 4-pole quasi-elliptic filter with cross coupling.

| $a_s$ | $L_1$ | $L_2$ | $Iris_1$ | $Iris_2$ | $Iris_3$ | $Iris_{14}$ | $CPW_{Length}$ | $CPW_{Width}$ | $CPW_{Space}$ |
|---|---|---|---|---|---|---|---|---|---|
| 30.54mm | 20.8mm | 21.5mm | 16mm | 12.8mm | 14.5mm | 1.8mm | 40.8mm | 0.2mm | 0.6mm |

The insertion loss of the EM results is 1.57dB (Q = 155), return loss is better than -20dB between 3.9GHz and 4.15GHz, and the zeros appear at 3.82GHz and 4.36GHz. There is some asymmetry present in the zeros; this can be corrected by introducing negative coupling between resonators one and three or two and four, but this would result in the degradation of the return loss performance. As a result, it was decided that this asymmetry

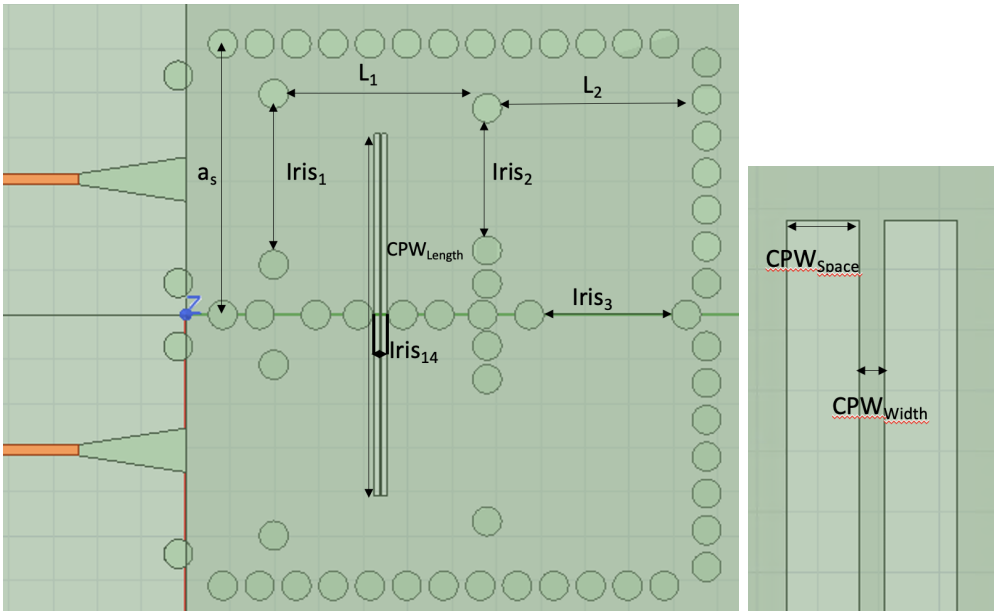


(a) (b)

Figure 3.19: The EM model of the (a) filter and (b) CPW etch.

would not be corrected.

### 3.3.7 Measurements

Figure 3.20 shows both the fabricated filter along with the measured and EM simulation results compared to the simulated results. The shape of the filter and positioning of the transmission zeros is clear and indicates that the coupling structure is used successfully to introduce negative cross-coupling. The original filter that had been sent for fabrication was designed and simulated using a dielectric constant of 3.38. It was only noticed after

placing the PCB fabrication order that it is advised to design for a dielectric constant of 3.55. There is slightly more loss in the passband than expected, and can be accredited to an error in the value for the loss tangent and return loss degradation. Fabrication tolerances and errors contribute to the error in magnitude of the return loss. The testing setup utilized a Keysight PNA with coaxial cables that were connected to the filter using SMA connectors.

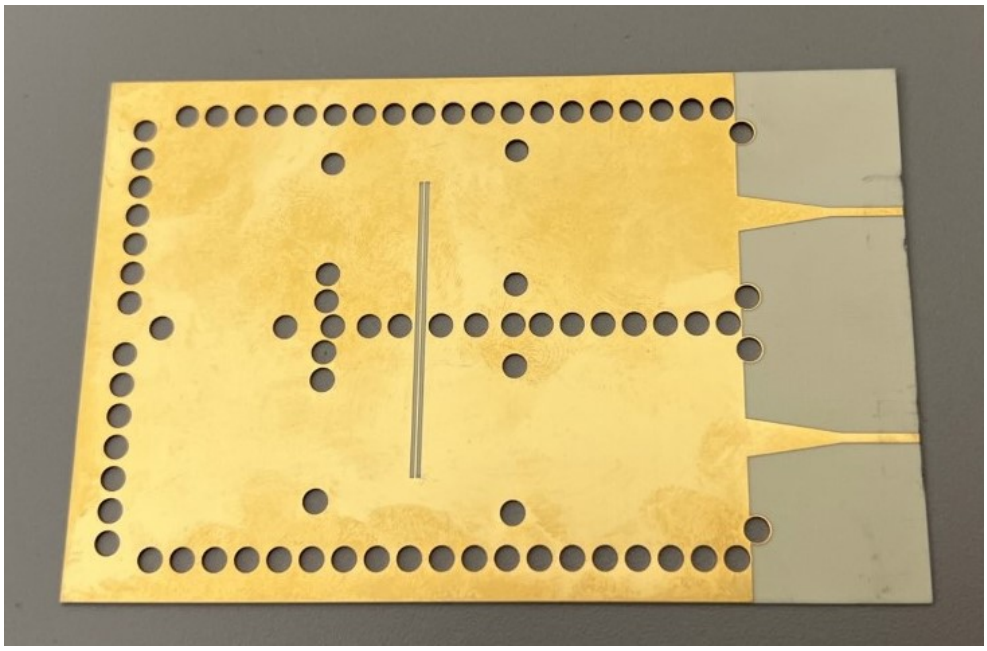

(a)

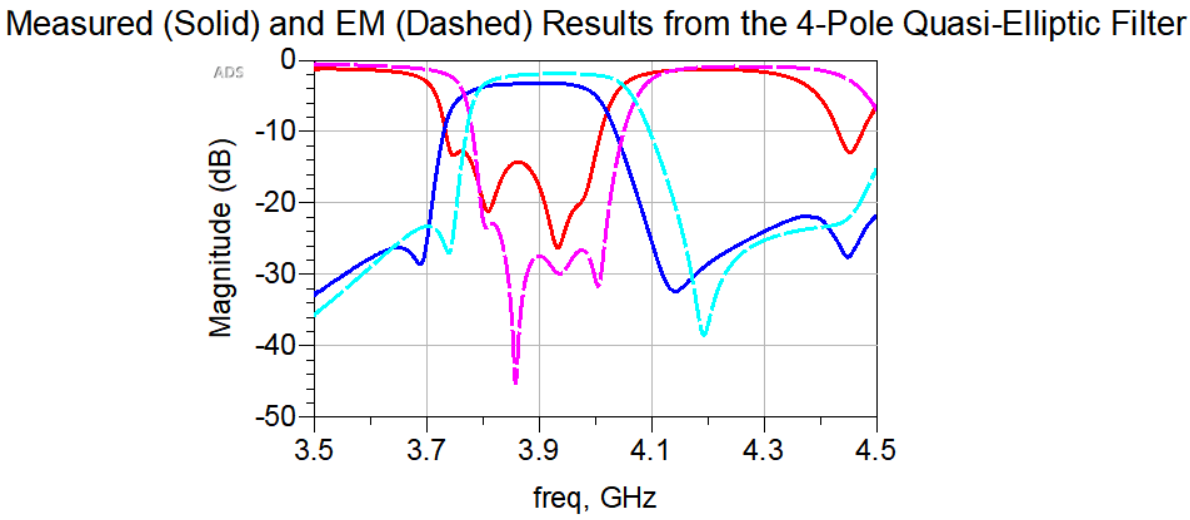


(b)

Figure 3.20: The (a) final fabricated 4-pole quasi-elliptic filter and (b) the measured and simulated results.

## 3.4 Dual-Band SIW Filter Design

### 3.4.1 Realization of the Dual-Band

Dual-band filters can be realized using any of the four methods mentioned in Section 2.2. For the design of this SIW dual-band filter, we choose to insert an in-band transmission zero into an 8-pole 5% bandwidth filter. The transmission zero will split the filter response into two 4-pole responses with narrower bandwidths.

The coupling matrix values of the 8-pole filter can be found using equations 3.7 - 3.9 with g-parameters for a -25dB Chebyshev filter. The same methods used to determine the coupling coefficients for the 4-pole quasi-elliptic filter are used to determine those required to split the 8-pole filter into two separate 4-pole passbands. The resulting N+2 x N+2 coupling matrix is shown below, along with the ideal simulation results in Figure 3.21. The signal flow diagram corresponding to the coupling matrix can be seen in Figure 3.22.

$$\begin{pmatrix} 0 & 0.92 & 0 & 0 & 0 & 0 & 0 & 0 & 0 & 0 \\ 0.92 & 0 & 0.942 & 0 & 0 & 0 & 0 & 0 & 0 & 0 \\ 0 & 0.942 & 0 & 0.586 & 0 & 0 & 0 & 0 & 0 & 0 \\ 0 & 0 & 0.586 & 0 & 0.54 & 0 & 0.52 & 0 & 0 & 0 \\ 0 & 0 & 0 & 0.54 & 0 & -0.03 & 0 & 0 & 0 & 0 \\ 0 & 0 & 0 & 0 & -0.03 & 0 & 0.54 & 0 & 0 & 0 \\ 0 & 0 & 0 & 0.52 & 0 & 0.54 & 0 & 0.586 & 0 & 0 \\ 0 & 0 & 0 & 0 & 0 & 0 & 0.586 & 0 & 0.942 & 0 \\ 0 & 0 & 0 & 0 & 0 & 0 & 0 & 0.942 & 0 & 0.92 \\ 0 & 0 & 0 & 0 & 0 & 0 & 0 & 0 & 0.92 & 0 \end{pmatrix}$$

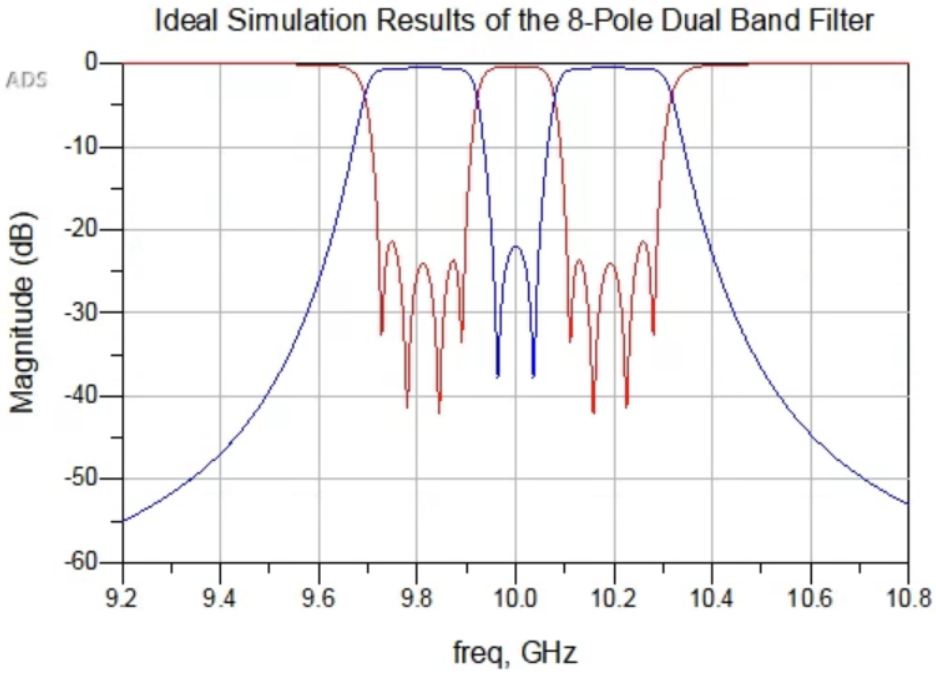


Figure 3.21: The ideal simulated results of the 8-pole dual-band filter

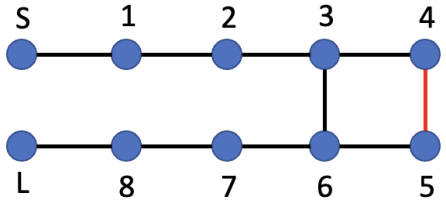


Figure 3.22: The signal flow diagram of the 8-pole dual-band filter where positive coupling is black and negative coupling is red

### 3.4.2 SIW and Transition Design

The design of the SIW and microstrip-to-SIW transition follows the same methods as Section 3.3.1. The simulation results of the transition can be seen in Figure 3.23, with the dimensions of the transition below that in Table 3.9. The transition performance shows an insertion loss of 0.34 dB and a return loss lower than 25 dB between 8.5 GHz and 12.7 GHz, providing a very good match for our frequencies of interest.

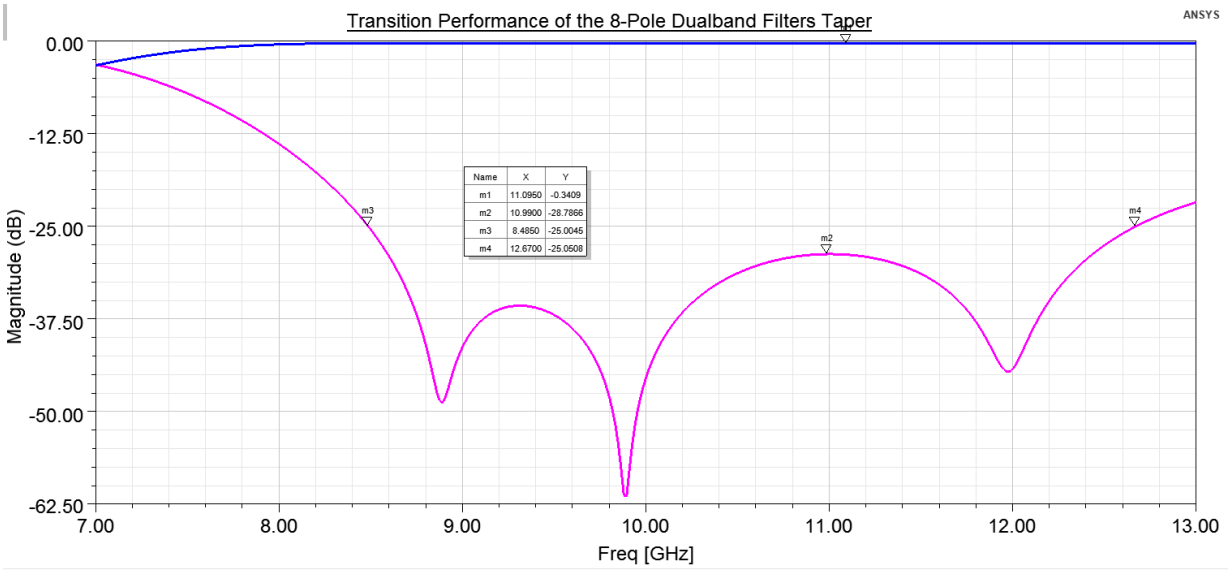


Figure 3.23: The performance of the tapered transition for the 8-pole dual-band filter

Table 3.9: The tapered transmission dimensions for the initial calculations and optimized performance.

| Dimension | $L_{t-v}$ | $w_{t-v}$ | $p_1$ | $w_1$ | $a_{SIW}$ | d | p |
|---|---|---|---|---|---|---|---|
| Value (mm) | 4 | 3.1 | 0.8 | 1.2 | 12.45 | 1.23 | 1.7 |

### 3.4.3 Resonator and Iris Design Using the Hybrid Method

The design of the dual-band filter uses the hybrid design method in Section 3.3.5 to initially realize all dimensions, except for the folded iris. In this case, the negative coupling is in the forward path from resonator four to five. Fortunately, the value of the coupling is small enough that, for this stage, we can assume it is zero. Because there is positive coupling between resonators three and six, the K-impedance inverter method will be used to determine the length of the resonators, $iris_1$, $iris_2$, $iris_3$, and $iris_4$ while eigenmode analysis will be used to find $iris_5$ and $iris_{36}$. Using the tables in Appendix A, we can extract the initial dimensions for the dual-band filter. These dimensions can be found in Table 3.10, with the EM simulation results in Figure 3.24. The dimensions here are from the edge of the vias, with the exception of $a_s$ It should be noted that these results do not include the dielectric loss of 0.0027. It will be shown later that the substrate chosen for this frequency of choice produces very high losses.

Table 3.10: The extracted dimensions when using the hybrid method.

| $a_s$ | $L_1$ | $L_2$ | $L_3$ | $L_4$ | $Iris_1$ | $Iris_2$ | $Iris_3$ | $Iris_4$ | $Iris_5$ | $Iris_{36}$ |
|---|---|---|---|---|---|---|---|---|---|---|
| 12.45mm | 8.2mm | 9.24mm | 9.46mm | 10mm | 5.86mm | 4.22mm | 3.7mm | 3.62mm | $\approx 0mm$ | 3.86mm |

It can be seen that the shape of the filter is beginning to form, but the results are not as accurate as expected. The transmission zero introduced is found to be shifted up in frequency, indicating that $L_4$ needs to be increased. The negative coupling will be introduced next, after which the filter will be tuned to an acceptable level of performance. The dimensions for the negative forward coupling structure are in Table 3.11, and the pre-tuned results can be seen in Figure 3.25.

Table 3.11: The dimensions of the etched CPW.

| $CPW_{Length}(mm)$ | $CPW_{Width}(mm)$ | $CPW_{Space}(mm)$ | $Iris_5(mm)$ |
|---|---|---|---|
| 15.5 | 0.2 | 0.2 | 2.82 |

The forward negative coupling provides a second transmission zero in the rejection band between the two passbands. This will allow for an acceptable level of rejection throughout the whole rejection band. This filter is then tuned, and the results without the dielectric loss are shown in 3.26a, while the results with loss are shown in 3.26b. The final dimensions

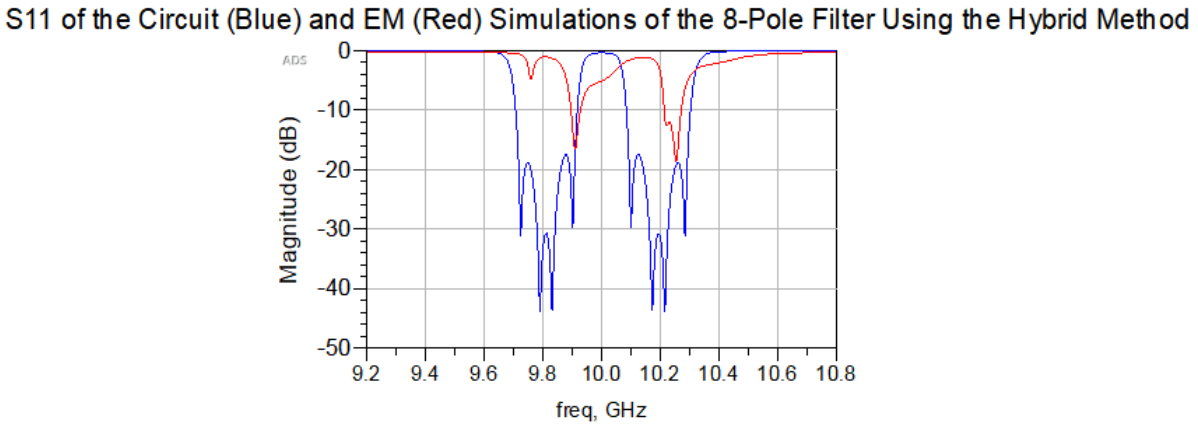


(a)

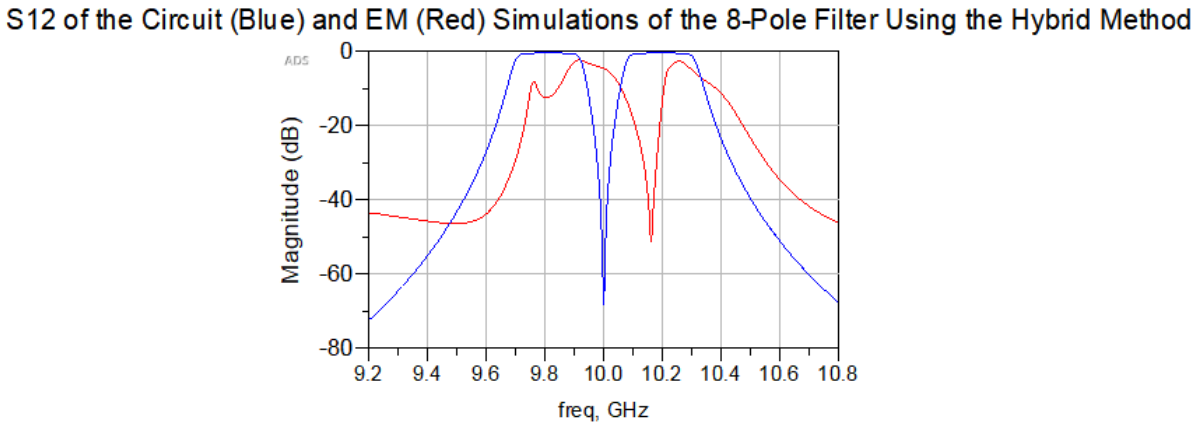


(b)

Figure 3.24: The result comparison for the circuit and EM simulations for (a) $S_{11}$ and $S_{12}$.

can be seen in Table 3.12 and the EM model in Figure 3.27.

Here we see the effects of the dielectric loss of 0.0027 on the response. It was realized

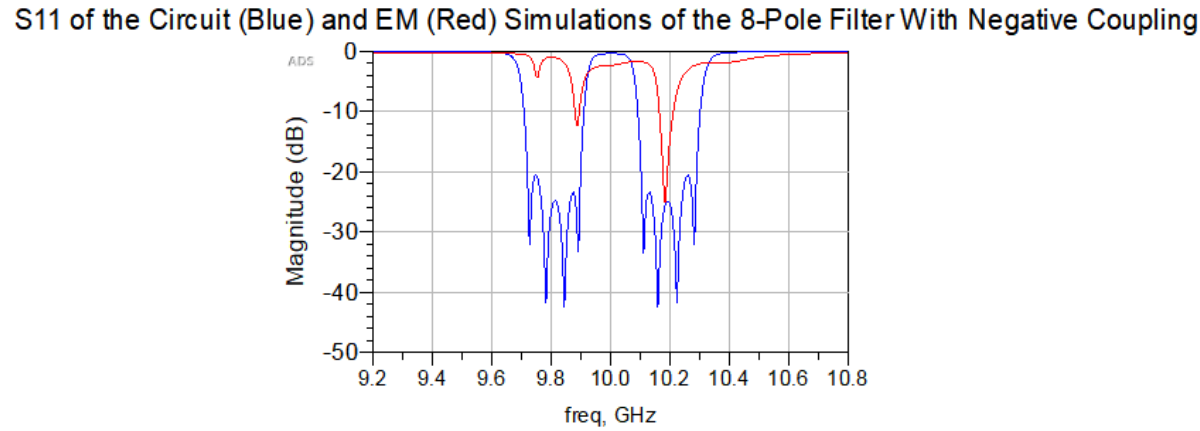


(a)

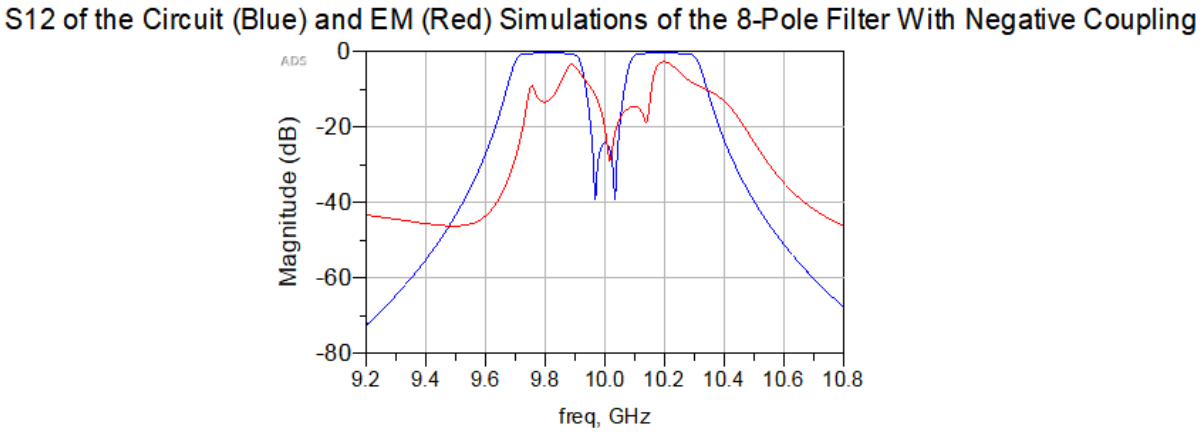


(b)

Figure 3.25: The result comparison for the circuit and EM simulations for (a) $S_{11}$ and $S_{12}$ with the negative forward coupling.

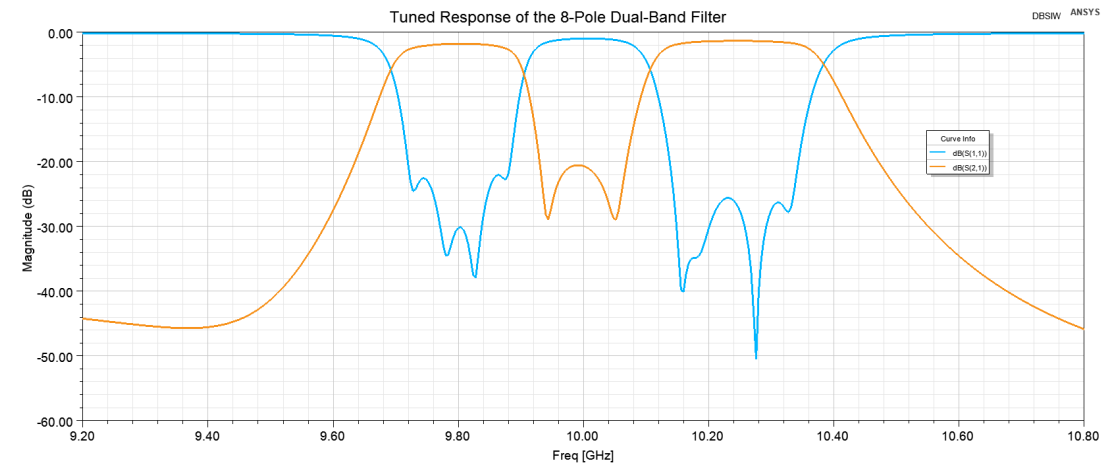


(a)

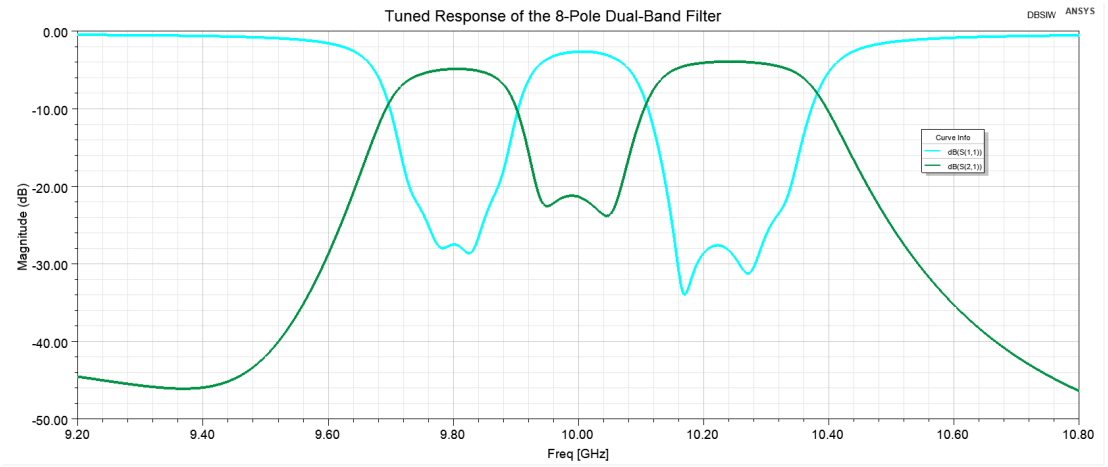


(b)

Figure 3.26: The results for the tuned EM simulations for (a) no dielectric loss and (b) with dielectric loss.

that the choice of substrate was not ideal, however, Rogers4003C was cheap and readily available at the time of the design. The final dimensions show that our initial values are

not very far off from the final values, the largest difference being 0.31mm (excluding $Iris_5$). The design was done on Rogers4003C with a dielectric constant of 3.55 and a dielectric loss of 0.0027. The final results with the dielectric loss show the lower band ranging from 9.73 GHz to 9.87 GHz (-20dB) with an insertion loss of 4.92 dB and the upper band ranging from 10.14 GHz to 10.33 GHz (-20 dB) with an insertion loss of 3.97 dB.

Table 3.12: The final tuned dimensions for the 8-Pole dual-band filter.

| $a_s$ | $L_1$ | $L_2$ | $L_3$ | $L_4$ | $Iris_1$ | $Iris_2$ |
|---|---|---|---|---|---|---|
| 12.45mm | 8.34mm | 9.36mm | 9.16mm | 10.1mm | 6.03mm | 4.53mm |
| $Iris_3$ | $Iris_4$ | $Iris_5$ | $Iris_{36}$ | $CPW_{Length}$ | $CPW_{Width}$ | $CPW_{Space}$ |
| 3.89mm | 3.79mm | 2.92mm | 4.14mm | 15.5mm | 0.2mm | 0.2mm |

### 3.4.4 Measurement Results

The measurements for the 8-pole dual-band filter were performed using a Keysight PNA with coaxial cables and SMA connectors. Referring to the note made at the beginning of this chapter, the measured and simulated results presented here are for a filter designed for a dielectric constant of 3.38. The simulated results can be seen in Figure 3.27 and the measured results with the fabricated filter in Figure 3.28.

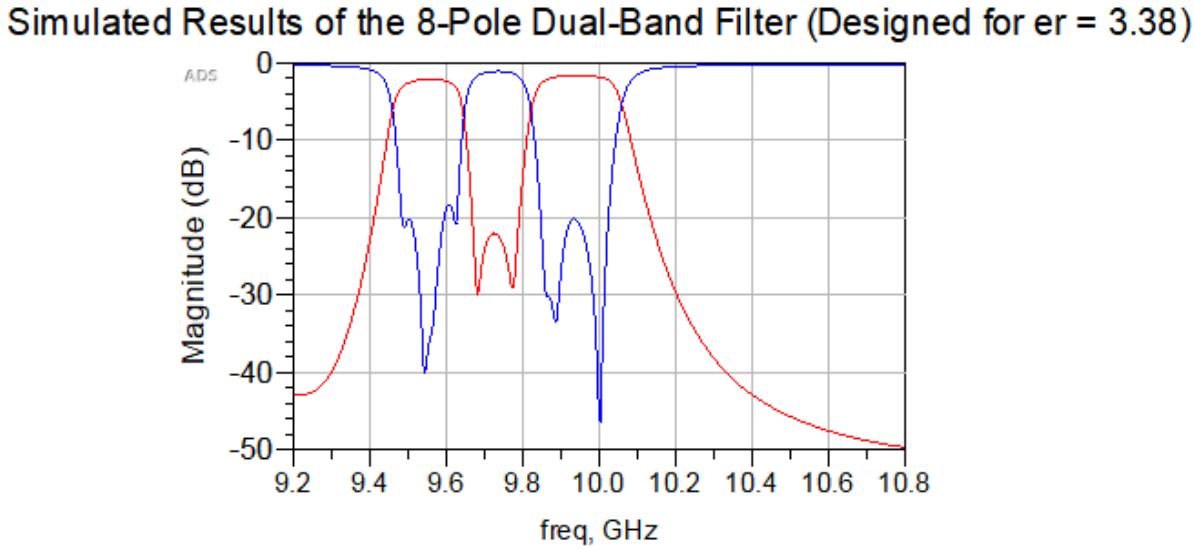


Figure 3.27: The results for the tuned EM simulations with no dielectric loss.

It can be immediately observed that there is a significant issue in $S_{12}$. There appears to be little to no transmission occurring in this filter.

To determine the issue, we first examined the experimental setup, but no issues were found. The dimensions of the filter were measured and accurately match what was sent for fabrication. Afterward, the model in HFSS was revisited to ensure that the simulation setup was correct. Again, no issues were found. The next step was to export this model to other EM simulators such as Sonnet [46], Momentum [47], and CST [48]. Figure 3.29 shows the simulated results from the three mentioned EM simulators. The results are similar enough to those of HFSS to confirm that EM simulation and setup were not the

cause of the issue. It was found that the result in $S_{12}$ could be achieved by shorting the second port to ground, however, examining the fabricated device revealed that this could not be the issue. Finally, we determined that the dielectric that the filter was fabricated on was the issue. There is a possibility that a wrong dielectric substrate with the same $\epsilon_r$ but very high loss tangent was used in the fabrication process. The more likely cause is that the batch of Rogers4003C used was defective.

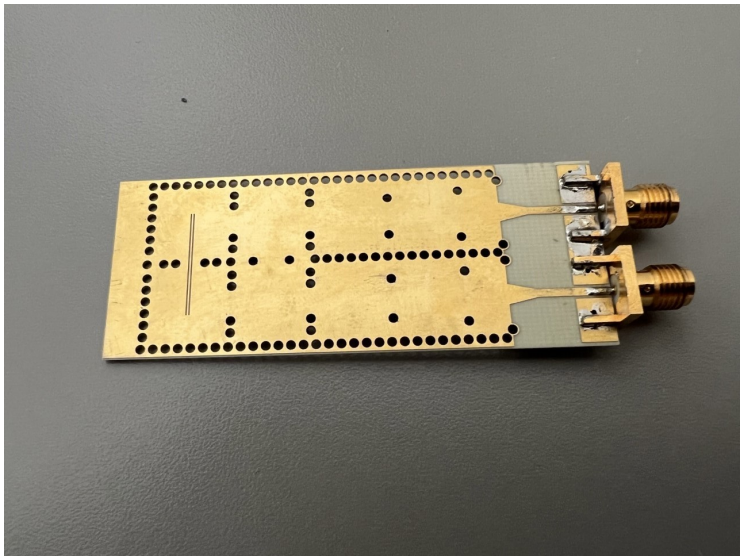

(a)

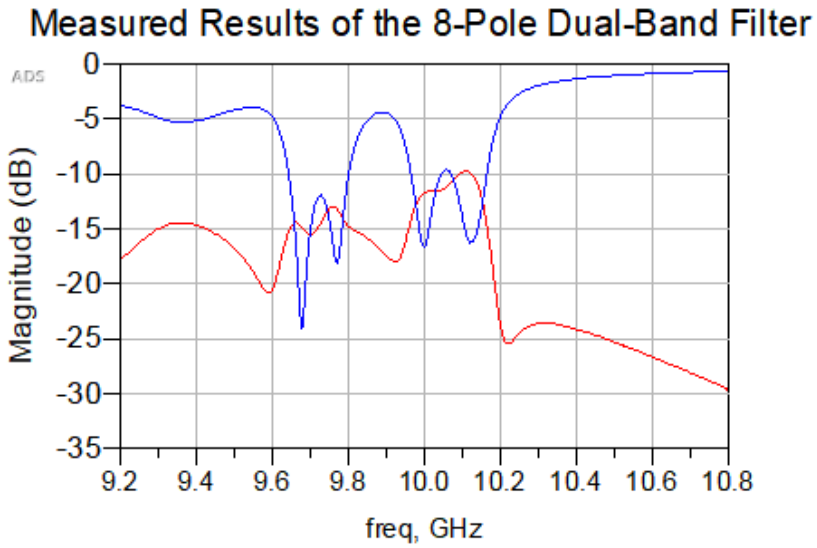


(b)

Figure 3.28: The (a) fabricated 8-pole dual-band filter and (b) the corresponding measured results.

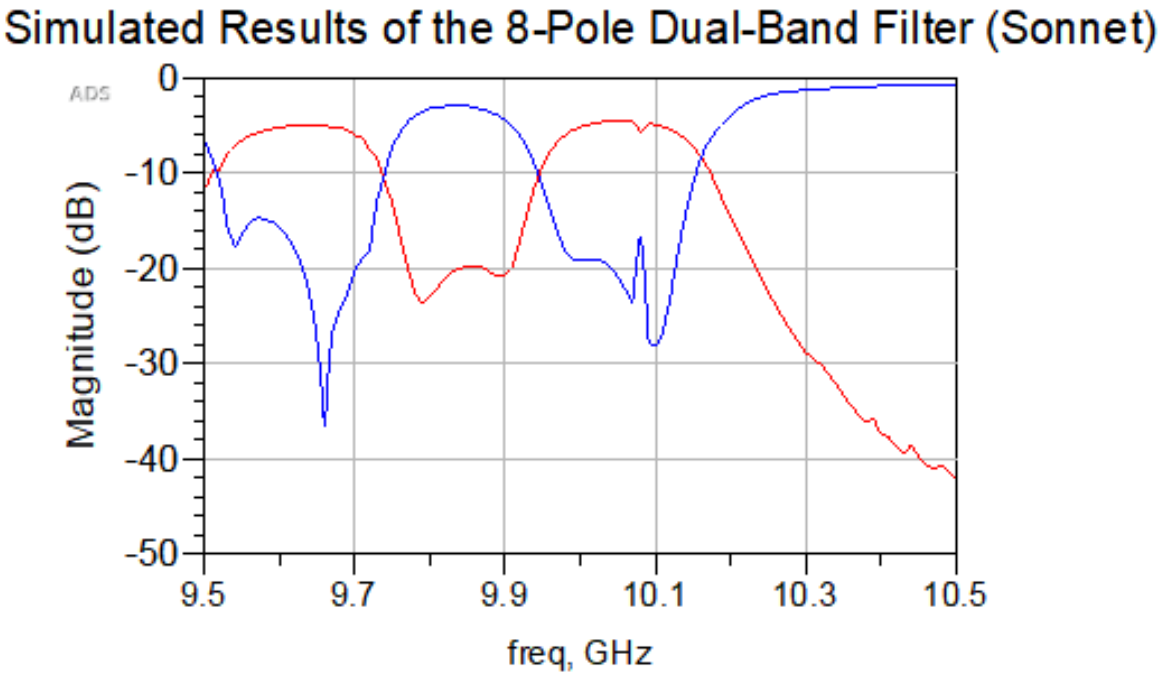
Simulated Results of the 8-Pole Dual-Band Filter (Sonnet)
ADS
Magnitude (dB)
0
-10
-20
-30
-40
-50
9.5
9.7
9.9
10.1
10.3
10.5
freq, GHz

(a)

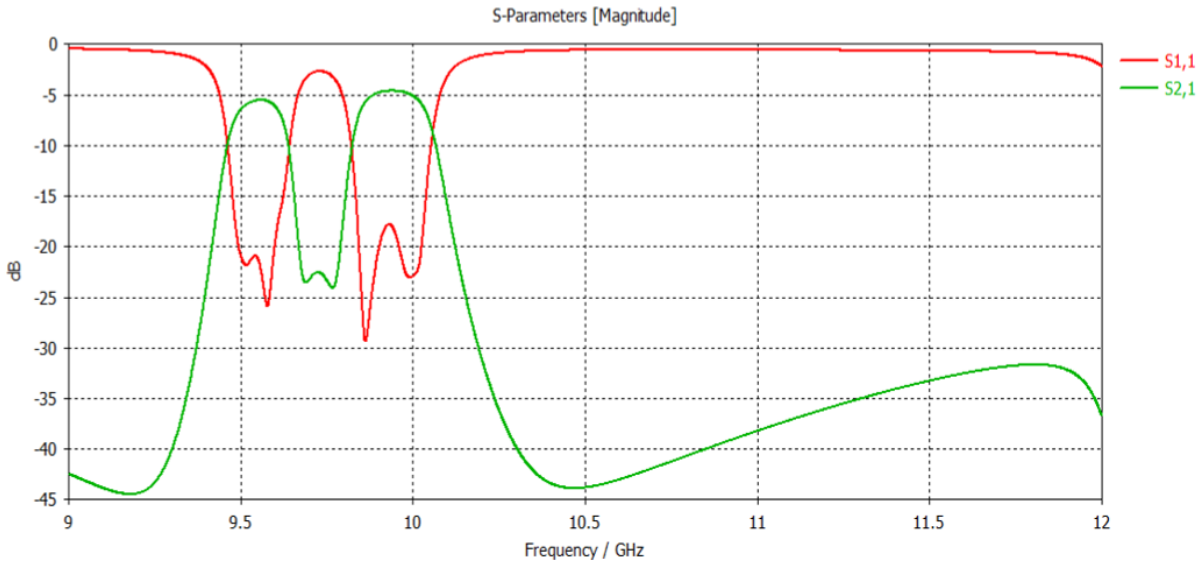
S-Parameters [Magnitude]
dB
0
-5
-10
-15
-20
-25
-30
-35
-40
-45
9
9.5
10
10.5
11
11.5
12
Frequency / GHz
S1,1
S2,1

(b)

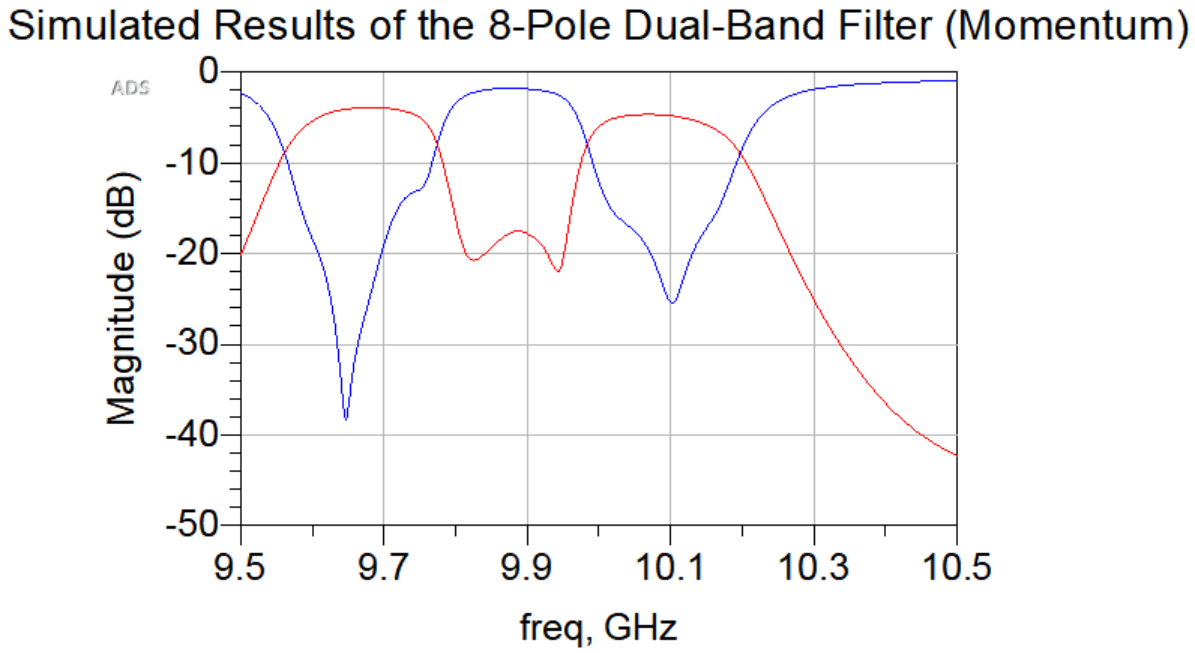


(c)

Figure 3.29: The EM simulated results of the 8-pole dual-band filter in (a) Sonnet, (b) CST, and (c) momentum.

# Chapter 4

# Superconducting Filter Design

The design of filters for kHz and MHz applications requires the use of large size resonators. Generally, at sufficiently low frequencies, lumped elements are used in the design of the filters because of the smaller footprint when compared to their distributed counterparts. However, using conventional lumped elements in such devices means that the device's footprint may surpass the fabrication limitations of certain foundries. The use of lumped elements theoretically allows for the realization of any desired bandwidth. Unfortunately, at lower frequencies, the choice of bandwidth severely affects the size of the elements, especially capacitors.

Miniaturization at such low frequencies becomes essential, even when using microstrip/CPW architectures, to reduce the overall footprint of the design and to remain within fabrica-

tion limitations. The use of multiple conducting layers can significantly reduce the size of components. Modified circuit topologies can be applied to reduce the size of certain elements, but this comes at the risk of increasing others. The use of superconducting lumped elements allows for a low loss circuit design at kHz, MHz, and GHz frequencies.

In this chapter, the realization of a classical lumped element Chebyshev filter is explored along with the application of a modified miniaturization technique to realize a low-frequency quasi-elliptic filter.

The devices in this chapter are designed with the intent to be fabricated on MIT Lincoln Laboratories 4-layer and 8-layer niobium-based processes. The use of this process allows for the design of highly miniaturized lumped elements.

The reflected group delay (RGD), as proposed in [49], is the chosen method of design and tuning. A coarse and fine model in the form of ADS and Sonnet, respectively, allow for the proper modelling of the designs.

To begin, we will first describe the MIT Lincoln Lab (MIT-LL) multilayer process. Afterward, a brief description of the lumped element filter design is given along with the reflected group delay method and the chosen methods for element miniaturization. A 3-pole 2 MHz classical Chebyshev filter is then designed, and a modified circuit topology is presented in order to further miniaturize the circuit. Using this topology, we design a 3-pole 200kHz

quasi-elliptic filter, and lastly, we explore the design of a 6-pole high-Q slotline filter using the 8-layer process.

## 4.1 MIT Lincoln Laboratory Multilayer Process

The MIT-LL process [3,4,50]is used to fabricate many types of single flux quantum (SFQ) integrated circuits using either four or eight niobium (Nb) metal layers. The stack-up of the 8-layer process is shown in Figure 4.1a [3]. The 8-layer process contains eight Nb layers (M0 - M7), with 200 nm thick silicon dioxide ($SiO_2$) layers in between them. The metal on these layers can be connected through vias (I0 - I6). An additional gold layer (M8) is used for landing pads, while the layers J5 and R5 are used for the realization of Josephson Junctions (JJ) and resistors, respectively. Figure 4.1b shows the 4-layer stack-up, the process which is used to achieve passive superconducting multi-chip modules (SMCM) [50]. As can be seen in the stack-up, this process contains four Nb metal layers (M0 - M3), one gold metal layer for pads (M4), four via layers (I0 - I3), and SiO2 layers of varying thicknesses. This stack-up does not contain JJ's, however, it does contain a resistor layer (R0) not shown in Figure 4.1b. It should be noted that the presence of the resistor layer is based on version 1.8 of the process, circa 2015.

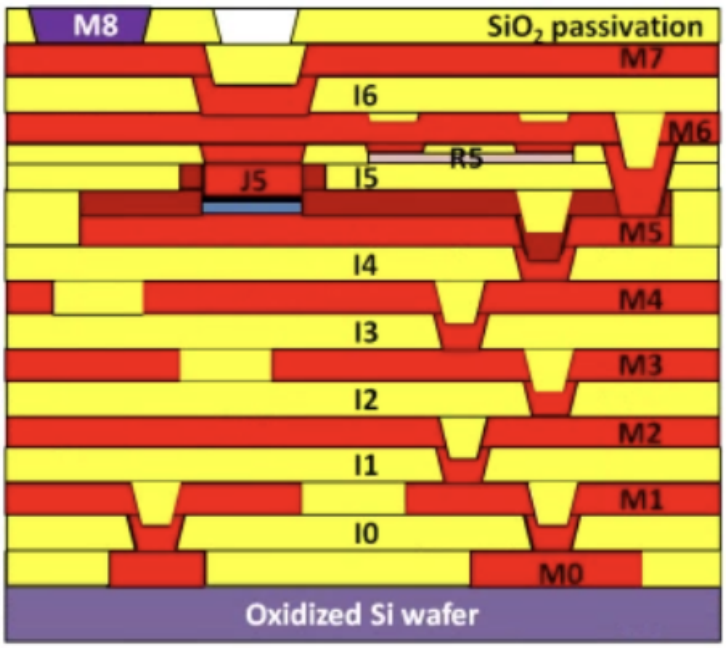


(a)

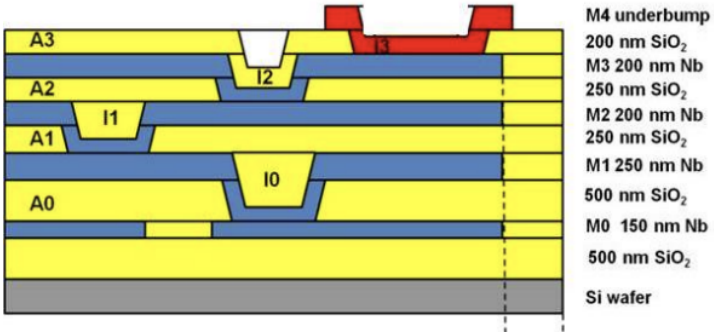


(b)

Figure 4.1: The stack-up diagram of the (a) 8-layer [3] and (b) 4-layer [50] processes from MIT-LL

## 4.2 Superconducting Lumped Element Filter Design

This section serves to provide a brief overview of the well-known methods used in the designs of the following lumped element filters. For a more in-depth explanation, it is recommended that the reader review [49], [51], and [52]

### 4.2.1 Lumped Element Filter Design

The insertion loss method for filter design is the most commonly used design technique for lumped element filters. This method allows for the determination of an ideal lumped element filter model for low-pass filters, while also providing control of a filter's center frequency and bandwidth. A frequency transform can be applied to the circuit topology to allow for the synthesis of a bandpass filter.

The low-pass g-parameters can be identified for a given return loss [51] which is assumed to be 25dB for this example. This results in a circuit that contains series and shunt resonators. An example of such a circuit for a three-pole filter in ADS can be seen in Figure 4.2. The equations for determining the capacitance and inductance can be seen below.

$$L_1 = \frac{g_1 R_0}{\omega_0 \Delta} \tag{4.1}$$

$$C_1 = \frac{\Delta}{\omega_0 g_1 R_0} \tag{4.2}$$

$$L_2 = \frac{\Delta R_0}{\omega_0 g_2} \tag{4.3}$$

$$C_2 = \frac{g_2}{\omega_0 \Delta R_0} \tag{4.4}$$

$$L_3 = \frac{g_3 R_0}{\omega_0 \Delta} \tag{4.5}$$

$$C_3 = \frac{\Delta}{\omega_0 g_3 R_0} \tag{4.6}$$

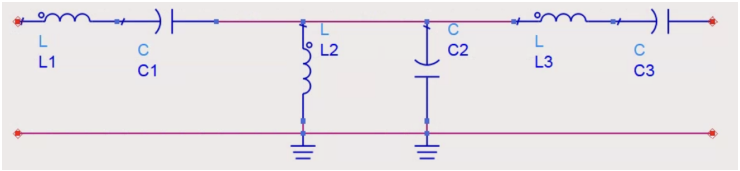


Figure 4.2: The schematic for a bandpass 3-pole lumped element filter.

### 4.2.2 Reflected Group Delay

The reflected group delay (RGD), first introduced in [49], is a powerful method for filter tuning and design. The method requires the analysis of each of the filter's resonators sequentially. This analysis requires the observation of the group delay of the input reflection coefficient. Once the resonator is properly tuned, the next resonator is included, and so on. This method can be used for the initial design of the filter, using both a coarse and fine model. By comparing the RGD of the fine model and coarse model, the parameters of

the resonator can be adjusted. Furthermore, after the filter is manufactured, this method can be used to tune the filter.

The phase information of the reflected signal is used to extract the RGD. Here $\phi$ is the phase of $S_{11}$.

$$\Gamma_{RGD} = -\frac{\delta\phi}{\delta\omega} \tag{4.7}$$

The formula for the RGD of each stage of the filter was derived by Ness; as shown in Table 4.1. The value of RGD calculated is the value seen at the center frequency. To successfully tune the filter, the resonators that appear after the current stage must be detuned.

The RGD method comes with an unfortunate caveat in that it is only applicable to narrowband filters. For narrowband filters, the RGD plot will be symmetric about the center frequency. As the bandwidth increases, the RGD becomes more asymmetric. Fortunately, by employing a circuit simulator such as ADS, the RGD of a wideband filter can be simulated and used as a reference for the EM design. When using RGD for more wideband filters, it is crucial that the whole RGD be matched.

To apply the RGD method to an EM simulation, only the resonators up to the current tuning stage are included; those that appear after can be removed. However, for certain structures, such as waveguides, the detuned cavities that appear after the current tuning

stage can be included to account for any loading effects. For example, the first tuning stage of the filter in Figure 4.2 would have only $C_1$ and $L_1$ shorted to ground as shown in Figure 4.3a. The second stage would have the first stage connected in series to the parallel combination of $L_2$ and $C_2$ which are then connected to ground as shown in Figure 4.3b. The third stage would include $C_3$ and $L_3$ to the structure in the second stage and have it shorted to ground as shown in Figure 4.3c.

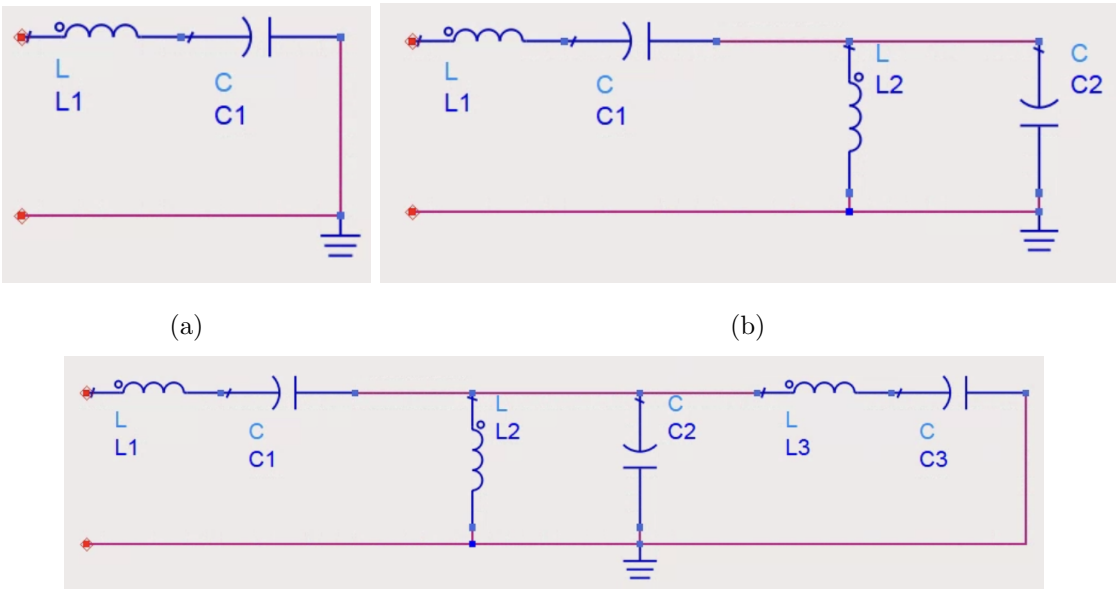


(a) (b)

(c)

Figure 4.3: The (a) first, (b) second, and (c) third stage of RGD tuning for a 3-pole lumped element filter.

Table 4.1: The formulas for the first four stages of the RGD. [49]

| Stage | Formula |
|---|---|
| 1 | $\Gamma_1(\omega_0) = \frac{4g_0g_1}{\omega_2-\omega_1}$ |
| 2 | $\Gamma_2(\omega_0) = \frac{4g_2}{g_0(\omega_2-\omega_1)}$ |
| 3 | $\Gamma_3(\omega_0) = \frac{4g_0(g_1+g_3)}{\omega_2-\omega_1}$ |
| 4 | $\Gamma_4(\omega_0) = \frac{4(g_2+g_4)}{g_0(\omega_2-\omega_1)}$ |

### 4.2.3 Miniaturization Techniques for Elements

The simplest method for minimizing lumped element circuits is to directly minimize individual elements. With access to the multilayer capabilities of MIT-LL's 4 and 8-layer processes, miniaturization techniques can be applied to the designs presented in this chapter.

The size of the capacitors can be minimized by connecting them in parallel, which will result in a smaller total area. To do so in the MIT-LL process, the metal layers (aside from the top gold layer) are used and connected in such a manner that multiple parallel capacitors are realized. Figure 4.4 shows how such capacitors can be modelled with four metal layers in Sonnet. The required structure is clearly a vertically integrated interdigital capacitor where each plate is a separate finger. If this were to be modelled using the 4-layer

Nb process, metals on layers M0 and M2 would be connected and metals on layers M1 and M3 would be connected.

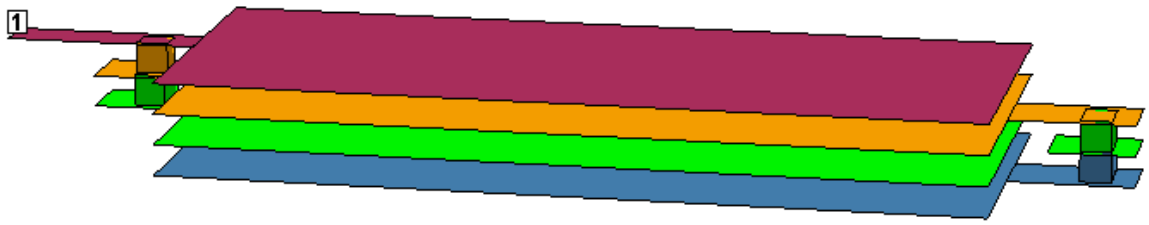


Figure 4.4: A model showing a 4-layer interdigital capacitor.

The minimization of inductors can be accomplished in a similar way to capacitors: by stacking them [52].The stacking of inductors, however, requires other considerations, the first of which is to ensure that the inductor in this case is a spiral inductor. Secondly, the signal direction within the inductor must be the same as it passes to each layer. This ensures that the magnetic fields produced by the stacked inductors are constructive, not destructive. Finally, consideration must be taken for self resonance. The inductor may exhibit capacitive behaviour if the parasitic capacitancea are large enough. Additionally, the self resonance should not be near the frequency band of interest, which can be addressed by offsetting sequential spiral inductor layers. By optimizing the offset, the self resonance frequency can be increased by as much as 39% with less than 10% [53] reduction in inductance. Unfortunately, the offset will result in a slightly larger footprint.

When completed, the stacking of inductors can theoretically increase the value of the inductance by $L * N^2$ times, where $L$ is the inductance of a single spiral and $N$ is the number of layers in which the spiral inductor appears on. Figure 4.5 shows the structure of two layers of stacked inductors.

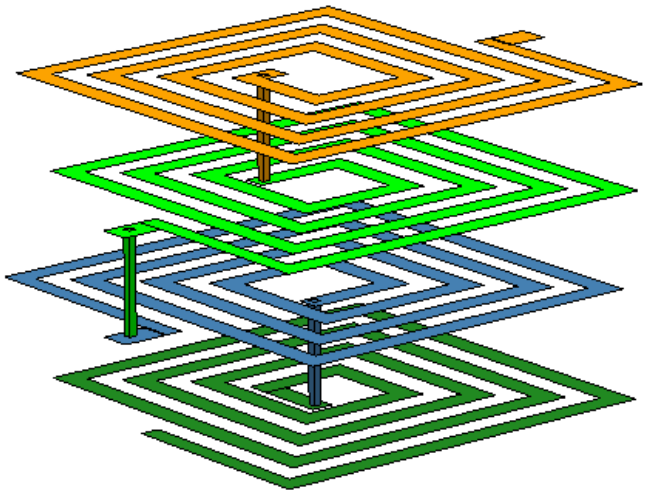

Figure 4.5: A model showing a 4-layer stacked inductor.

There are several dimensions to consider when designing spiral inductors, including the width of the inductor line $w$, the spacing between the lines $s$, the number of turns $n$, the outer diameter $d_{out}$, and the inner diameter $d_{in}$ shown in Figure 4.6. The value of the inductance can be found with the use of one of three formulas introduced by [54]. The first is the Modified Wheeler Formula (eq 4.8). Here $K_1$ and $K_2$ are coefficients that are layout dependent and can be found in Appendix B. The value of $\rho$ is defined as the fill parameter.

$$L_{Wheeler} = K_1 \mu_0 \frac{n^2 d_{avg}}{1 + K_2 \rho} \tag{4.8}$$

$$\rho = \frac{d_{out} - d_{in}}{d_{out} + d_{in}} \tag{4.9}$$

With a given $d_{avg}$, the inductor with a smaller fill parameter will have a larger inductance compared to that with a larger fill parameter.

The second formula is based on the Current Sheet Approximation (eq 4.10). Here $c_i$ are layout dependant coefficients and can be found in Appendix B. This formula is accurate as long as $\frac{s}{w} \leq 3$. It is ideal to keep $\frac{s}{w} \leq 1$ in order to maximize inductance while minimizing area.

$$L_{CS} = \frac{\mu n^2 d_{avg} c_1}{2} (ln(\frac{c_2}{\rho} + c_3 \rho + c_4 \rho^2) \tag{4.10}$$

The final formula is a Data Fitted Monomial Expression (eq 4.11). Here $\beta$ and $\alpha_i$ are layout dependant and can be found in Appendix B [54].

$$L_{ME} = \beta d_{out}^{\alpha_1} \omega^{\alpha_2} d_{avg}^{\alpha_3} n^{\alpha_4} s^{\alpha_5} \tag{4.11}$$

The value of the single-layer inductor can be found using one of the given equations and

then multiplied by $N^2$. Alternatively, there are calculators [55] for determining the value of spiral inductors, which adds convenience to the design process.

## 4.3 Design of a Lumped Element 3-Pole Chebyshev Filter

This section describes the design of a 3-pole 2 MHz filter with a fractional bandwidth of 10%, beginning with some commentary on software and simulation considerations. Next, the ideal filter model is presented, and finally, the RGD method is used and the final simulation results are shown.

### 4.3.1 EM Software Considerations

With the design of filters at such low frequencies, we found that there are issues with the use of Sonnet and HFSS. Sonnet is generally used for the design of superconducting circuits because it allows for the incorporation of kinetic inductance. Unfortunately, the simulation of low-frequency inductors provides inconsistent and unreliable results. The figures shown below highlight the drastic difference that can be seen in the simulation of the inductors based on changes in the box size in Sonnet. For capacitors, however, Sonnet still provides

accurate results at low frequencies

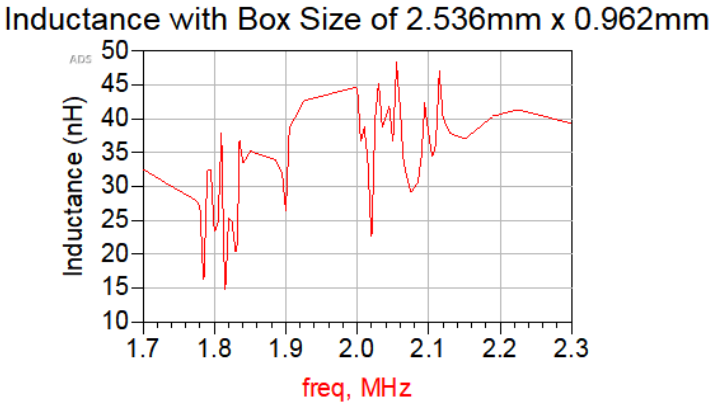


(a)

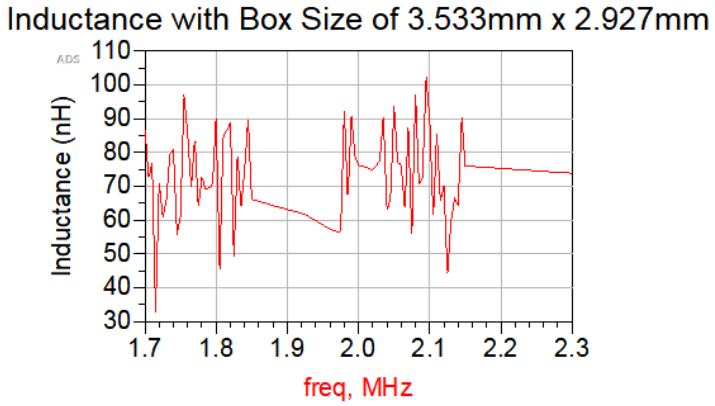


(b)

The use of HFSS with such fine dimensions and low frequencies results in extremely long simulation times. Because of this, HFSS is not an acceptable simulation tool for this design. The chosen software for this design is Momentum. This EM simulator has settings that

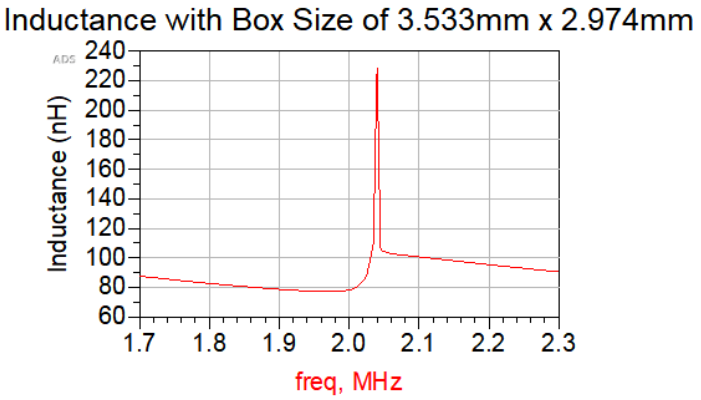


(c)

Figure 4.6: The simulation results for the same inductor with varying box sizes at 2 MHz.

allow for consistent low-frequency simulations for inductors and easy implementation of multi-layer circuits. This allows for the simulation of both individual elements and the filter as a whole. Unfortunately, kinetic inductance cannot be easily included like it is in Sonnet.

### 4.3.2 Ideal Filter Model

The first step of the design is to use the low-pass prototype g-values shown in Table 4.2 for a three-pole filter with 25 dB return loss to determine the inductance and capacitance values expressed by equations 4.1 - 4.6. Table 4.3 shows the calculated values and Figure 4.7 shows the equivalent lumped element bandpass filter while Figure 4.8 shows the simulation results from ADS.

Table 4.2: The low-pass prototype g-values for a 25 dB return loss filter.

| $g_0$ | $g_1$ | $g_2$ | $g_3$ | $g_4$ |
|---|---|---|---|---|
| 1 | 0.6708 | 1.003 | 0.6708 | 1 |

Table 4.3: The lumped element values for the 2 MHz 3-pole 10% BW filter.

| L1 | C1 | L2 | C2 | L3 | C3 |
|---|---|---|---|---|---|
| 26.69 $\mu H$ | 0.2373 nF | 396.7 nH | 15.96 nF | 26.69 $\mu H$ | 0.2373 |

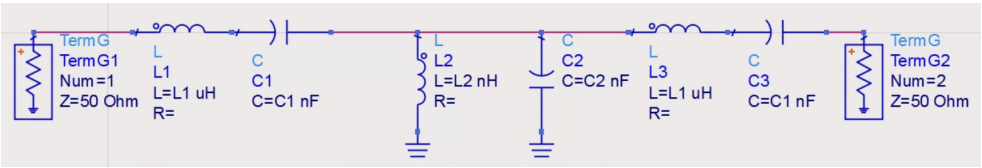


Figure 4.7: The lumped element schematic for the 2 MHz 3-pole 10% BW filter.

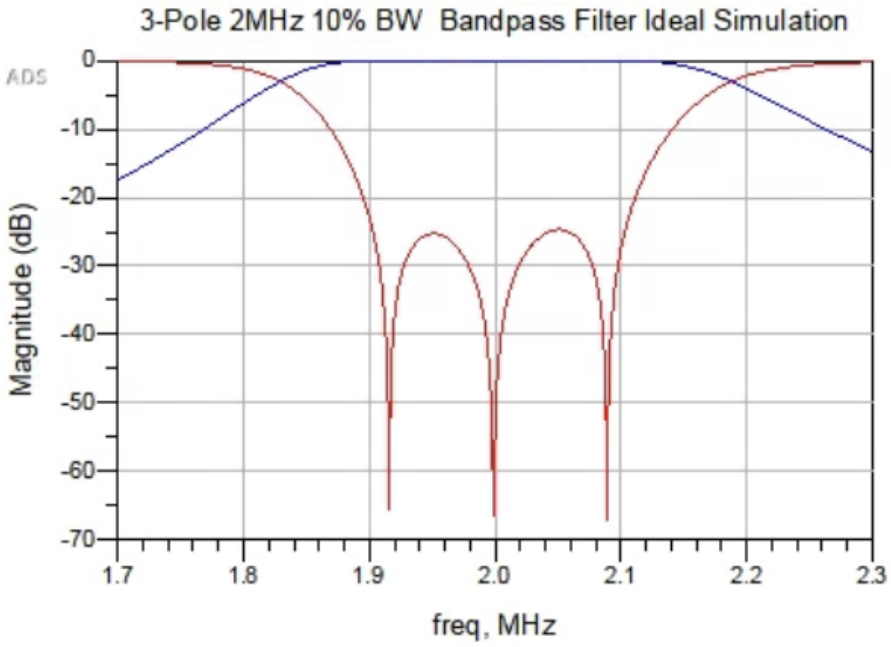


Figure 4.8: The ideal simulation results for the lumped element 2 MHz 3-pole 10% BW filter.

### 4.3.3 RGD Tuning and Simulated Results

To begin the RGD tuning, the value of the RGD must be determined for the first two stages of this design. The third stage does not require tuning due to the symmetry of the circuit, where $C_1 = C_3$ and $L_1 = L_3$. To obtain initial dimensions for the capacitance, we use equation 4.12. Here $\epsilon_0 = 8.854x10^{-12}$, $\epsilon$ is the dielectric constant of MIT-LL's substrate, A is the plate area, and $d_{eq}$ is the equivalent distance between plates for all layers used.Using these two equations, we can determine the given area for the capacitor plates based on how

many layers are used. For the inductors, [55] can be used to determine initial dimensions.

$$C_{Total} = \frac{\epsilon_0 \epsilon A}{d_{eq}} \tag{4.12}$$

$$\frac{1}{d_{eq}} = (\frac{1}{d_{A_0}} + \frac{1}{d_{A_1}} + \frac{1}{d_{A_2}}) \tag{4.13}$$

Using the equations given in Table 4.1, we find the RGD values given in Table 4.4. The results for the first two stages of the RGD tuning can be seen in Figure 4.9, and the final simulation results can be seen in Figure 4.10 along with the model of the filter. The size of the filter is 8.05mm x 10.9mm.

Table 4.4: The RGD for the first two stages of the 2 MHz 3-pole 10% BW filter.

| Stage | RGD ($\mu s$) |
|---|---|
| 1 | 2.134 |
| 2 | 3.193 |

As is illustrated in Figure 4.10, the results of the testing indicate that the filter requires slight tuning. Here, the second capacitor size was increased slightly to bring the response to that in Figure 4.11.

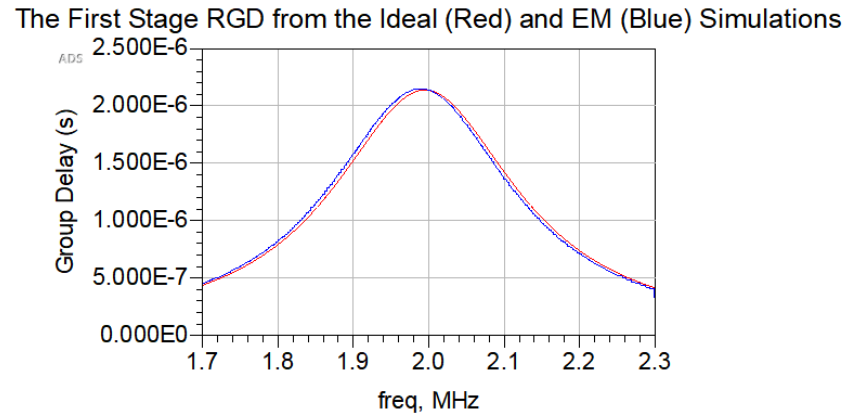


(a)

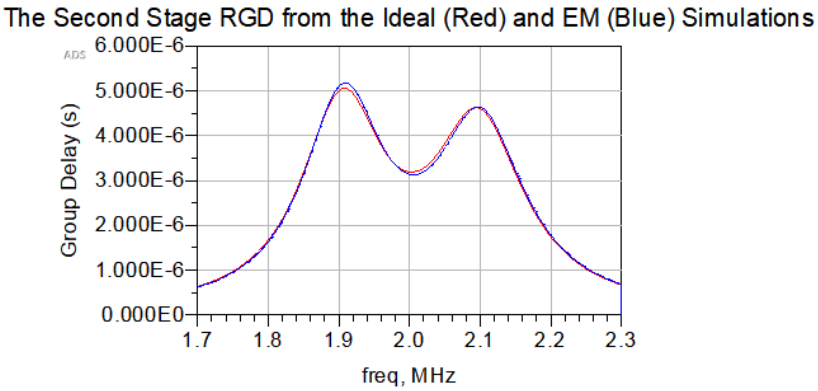


(b)

Figure 4.9: The (a) first and (b) second RGD stage results for the EM tuned 3-Pole 2MHz filter.

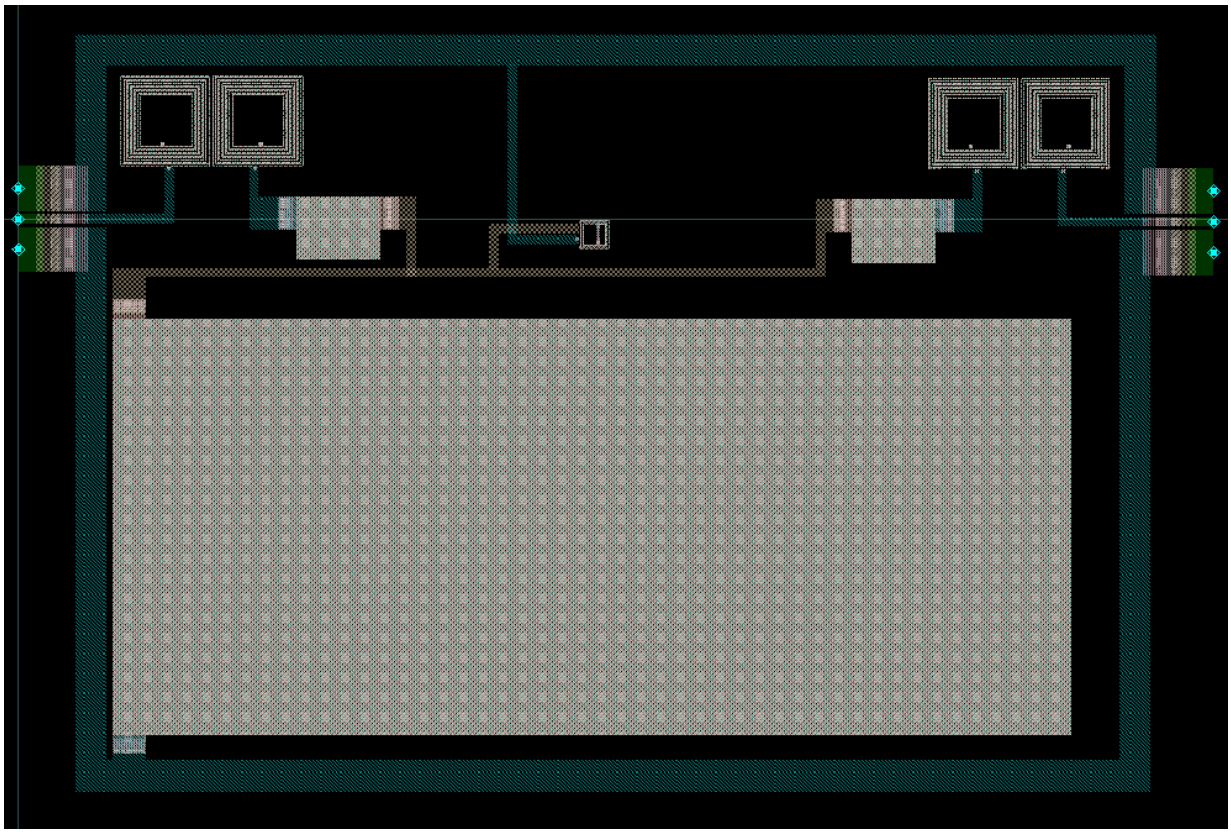

(a)

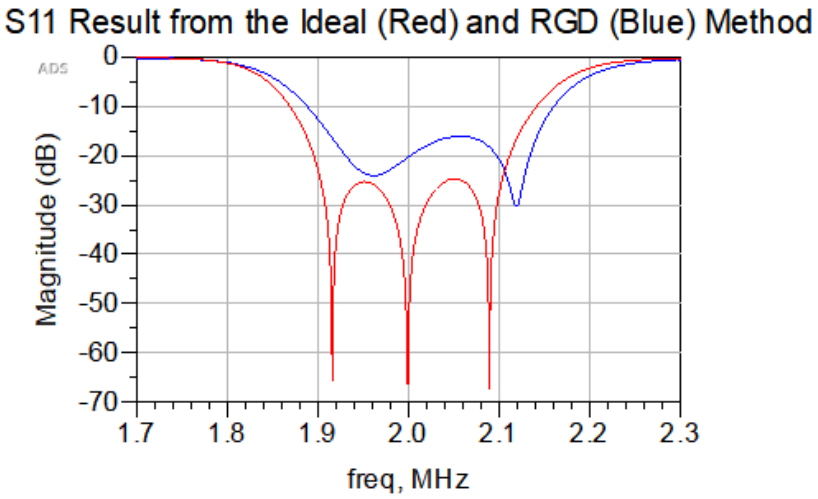


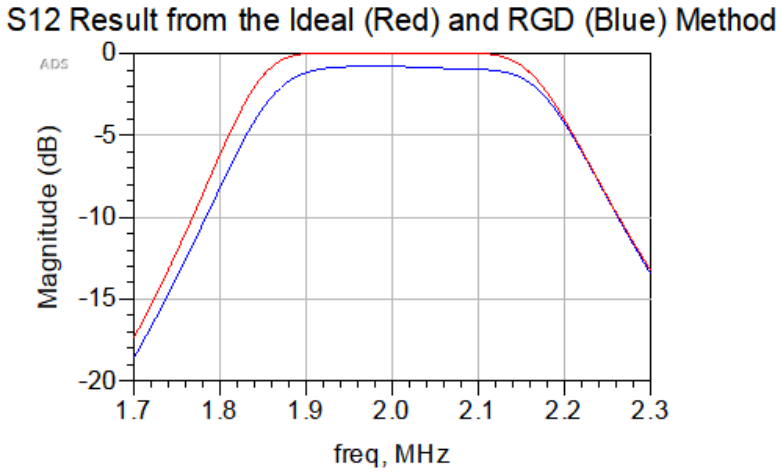


(b)

Figure 4.10: The (a) model of the 3-pole Chebychev filter and the (b) full model EM results from the RGD method.

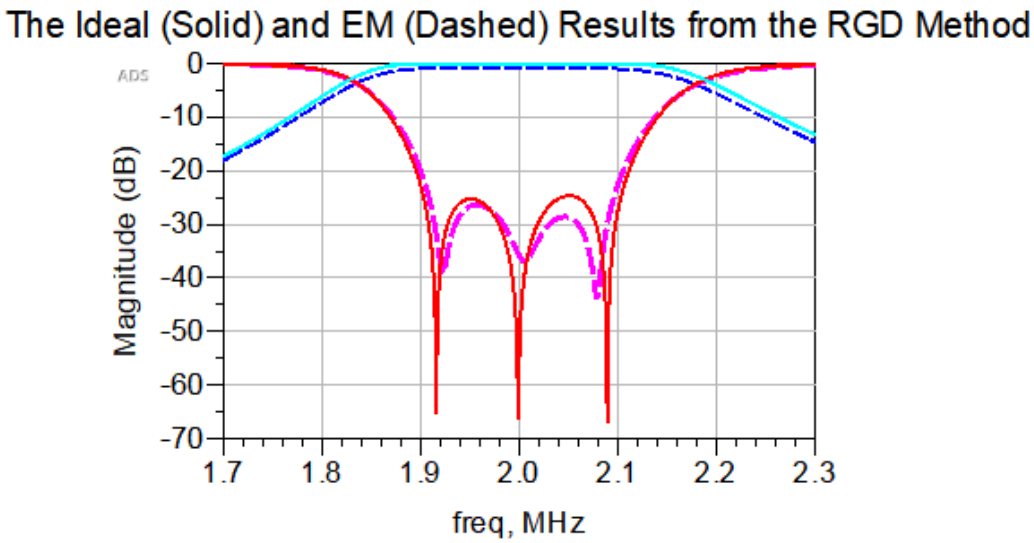


Figure 4.11: The final tuned results for the 3-pole 2MHz Chebyshev filter.

## 4.4 Design of a Miniaturized Lumped Element 3-Pole 200kHz Filter

### 4.4.1 Miniaturization of Lumped Element Filters by Using Additional Elements

Since MIT-LL has stringent spatial requirements, the designed circuits should be as small as possible. The use of stacked inductors and vertically integrated interdigital capacitors only provide so much by way of size reduction, and it is sometimes insufficient. The circuit topology is another area in which miniaturization can be carried out. [56] and [57] provide a method to miniaturize lumped element circuits in narrowband filters by adding additional elements to the resonators. The goal of adding these elements is to reduce the value of large elements, primarily capacitors. In lower frequency lumped element filters, the capacitor size heavily influences the total footprint of the circuit.

This method is first used to explore what the expected size of the 200 kHz 3-pole filter will be in comparison to a traditional series-shunt topology. First, we design a circuit model for a Chebyshev filter with 10% bandwidth at 200 kHz. The circuit model and simulation results can be seen in Figure 4.12, and the values can be seen in Table 4.5.

We now use the methods shown in [56] and [57] and apply the equations to the additional

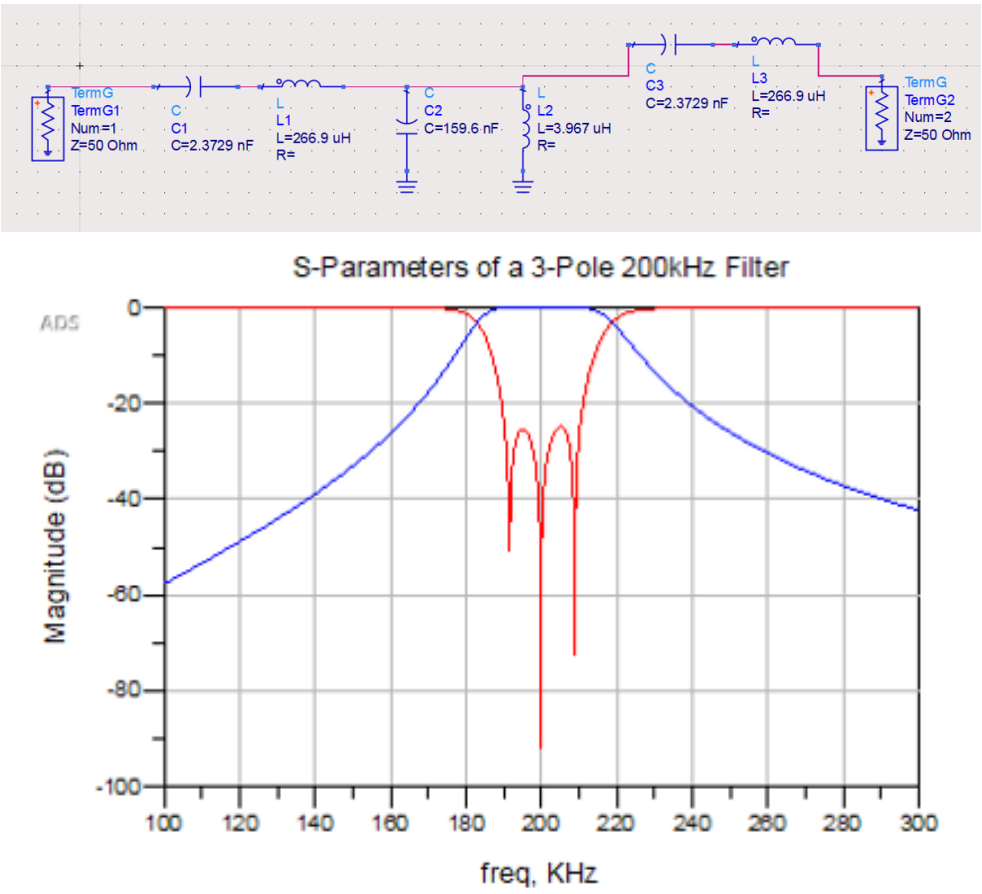


Figure 4.12: The circuit model and results for the 200kHz Chebyshev filter.

Table 4.5: The lumped element values for the 200kHz Chebyshev Filter..

| $C_1(nF)$ | $L_1(\mu H)$ | $C_2(nF)$ | $L_2(\mu H)$ | $C_3(nF)$ | $L_3(\mu H)$ |
|---|---|---|---|---|---|
| 2.3729 | 266.9 | 159.6 | 3.967 | 2.3729 | 266.9 |

elements and resonators. The first set of equations is for parallel resonators. An inductor $L_s$ is added in series with the capacitor $C$ and parallel to $L_p$. The parameter $a$, is a multiplication value to help visualize the change in size of the elements. $L$ in the equations refers to the original value of the parallel inductor in the Chebyshev filter.

$$L_s = a * L(1 - \frac{1}{\sqrt{a}}) \tag{4.14}$$

$$L_p = \sqrt{a} * L \tag{4.15}$$

The second set of equations is for series resonators. A capacitor $C_p$ is added in parallel with the inductor $L$. $C$ in equation 4.16 refers to the original value of the series capacitor in the Chebyshev filter. The circuit model of this filter can be seen in Figure 4.13.

$$C_p = a * C(1 - \frac{1}{\sqrt{a}}) \tag{4.16}$$

$$C_s = \sqrt{a} * C \tag{4.17}$$

By varying the value of $a$, we can control the position of an upper band transmission zero and effectively the asymmetry of the in-band response. Figure 4.14 shows the effect on the S-parameters when varying $a$ from 1 to 30.

We can see that an increase in a will bring a transmission zero closer to the passband of the filter, but it will also increase the asymmetry of the in-band response. This is characterized

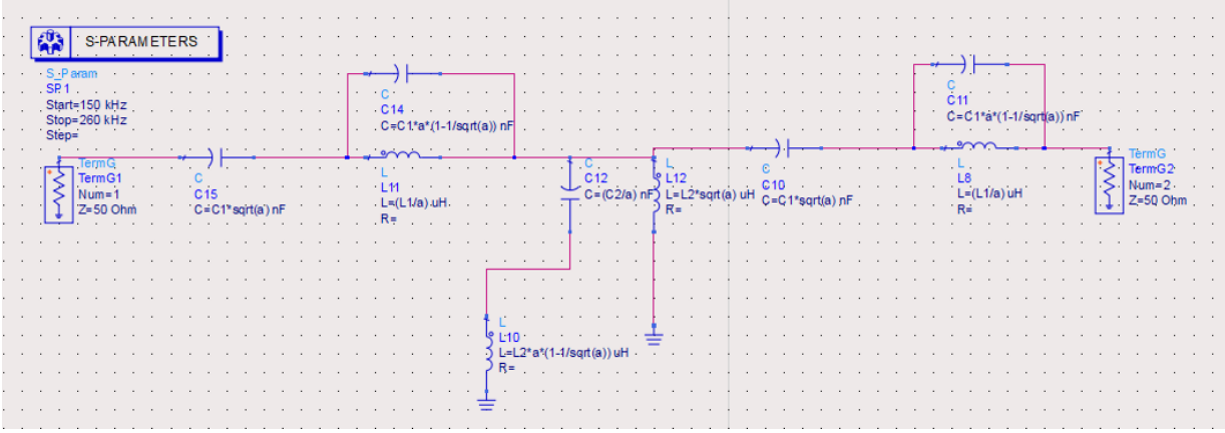


Figure 4.13: The circuit model and when applying equations 4.14 - 4.17.

by the steeper rejection on the upper band and the worsening rejection on the lower band. For the transmission zero to be placed appropriately near the passband, a large value of $a$ is required. This introduces a problem in which we will reduce the size of several components, but those will be somewhat offset by the size increase of others. As a result, we cannot maximize the miniaturization. Figure 4.15 shows the response if we use an $a$ of 40 and Table 4.6 shows the corresponding element values.

Table 4.6: The lumped element values for the 200kHz Filter when $a = 40$.

| $C_1(nF)$ | $L_1(\mu H)$ | $C_{p1}(nF)$ | $C_2(nF)$ | $L_2(\mu H)$ | $L_s(\mu H)$ | $C_3(nF)$ | $L_3(\mu H)$ | $C_{p3}(nF)$ |
|---|---|---|---|---|---|---|---|---|
| 15 | 6.6725 | 79.9 | 3.99 | 25.09 | 133.6 | 15 | 6.6725 | 79.9 |

As illustrated in Table 4.6, we now have two 15nF capacitors and two 79.9nF capacitors

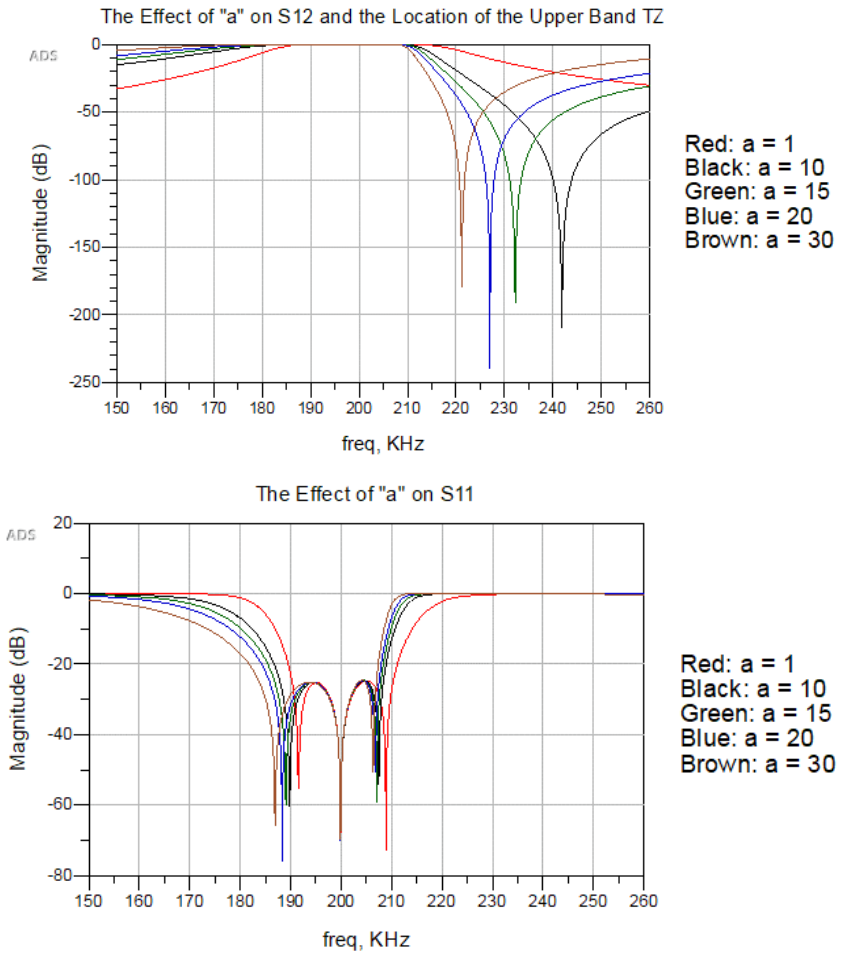


Figure 4.14: The effect of $a$ on $S_{11}$ and $S12$.

that will offset the size reduction of the 159.6nF capacitor. Therefore, for this application, the use of equations 4.14-4.17 will not benefit much in size reduction.

The RGD technique is now implemented to obtain an improved response. This means that we do not utilize a scaling value of a, but rather tune to help reduce element size. Figure

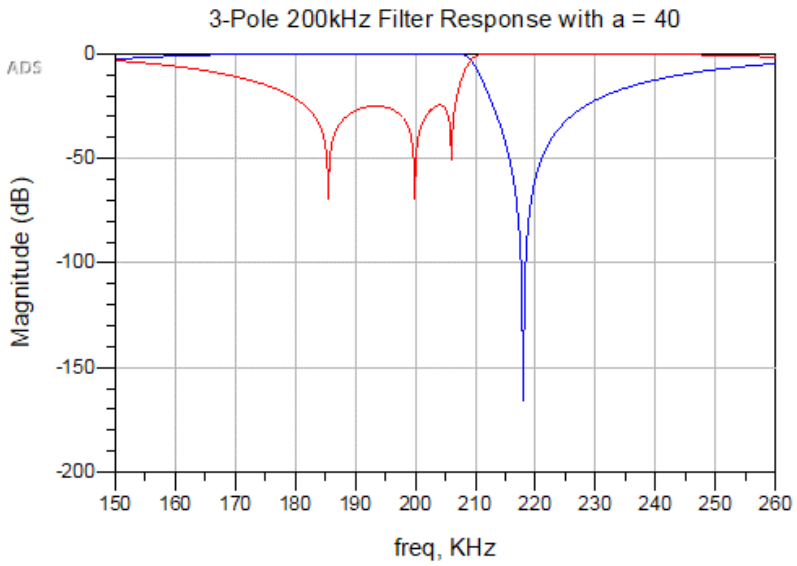


Figure 4.15: The 200kHz filter response when $a = 40$.

4.16 shows the tuned response using RGD, and Table 4.7 shows the element values. We see here a drastic reduction in the size of the capacitors in the circuit, but an increase in the size of some of the inductors. However, the footprint reduction of the capacitors heavily outweighs the increase in footprint from the inductors.

Table 4.7: The lumped element values for the 200kHz Filter when using the RGD technique.

| $C_1(nF)$ | $L_1(\mu H)$ | $C_{p1}(nF)$ | $C_2(nF)$ | $L_2(\mu H)$ | $L_s(\mu H)$ | $C_3(nF)$ | $L_3(\mu H)$ | $C_{p3}(nF)$ |
|---|---|---|---|---|---|---|---|---|
| 4.572 | 72.9 | 4 | 8.91 | 16.633 | 53 | 4.572 | 72.9 | 4 |

We now look to improve the response in 4.16 by introducing a transmission zero in the

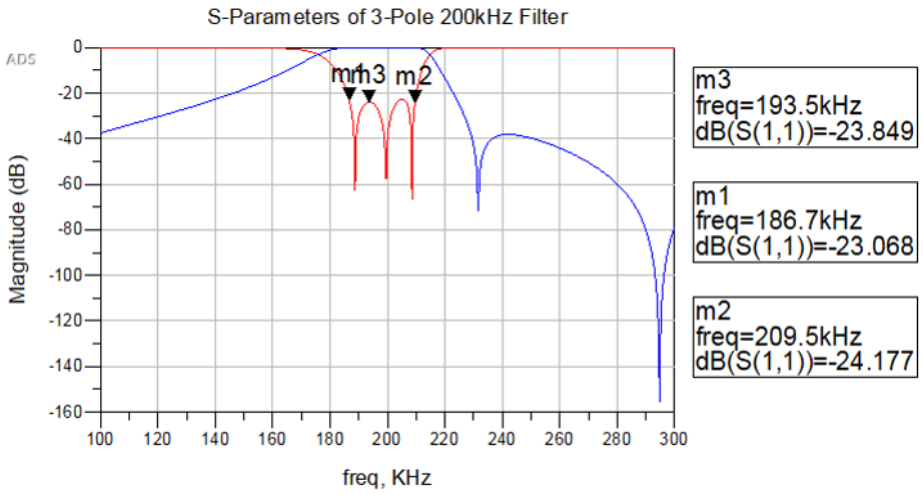


Figure 4.16: The S-parameters of the RGD tuned miniaturized circuit when not using equations 4.14 - 4.17.

lower band. To do so, we introduce an inductor connected between the input of resonator one and the junction between resonators two and three as shown in Figure 4.17. Here $C_p$ has been changed to $C_m$ and $L_s$ to $L_m$.

By adding the inductor and tuning the elements, we obtain the results in Figure 4.18. The corresponding element values can be seen in Table 4.8. The results are compared with the $S_{12}$ of the Chebyshev equivalent. It is observed that for the TZ to be beneficial, $L_c$ has to be sufficiently small. Unfortunately, this alters the in-band result and appears to eliminate one of the reflection zeros.

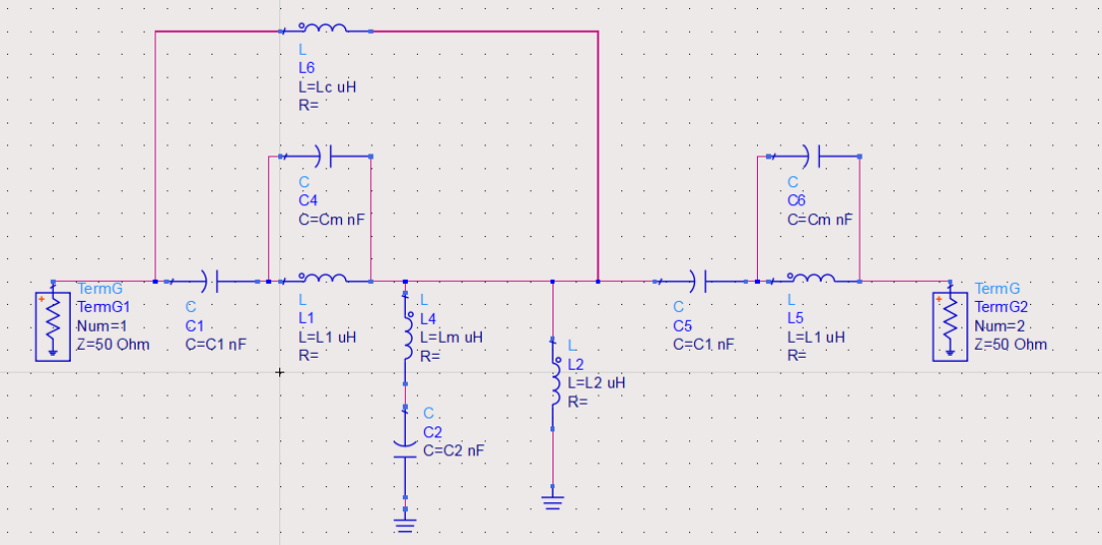


Figure 4.17: The miniaturized circuit model with cross coupling.

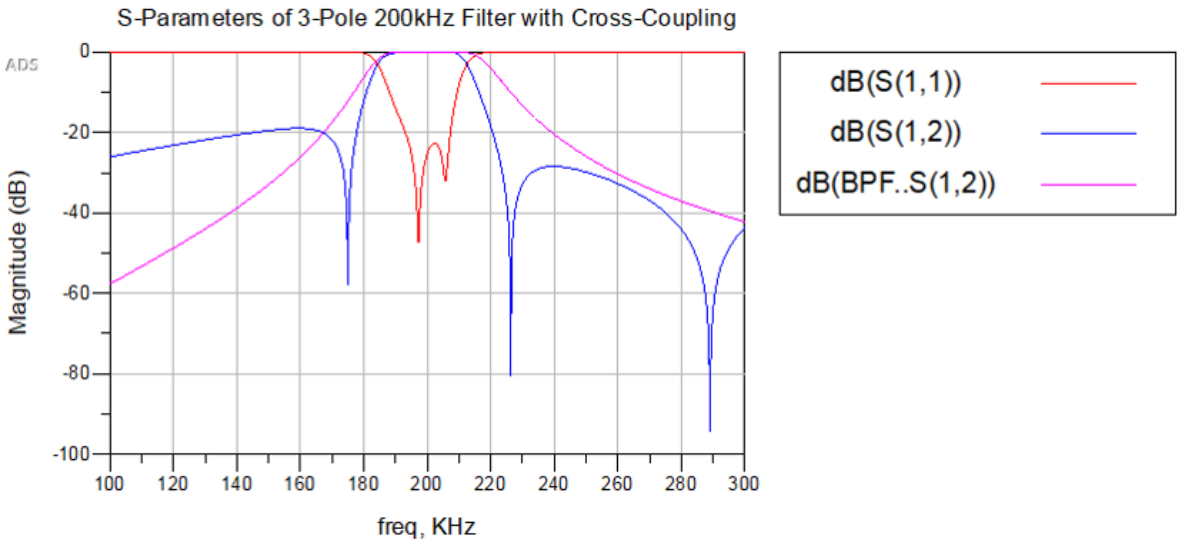


Figure 4.18: The results of the miniaturized circuit model with cross coupling.

Table 4.8: The lumped element values for the 200kHz Filter when including the cross-coupling.

| $C_1(nF)$ | $L_1(\mu H)$ | $C_{m1}(nF)$ | $C_2(nF)$ | $L_2(\mu H)$ | $L_m(\mu H)$ | $C_3(nF)$ | $L_3(\mu H)$ | $L_c(\mu H)$ | $C_{m3}(nF)$ |
|---|---|---|---|---|---|---|---|---|---|
| 4.572 | 72.2 | 4.2 | 7.85 | 16.853 | 63 | 4.572 | 72.2 | 66.86 | 4.2 |

We then take the elements from Tables 4.8, 4.7, and 4.5 and compare their sizes. Using equation 4.12 and the four-layer stack-up for the capacitors, and [55] for square inductors, the approximate sizes of these elements are obtained and shown in Table 4.9.

Table 4.9: The lumped element sizes for the 200kHz Chebychev filter with and without the cross-coupling.

| | Table 4.8 | Table 4.5 | Table 4.7 |
|---|---|---|---|
| $C_1/C_3(mm)$ | 2 * (3.35 x 3.35) | 2 * (2.414 x 2.414) | 2 * (3.35 x 3.35) |
| $L_1/L_3(mm)$ | 2 * (2.45 x 2.45) | 2 * (4 x 4) | 2 * (2.47 x 2.47) |
| $C_2(mm)$ | 4.39 x 4.39 | 19.8 x 19.8 | 4.6 x 4.6 |
| $L_2(mm)$ | 1.5 x 1.5 | 0.925 x 0.925 | 0.92 x 0.92 |
| $C_m/C_p(mm)$ | 2 * (3.211 x 3.211) | — | 2 * (3.13 x 3.13) |
| $L_m/L_s$ | 2.33 x 2.33 | — | 2.21 x 2.21 |
| $L_c(mm)$ | 2.35 x 2.35 | — | — |
| Total ($cm^2$) | 8.18 | 11.21 | 6.56 |

There is a size reduction of 27% in comparison to the classic Chebyshev topology and the topology in Figure 4.17. When comparing the topology in Figure 4.17 and the circuit topology given in Figure 4.13 when the RGD is used to tune the values, there is a size reduction of 19.8%, however, the response of the filter is not ideal. The RGD technique will not reduce the size of the circuit, this is achieved by paying close attention to the values of the elements as we perform the tuning. It appears that the addition of the cross-coupling only improves the near-band response of the filter at the expense of the in-band response and a slight footprint increase. In the next section, we look at a topology where the footprint of the 3-pole filter is reduced even further. The IL on the simulated filter is 0.79dB.

### 4.4.2 Further Miniaturization Using Modified Circuit Topology

The information summarized in Table 4.9 provides us with insight as to what the largest contributing factors are to the overall size of the circuit. We see that $C_2$ in the classic Chebyshev circuit is the largest element present in all three topologies, but it can easily be reduced by the inclusion of $L_m/L_s$. However, the reduction of $L_1/L_3$ by the inclusion of $C_m/C_p$ is minimal and introduces two extra capacitors that not only offset the reduction, but actually increase the overall footprint. Therefore, a topology is presented that focuses on the reduction of only $C_2$ and still includes transmission zeros to help with the out-of-band rejection.

This topology can be seen as a middle ground between those presented in Figure 4.13 and Figure 4.17. Here, $C_m/C_p$ is completely removed but $L_m/L_s$ remains, and instead of cross-coupling from an inductor, a capacitor is connected from input to output. The circuit topology can be seen in Figure 4.19. Here, $L_m$ can be seen in the shunt branch, and $C_c$ is included for the cross-coupling. The circuit model is designed using the RGD technique, and the results can be seen in Figure 4.20, with the element values presented in Table 4.10.

In the circuit model, there are now two upper-band transmission zeros and one on the lower band. These circuit simulator results are compared to the results of the Chebyshev filter in Figure 4.21. The upper-band result is improved drastically with this topology, but

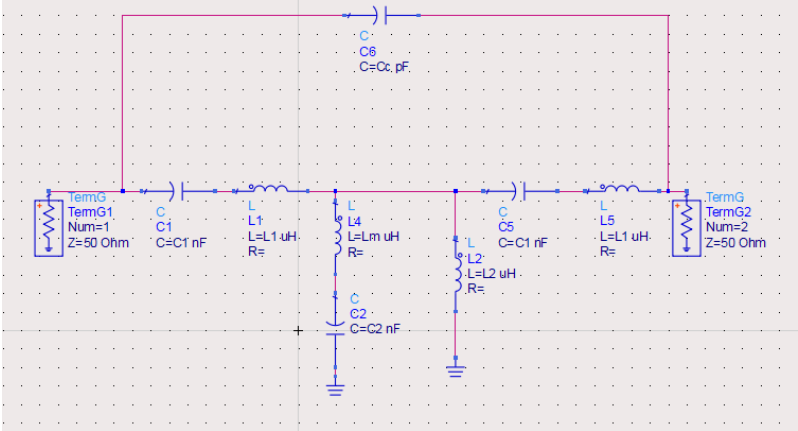


Figure 4.19: The topology for the miniaturized 200kHz filter design.

Table 4.10: The lumped element values for the miniaturized 200kHz filter.

| $C_1(nF)$ | $L_1(\mu H)$ | $C_2(nF)$ | $L_2(\mu H)$ | $L_m(\mu H)$ | $C_3(nF)$ | $L_3(\mu H)$ | $C_c(nF)$ |
|---|---|---|---|---|---|---|---|
| 2.3732 | 257.8 | 7.77 | 16.645 | 61.454 | 2.3732 | 257.8 | 0.241 |

the lower-band response is slightly worse. Normally, $C_c$ could be increased to bring the transmission zero closer to the passband and improve the result, but Figure 4.22 shows that as $C_c$ increases, degradation in the upper band occurs and the improvement of the upper-band essentially disappears. It is interesting to observe the effect that $C_c$ has on the transmission zeros. We decided to accept the decline in lower-band rejection performance for the improved upper-band rejection performance.

The element values can now be taken and added to Table 4.9 in order to compare this

example to the other circuit topologies. The update is shown in Table 4.11.

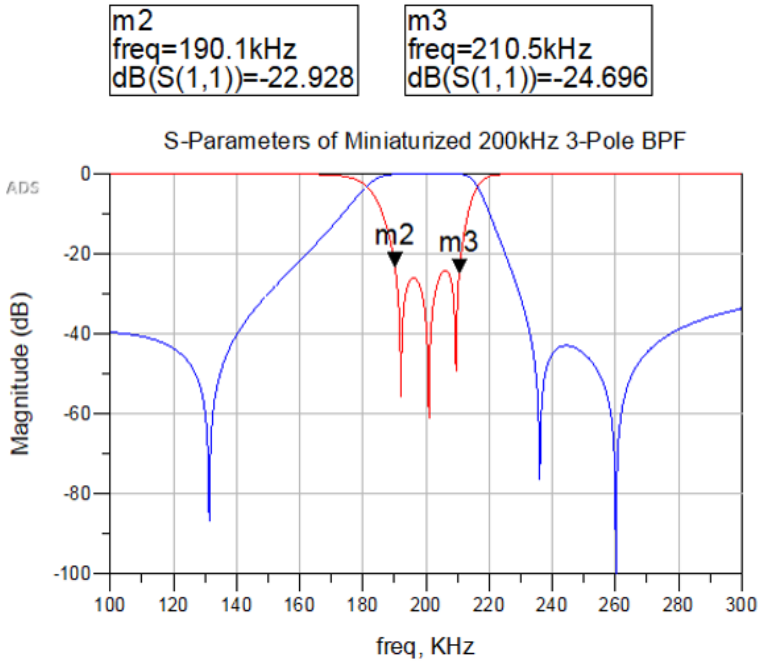


Figure 4.20: The circuit simulation results for the miniaturized 200kHz filter.

This comparison clearly shows that the presented topology provides the smallest footprint. It is 58% smaller than the Chebyshev filter, and 42% smaller than the filter in Table 4.8. This topology is 28% smaller than the next smallest topology.

### 4.4.3 Simulated Results

The values in Table 4.10 are taken and used to model this circuit in an EM simulator. Similar to the filter presented in 4.3, Momentum must be used due to various software

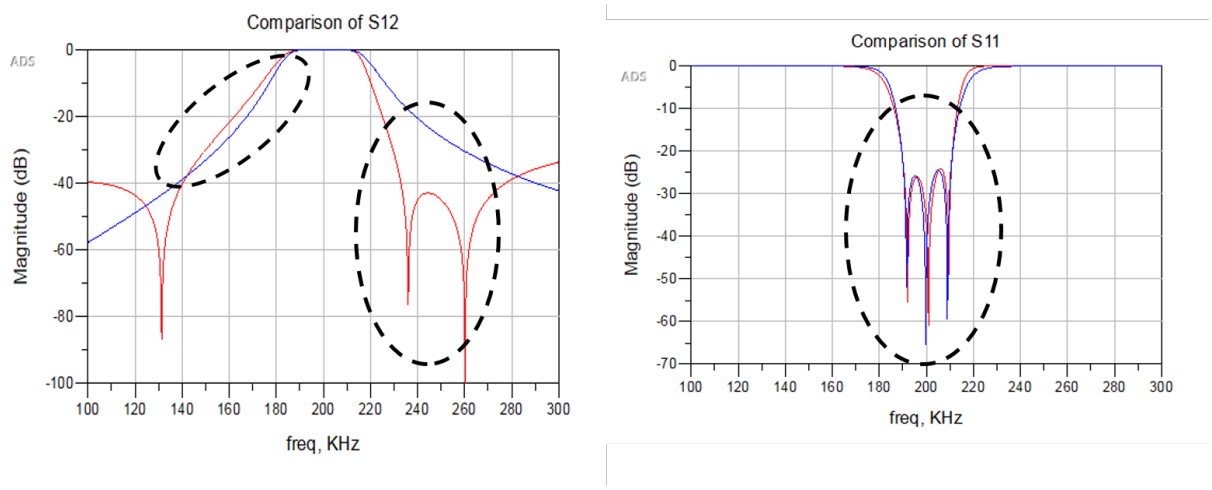


Figure 4.21: The circuit simulation results for the miniaturized 200kHz filter (red) compared to the results from the Chebychev filter (blue).

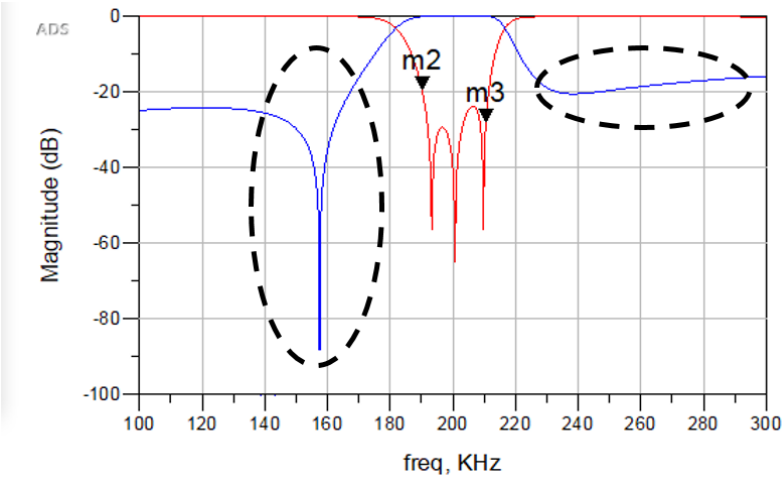


Figure 4.22: The circuit simulation results for the miniaturized 200kHz filter when $C_c = 1$nF.

issues present in Sonnet and HFSS. One consideration made in this design is whether or not $L_1$ should be split into smaller series inductors. This decision must be made because

Table 4.11: A summary of the element sizes of the various circuit topologies presented.

| | Table 4.8 | Table 4.5 | Table 4.7 | Table 4.10 |
|---|---|---|---|---|
| $C_1/C_3(mm)$ | 2 * (3.35 x 3.35) | 2 * (2.414 x 2.414) | 2 * (3.35 x 3.35) | 2 * (2.414 x 2.414) |
| $L_1/L_3(mm)$ | 2 * (2.45 x 2.45) | 2 * (4 x 4) | 2 * (2.47 x 2.47) | 2 * (4 x 4) |
| $C_2(mm)$ | 4.39 x 4.39 | 19.8 x 19.8 | 4.6 x 4.6 | 4.37 x 4.37 |
| $L_2(mm)$ | 1.5 x 1.5 | 0.925 x 0.925 | 0.92 x 0.92 | 1.5 x 1.5 |
| $C_m/C_p(mm)$ | 2 * (3.211 x 3.211) | — | 2 * (3.13 x 3.13) | — |
| $L_m/L_s$ | 2.33 x 2.33 | — | 2.21 x 2.21 | 2.33 x 2.33 |
| $L_c(mm)$ | 2.35 x 2.35 | — | — | — |
| $C_c(mm)$ | — | — | — | 0.77 x 0.77 |
| Total ($cm^2$) | 8.18 | 11.21 | 6.56 | 4.75 |

the self resonance of the inductor is nearing the passband as seen in Figure 4.23. There is a trade-off to splitting the inductor into two. The benefit is that the self resonance is pushed to a higher frequency, but the drawback is that the simulation time for the whole circuit becomes prohibitively long. We want to be able to analyze the filter with a full EM model as opposed to a semi-EM model, so we choose to leave the inductor as a whole.

The EM model and results can be seen in Figure 4.24. The overall size of the filter is 26mm x 15.25mm, for a total area of $3.96cm^2$—even smaller than predicted. The EM

and circuit simulation results match almost perfectly, except for some discrepancy in the upper rejection band. The steep fall-off in the upper band indicates that the transmission zeros that should be present do, in fact, show in the EM results. The IL of the filter was simulated to be 0.03 dB with the highest value of RL being 21.86 dB.

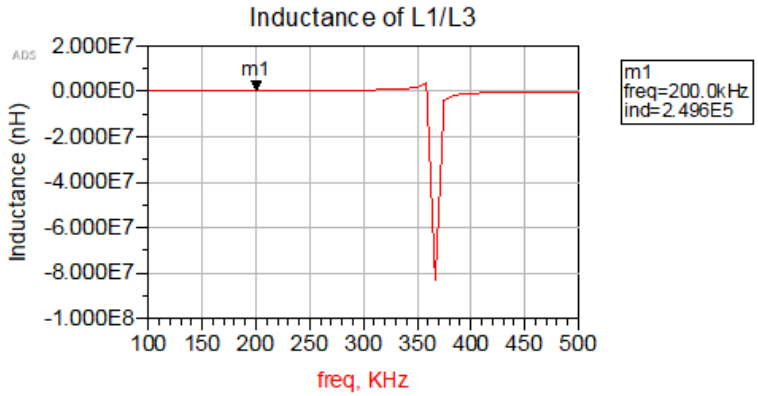


Figure 4.23: The indcutor EM simulation results showing the self resonance of $L_1$ and $L_3$.

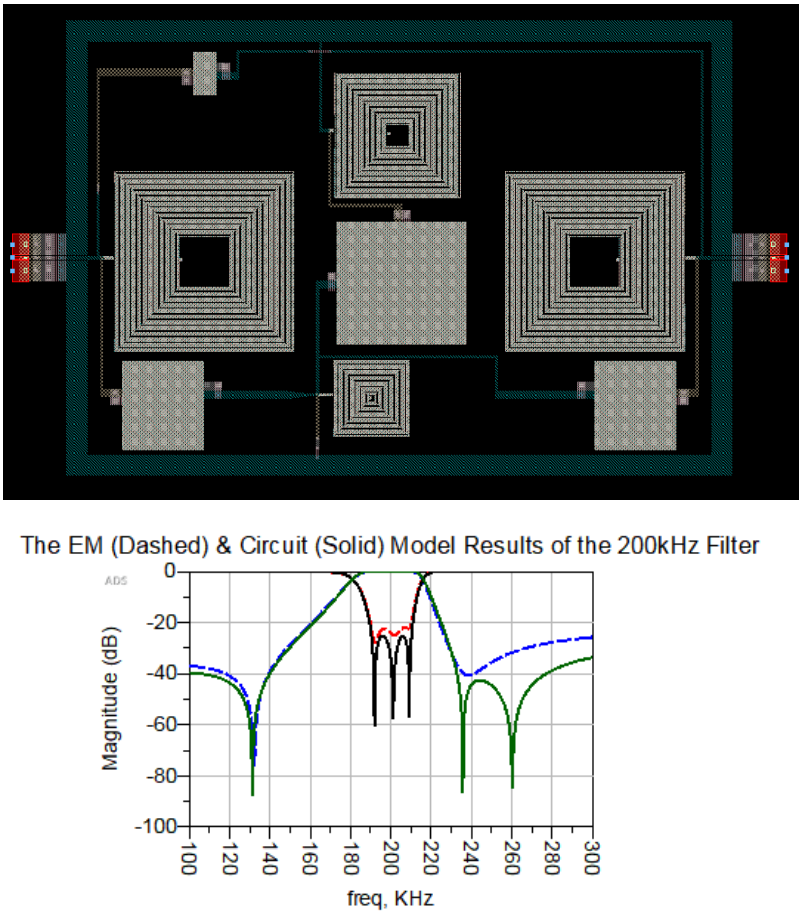


Figure 4.24: The EM model and simulation results of the 200kHz filter.

## 4.5 High-Q Slotline Filter

The use of lumped elements in superconducting filter design is ideal for lower frequency applications, but the quality begins to degrade as the frequency of operation increases. Therefore, it is important to consider other types of filters in order to maintain an accept-

able Q-factor at higher frequencies.

At mmWave frequencies, slotline technology becomes an interesting choice for the design of filters. This planar structure provides a higher Q compared to its microstrip counterparts when the dimensions are similar [58]. The energy stored in a slotline resonator is concentrated over a larger volume, and the current flow occurs across a wider area. These two characteristics provide lower ohmic losses within the circuit.

### 4.5.1 Resonator and I/O Coupling Design

The use of slotline architecture requires careful consideration when designing the resonator and input/output coupling. The use of double spiral inductors is used in [58]] to design slotline filters with a 5% and 3% bandwidth and introduces an effective method for I/O coupling in slotlines. [37] uses double spiral inductors and interdigital capacitors to design superconducting microstrip filters. The microstrip structure introduced in [37] can be easily translated to slotline and used as an effective and high-Q resonator, while the capacitive I/O coupling from [58] is used to couple the input CPW line to the filter.

The structure of the resonator can be seen in Figure 4.25. The embedded resonator structure includes both the double spiral inductor and the interdigital capacitor. The resonant frequency of the structure can easily be adjusted by changing the lengths of the capacitor

legs and sizes of the spirals. This structure provides significant flexibility when choosing resonant frequency.

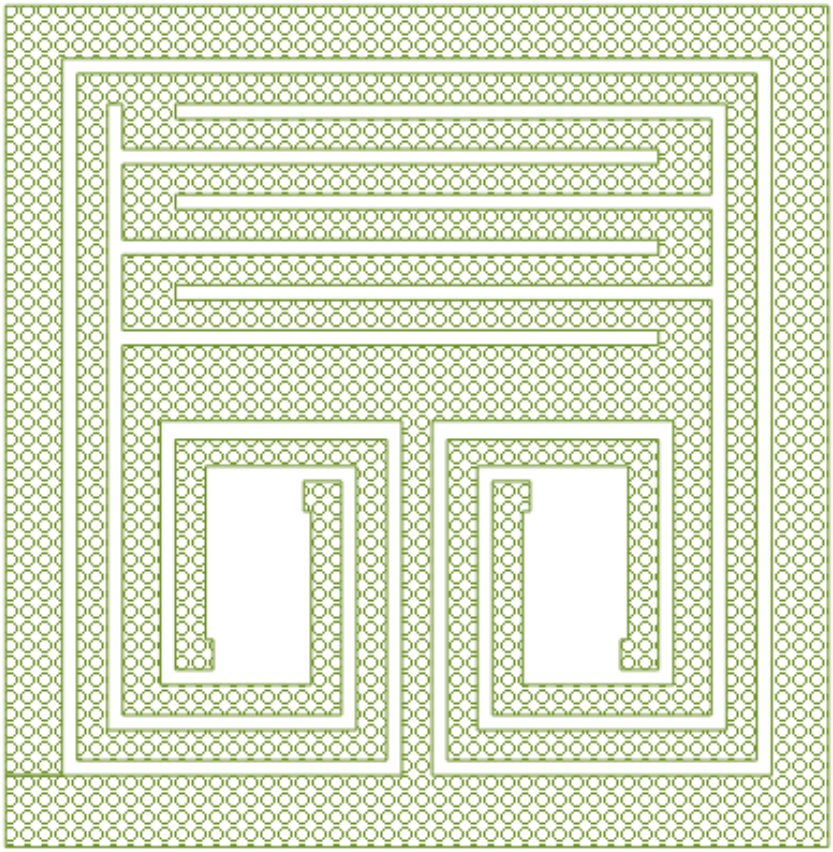

Figure 4.25: The model of the slotline resonator.

The I/O coupling is realized through an interdigital capacitor that allows for a transition between CPW and slotline. The I/O coupling structure can be seen in Figure 4.26. Here, the length of the legs and number of capacitor fingers can be changed to adjust the strength

of the coupling.

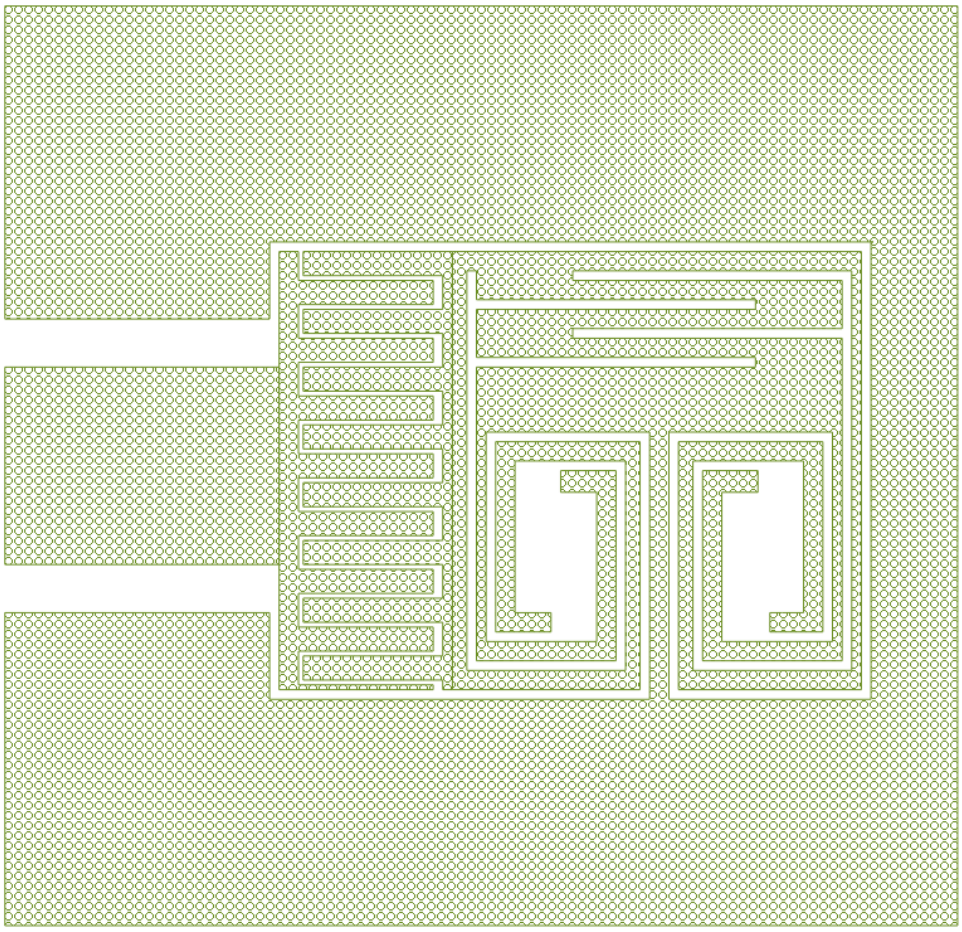

Figure 4.26: The model of the slotlines I/O coupling structure.

### 4.5.2 Slotline Filter Design and Simulation Results

With the resonator and I/O coupling structure, a 6-pole 10% bandwidth slotline filter can be realized using MIT-LL's 8-layer process. The first step is to create an ideal model

for this filter, which can be done in ADS. Figure 4.27 highlights the ADS model and the circuit simulation results. The corresponding N+2 x N+2 coupling matrix values can be seen below. The inter-resonator coupling is achieved by adjusting the spacing between two adjacent resonators, while also flipping them vertically by $180^o$. The RGD technique is used at each stage to tune the filter in order to obtain an ideal response.

$$\begin{pmatrix} 0 & 1.218 & 0 & 0 & 0 & 0 & 0 & 0 \\ 1.218 & 0 & 0.9405 & 0 & 0 & 0 & 0 & 0 \\ 0 & 0.9405 & 0 & 0.648 & 0 & 0 & 0 & 0 \\ 0 & 0 & 0.648 & 0 & 0.612 & 0 & 0 & 0 \\ 0 & 0 & 0 & 0.612 & 0 & 0.648 & 0 & 0 \\ 0 & 0 & 0 & 0 & 0.648 & 0 & 0.9405 & 0 \\ 0 & 0 & 0 & 0 & 0 & 0.9405 & 0 & 1.218 \\ 0 & 0 & 0 & 0 & 0 & 0 & 1.218 & 0 \end{pmatrix}$$

The EM model created in Sonnet is shown in Figure 4.28, and the simulation results are compared to the ideal response and shown in Figure 4.29. The response shows a slightly wider bandwidth than expected but a simulated Q-factor of approximately 620.

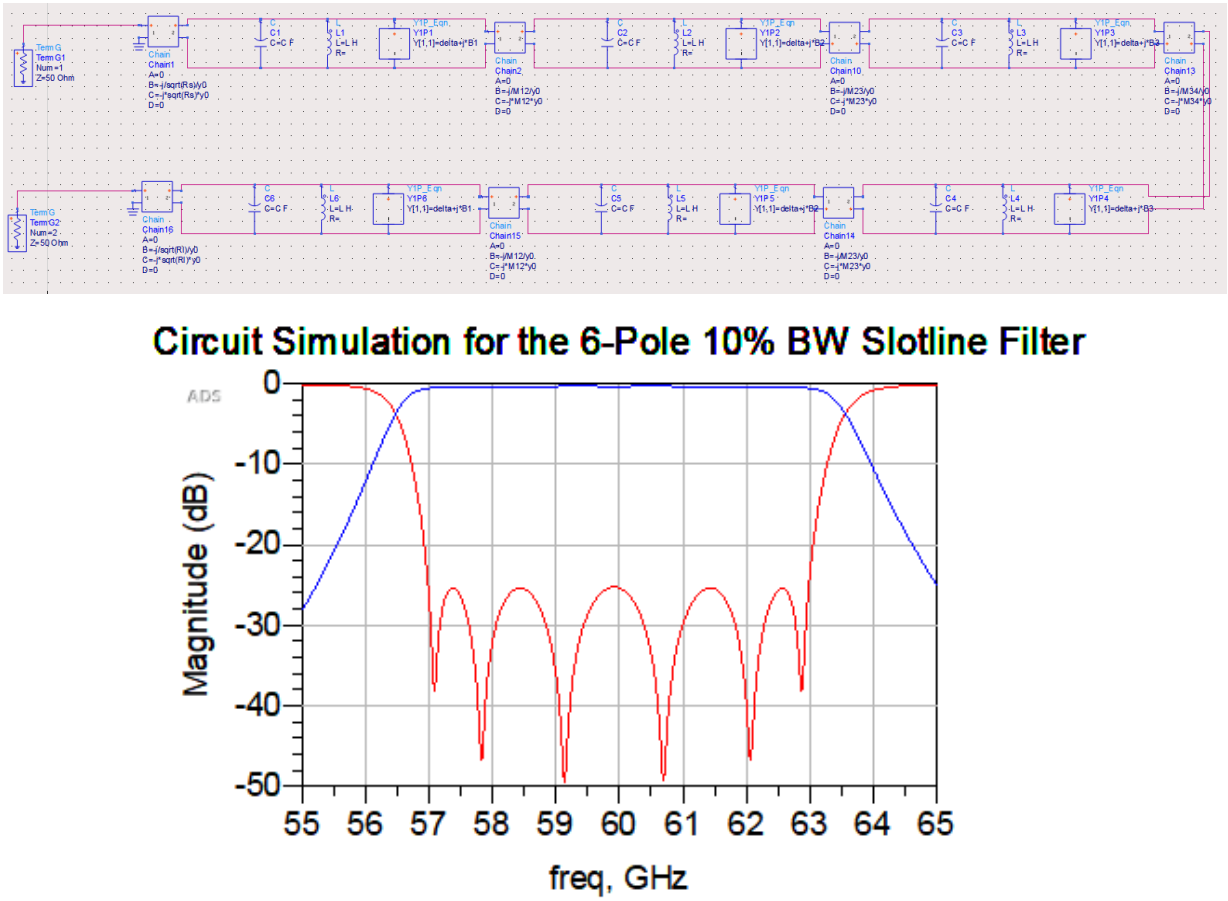


Figure 4.27: The circuit model and results of the slotline filter.

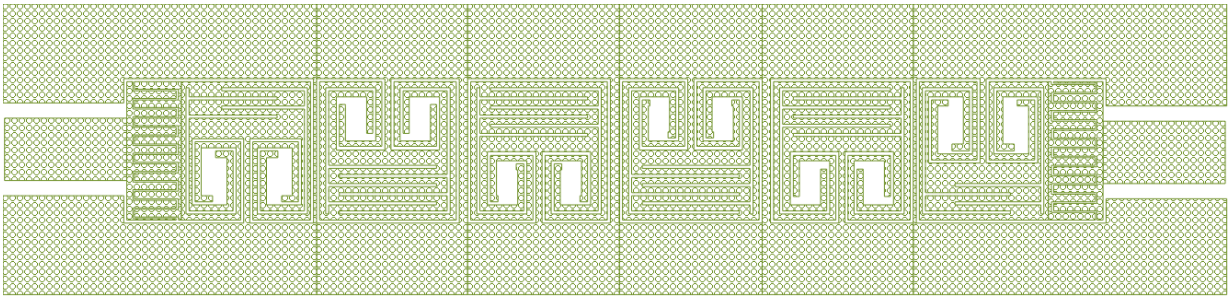

Figure 4.28: The full EM model of the slotline filter.

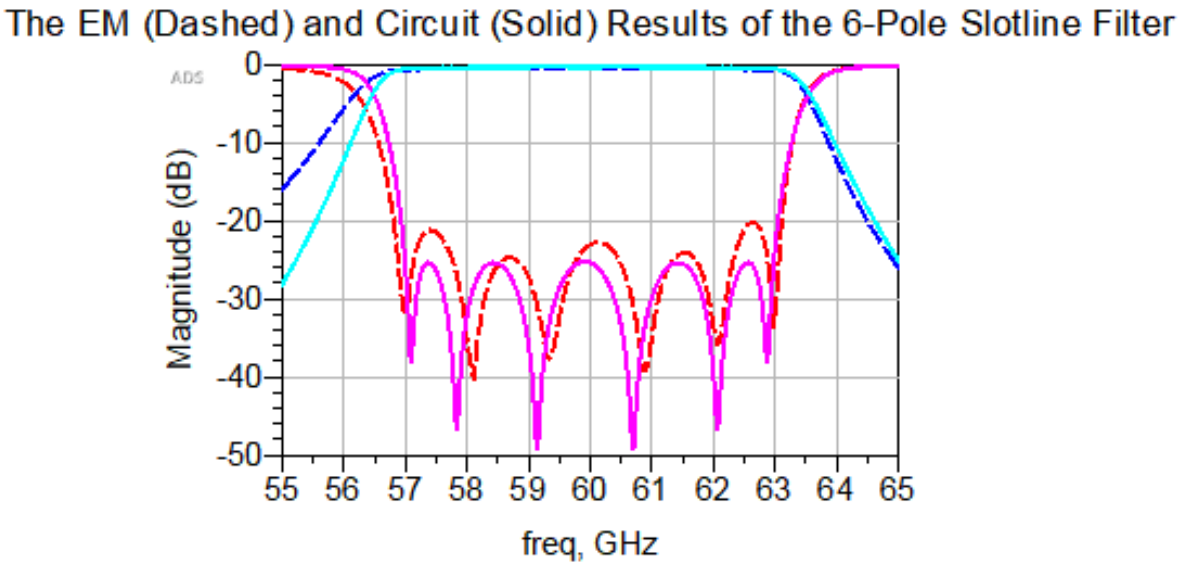


Figure 4.29: The EM results of the slotline filter compared to the ideal circuit simulator results.

# Chapter 5

# Conclusion

The first part of this research explored the process for designing SIW filters. This process highlighted several design methods and compared the results of each. The Hybrid Method was used to design a 4-pole 4GHz quasi-elliptic SIW filter with a bandwidth of 4.2% and then a 5% 8-pole dual-band SIW filter. The negative couplings required to realize both filters were implemented by etching CPW lines from one resonator to another. These filters were also measured, and it was found that implementing the cross-coupling method successfully introduces transmission zeros near the passband. An investigation into an apparent error in the measurements of the dual-band filter was conducted and determined that neither the EM simulation setup nor the design method was the likely source. It is believed that the issue occurred due to an error in manufacturing, more specifically, because

of the use of the wrong dielectric or a highly defective batch of Rogers4003C material. The application of these filters on PCB technology highlights the ability to implement higher Q structures in planar technology.

In the second part of this work, the design of lower-frequency (KHz and MHz) superconducting lumped element filters using the MIT-LL's 4-layer process was explored. Concerns emerged about Sonnet and HFSS's ability to simulate devices at such a low frequency, as it was found that Sonnet could not accurately simulate the value of inductors, and HFSS required extremely long simulation times. We elected, therefore, to use Momentum as our simulator, although, unlike Sonnet, it cannot incorporate kinetic inductance. Several miniaturization techniques were used, such as stacked spiral inductors and capacitors, to design a 2 MHz 3-pole 10% BW lumped-element filter. The spiral inductors were modelled in Sonnet, but the values were simulated in Momentum. No measurements were made for this filter.

We used MIT-LL's 4-layer process to design a 200 KHz lumped-element 3-pole bandpass filter with 10% BW, and found that for filters at this low of frequency, the elements, especially capacitors, are fairly large. With MIT-LL's strict space restrictions, a filter with such large components required miniaturization techniques well beyond stacked spiral inductors and capacitors. The chosen method of miniaturization provides a theoretical size that is 58% smaller than the general Chebyshev structure and 28% smaller than the next

smallest topology presented. This filter was designed in Momentum, but no measurements have been made.

In this thesis, the possibility of using slotline as an architecture for superconducting circuits was explored by presenting a dual-spiral and interdigital capacitor slotline resonator along with a capacitive coupling technique to couple CPW to slotline. The inter-resonator coupling was achieved by changing the spacing between two resonators. Finally, Sonnet and MIT-LL's 8-layer process was used to design a 60GHz 6-pole 10% BW filter.

# References

[1] X.-P. Chen and K. Wu, "Substrate integrated waveguide filter: Basic design rules and fundamental structure features," *IEEE Microwave Magazine*, vol. 15, no. 5, pp. 108–116, 2014.

[2] R. J. Cameron, C. M. Kudsia, and R. R. Mansour, *Microwave filters for communication systems: fundamentals, design, and applications*. John Wiley & Sons, 2018.

[3] S. K. Tolpygo, V. Bolkhovsky, T. J. Weir, C. J. Galbraith, L. M. Johnson, M. A. Gouker, and V. K. Semenov, "Inductance of circuit structures for mit ll superconductor electronics fabrication process with 8 niobium layers," *IEEE Transactions on Applied Superconductivity*, vol. 25, no. 3, pp. 1–5, 2015.

[4] MIT Lincoln Labs, 2022 [Online].

[5] G. Venanzoni, D. Mencarelli, A. Morini, M. Farina, and F. Prudenzano, "Review of substrate integrated waveguide circuits for beam-forming networks working in x-band," *Applied Sciences*, vol. 9, p. 1003, 03 2019.

[6] D. Deslandes and K. Wu, "Integrated microstrip and rectangular waveguide in planar form," *IEEE Microwave and Wireless Components Letters*, vol. 11, no. 2, pp. 68–70, 2001.

[7] X. Chen, W. Hong, T. Cui, J. Chen, and K. Wu, "Substrate integrated waveguide (siw) linear phase filter," *IEEE Microwave and Wireless Components Letters*, vol. 15, no. 11, pp. 787–789, 2005.

[8] S. S. Sabri, B. H. Ahmad, and A. R. B. Othman, "A review of substrate integrated waveguide (siw) bandpass filter based on different method and design," in *2012 IEEE Asia-Pacific Conference on Applied Electromagnetics (APACE)*, pp. 210–215, 2012.

[9] T. Martin, A. Ghiotto, T.-P. Vuong, K. Wu, and F. Lotz, "Compact quasi-elliptic and highly selective afsiw filter with multilayer cross-coupling," in *2019 IEEE MTT-S International Microwave Symposium (IMS)*, pp. 718–721, 2019.

[10] M. F. Hagag, R. Zhang, and D. Peroulis, "High-performance tunable narrowband siw cavity-based quadrature hybrid coupler," *IEEE Microwave and Wireless Components Letters*, vol. 29, no. 1, pp. 41–43, 2019.

[11] T. Djerafi and K. Wu, "Super-compact substrate integrated waveguide cruciform directional coupler," *IEEE Microwave and Wireless Components Letters*, vol. 17, no. 11, pp. 757–759, 2007.

[12] L.-R. Tan, R.-X. Wu, and Y. Poo, "Magnetically reconfigurable siw antenna with tunable frequencies and polarizations," *IEEE Transactions on Antennas and Propagation*, vol. 63, no. 6, pp. 2772–2776, 2015.

[13] Y. Ding and K. Wu, "A 4 × 4 ridge substrate integrated waveguide (rsiw) slot array antenna," *IEEE Antennas and Wireless Propagation Letters*, vol. 8, pp. 561–564, 2009.

[14] Y. Cassivi, L. Perregrini, P. Arcioni, M. Bressan, K. Wu, and G. D. I. Conciauro, "Dispersion characteristics of substrate integrated rectangular waveguide," *IEEE Microwave and Wireless Components Letters*, vol. 12, pp. 333–335, 2002.

[15] F. Xu and K. Wu, "Guided-wave and leakage characteristics of substrate integrated waveguide," *IEEE Transactions on Microwave Theory and Techniques*, vol. 53, no. 1, pp. 66–73, 2005.

[16] L. Yan, W. Hong, G. Hua, J. Chen, K. Wu, and T. J. Cui, "Simulation and experiment on siw slot array antennas," *IEEE Microwave and Wireless Components Letters*, vol. 14, no. 9, pp. 446–448, 2004.

[17] M. Salehi and E. Mehrshahi, "A closed-form formula for dispersion characteristics of fundamental siw mode," *IEEE Microwave and Wireless Components Letters*, vol. 21, no. 1, pp. 4–6, 2011.

[18] W. Che, K. Deng, D. Wang, and Y. Chow, "Analytical equivalence between substrate-integrated waveguide and rectangular waveguide," *IET microwaves, antennas & propagation*, vol. 2, no. 1, pp. 35–41, 2008.

[19] Z. Kordiboroujeni and J. Bornemann, "Designing the width of substrate integrated waveguide structures," *IEEE Microwave and Wireless Components Letters*, vol. 23, no. 10, pp. 518–520, 2013.

[20] D. Deslandes, "Design equations for tapered microstrip-to-substrate integrated waveguide transitions," in *2010 IEEE MTT-S International Microwave Symposium*, pp. 704–707, 2010.

[21] B. Kunooru, S. V. Nandigama, D. Rama Krishna, R. Gugulothu, and S. Bhalke, "Studies on microstrip to siw transition at ka-band," in *2019 TEQIP III Sponsored International Conference on Microwave Integrated Circuits, Photonics and Wireless Networks (IMICPW)*, pp. 379–382, 2019.

[22] Z. Kordiboroujeni and J. Bornemann, "New wideband transition from microstrip line to substrate integrated waveguide," *IEEE Transactions on Microwave Theory and Techniques*, vol. 62, no. 12, pp. 2983–2989, 2014.

[23] X.-P. Chen and K. Wu, "Substrate integrated waveguide cross-coupled filter with negative coupling structure," *IEEE Transactions on Microwave Theory and Techniques*, vol. 56, no. 1, pp. 142–149, 2008.

[24] F. Taringou, D. Dousset, J. Bornemann, and K. Wu, "Substrate-integrated waveguide transitions to planar transmission-line technologies," in *2012 IEEE/MTT-S International Microwave Symposium Digest*, pp. 1–3, 2012.

[25] D. Lorente, M. Limbach, H. Esteban, and V. Boria, "Compact ultrawideband grounded coplanar waveguide to substrate integrated waveguide tapered v-slot transition," *IEEE Microwave and Wireless Components Letters*, vol. 30, no. 12, pp. 1137–1140, 2020.

[26] L. Li, X. Chen, R. Khazaka, and K. Wu, "A transition from substrate integrated waveguide (siw) to rectangular waveguide," in *2009 Asia Pacific Microwave Conference*, pp. 2605–2608, 2009.

[27] R. Vincenti Gatti, R. Rossi, and M. Dionigi, "Broadband right-angle rectangular waveguide to substrate integrated waveguide transition with distributed impedance matching network," *Applied Sciences*, vol. 9, p. 389, 01 2019.

[28] L. Szydlowski, N. Leszczynska, A. Lamecki, and M. Mrozowski, "A substrate integrated waveguide (siw) bandpass filter in a box configuration with frequency-dependent coupling," *IEEE Microwave and Wireless Components Letters*, vol. 22, no. 11, pp. 556–558, 2012.

[29] F. Mira, J. Mateu, S. Cogollos, and V. E. Boria, "Design of ultra-wideband substrate integrated waveguide (siw) filters in zigzag topology," *IEEE Microwave and Wireless Components Letters*, vol. 19, no. 5, pp. 281–283, 2009.

[30] H. Miyake, S. Kitazawa, T. Ishizaki, T. Yamada, and Y. Nagatomi, "A miniaturized monolithic dual band filter using ceramic lamination technique for dual mode portable telephones," in *1997 IEEE MTT-S International Microwave Symposium Digest*, vol. 2, pp. 789–792 vol.2, 1997.

[31] L. Zhu, R. R. Mansour, and M. Yu, "Triple-band dielectric resonator bandpass filters," in *2017 IEEE MTT-S International Microwave Symposium (IMS)*, pp. 745–747, 2017.

[32] A. M. Abu-Hudrouss, A. B. Jayyousi, and M. J. Lancaster, "Triple-band hts filter using dual spiral resonators with capacitive-loading," *IEEE Transactions on Applied Superconductivity*, vol. 18, no. 3, pp. 1728–1732, 2008.

[33] H.-W. Wu and R.-Y. Yang, "A new quad-band bandpass filter using asymmetric stepped impedance resonators," *IEEE Microwave and Wireless Components Letters*, vol. 21, no. 4, pp. 203–205, 2011.

[34] X. Guo, L. Zhu, and W. Wu, "Design method for multiband filters with compact configuration in substrate integrated waveguide," *IEEE Transactions on Microwave Theory and Techniques*, vol. 66, no. 6, pp. 3011–3018, 2018.

[35] J. Lee, M. S. Uhm, and I.-B. Yom, "A dual-passband filter of canonical structure for satellite applications," *IEEE Microwave and Wireless Components Letters*, vol. 14, no. 6, pp. 271–273, 2004.

[36] Laforge, Paul, *Tunable Superconducting Microwave Filters.* PhD thesis, 2010.

[37] J. Zhou, M. Lancaster, and F. Huang, "Superconducting microstrip filters using compact resonators with double-spiral inductors and interdigital capacitors," in *IEEE MTT-S International Microwave Symposium Digest, 2003*, vol. 3, pp. 1889–1892 vol.3, 2003.

[38] P. D. Laforge, R. R. Mansour, and M. Yu, "Reconfigurable mems-based bpf for manifold-coupled-superconducting triplexers," *IEEE Transactions on Applied Superconductivity*, vol. 28, no. 6, pp. 1–8, 2018.

[39] M. J. Lancaster, *Passive Microwave Device Applications of High-Temperature Superconductors*. Cambridge University Press, 1997.

[40] M. Lancaster, F. Huang, A. Porch, B. Avenhaus, J.-S. Hong, and D. Hung, "Miniature superconducting filters," *IEEE Transactions on Microwave Theory and Techniques*, vol. 44, no. 7, pp. 1339–1346, 1996.

[41] Jia, Huayong, *High-Q Millimeter Wave RF Filters and Multiplexers*. PhD thesis, 2021.

[42] J. Zhou, M. Lancaster, and F. Huang, "Superconducting microstrip filters using compact resonators with double-spiral inductors and interdigital capacitors," in *IEEE MTT-S International Microwave Symposium Digest, 2003*, vol. 3, pp. 1889–1892 vol.3, 2003.

[43] Keysight, 2022 [Online].

[44] Ansys, 2022 [Online].

[45] X.-P. Chen, K. Wu, and D. Drolet, "Substrate integrated waveguide filter with improved stopband performance for satellite ground terminal," *IEEE Transactions on Microwave Theory and Techniques*, vol. 57, no. 3, pp. 674–683, 2009.

[46] Sonnet, 2022 [Online].

[47] Keysight, 2022 [Online].

[48] Simulia, 2022 [Online].

[49] J. Ness, "A unified approach to the design, measurement, and tuning of coupled-resonator filters," *IEEE Transactions on Microwave Theory and Techniques*, vol. 46, no. 4, pp. 343–351, 1998.

[50] R. N. Das, V. Bolkhovsky, S. K. Tolpygo, P. Gouker, L. M. Johnson, E. A. Dauler, and M. A. Gouker, "Large scale cryogenic integration approach for superconducting high-performance computing," in *2017 IEEE 67th Electronic Components and Technology Conference (ECTC)*, pp. 675–683, 2017.

[51] D. Pozar, *Microwave Engineering, 4th Edition*. Wiley, 2011.

[52] A. Zolfaghari, A. Chan, and B. Razavi, "Stacked inductors and transformers in cmos technology," *IEEE Journal of Solid-State Circuits*, vol. 36, no. 4, pp. 620–628, 2001.

[53] M. Geen, G. Green, R. Arnold, J. Jenkins, and R. Jansen, "Miniature multilayer spiral inductors for gaas mmics," in *11th Annual Gallium Arsenide Integrated Circuit (GaAs IC) Symposium*, pp. 303–306, 1989.

[54] S. Mohan, M. del Mar Hershenson, S. Boyd, and T. Lee, "Simple accurate expressions for planar spiral inductances," *IEEE Journal of Solid-State Circuits*, vol. 34, no. 10, pp. 1419–1424, 1999.

[55] Stanford Microwave Integrated Circuits Laboratory, 2022 [Online].

[56] Setoodeh, Sormeh, "Superconducting microwave filters," Master's thesis, 2011.

[57] P. D. Laforge, R. R. Mansour, and M. Yu, "The design of miniaturized superconducting filters with the reflected group delay method," *IEEE Transactions on Applied Superconductivity*, vol. 20, no. 4, pp. 2265–2271, 2010.

[58] R. Azadegan and K. Sarabandi, "Miniature high-q double-spiral slot-line resonator filters," *IEEE Transactions on Microwave Theory and Techniques*, vol. 52, no. 5, pp. 1548–1557, 2004.

# APPENDICES

# Appendix A

Table A.1: The K-impedance method table for the 4GHz quasi-elliptic filter.

| Iris Width (mm) | $Z_{11}$ | $Z_{12}$ | $X_s$ | $X_p$ | $\phi$ | K |
|---|---|---|---|---|---|---|
| 11.314 | 0.345351 | 0.171833 | 0.173518 | 0.171833 | -0.6491 | 0.1539 |
| 11.514 | 0.35761 | 0.182448 | 0.175162 | 0.182448 | -0.6686 | 0.1623 |
| 12.114 | 0.396083 | 0.217412 | 0.178671 | 0.217412 | -0.7271 | 0.1889 |
| 12.314 | 0.411251 | 0.230807 | 0.180444 | 0.230807 | -0.7493 | 0.1987 |
| 15.314 | 0.755207 | 0.555616 | 0.199591 | 0.555616 | -1.1161 | 0.3776 |
| 15.714 | 0.829805 | 0.627744 | 0.202061 | 0.627744 | -1.1676 | 0.4057 |
| 15.914 | 0.871296 | 0.668069 | 0.203227 | 0.668069 | -1.1952 | 0.4194 |
| 16.314 | 0.964146 | 0.758475 | 0.205671 | 0.758475 | -1.2477 | 0.4478 |
| 16.914 | 1.133159 | 0.924202 | 0.208957 | 0.924202 | -1.3244 | 0.4907 |
| 17.114 | 1.198534 | 0.988858 | 0.209676 | 0.988858 | -1.3487 | 0.505 |
| 17.314 | 1.2722 | 1.061075 | 0.211125 | 1.061075 | -1.3742 | 0.5194 |
| 19.314 | 2.694 | 2.4732 | 0.2208 | 2.4732 | -1.5969 | 0.6568 |
| 21.314 | 18.490332 | 18.264198 | 0.226134 | 18.264198 | -1.766 | 0.7771 |

Table A.2: The K-impedance method table for the 4GHz quasi-elliptic filter (finding $iris_3$ when $L_2 = 22.96$mm) .

| Iris Width (mm) | $Z_{11}$ | $Z_{12}$ | $X_s$ | $X_p$ | $\phi$ | K |
|---|---|---|---|---|---|---|
| 6.96 | 0.196976 | 0.035368 | 0.161608 | 0.035368 | -0.3885 | 0.034 |
| 8.96 | 0.253109 | 0.077749 | 0.17536 | 0.077749 | -0.4931 | 0.0731 |
| 10.96 | 0.347407 | 0.158131 | 0.189276 | 0.158131 | -0.6551 | 0.1414 |
| 11.36 | 0.374204 | 0.181619 | 0.192585 | 0.181619 | -0.6976 | 0.1599 |
| 11.56 | 0.388413 | 0.194386 | 0.194027 | 0.194386 | -0.7193 | 0.1696 |

Table A.3: The eigenmode analysis table for the 4GHz quasi-elliptic filter.

| Iris Width (mm) | $f_e(GHz)$ | $f_m(GHz)$ | $k_e$ | M |
|---|---|---|---|---|
| 10.484 | 4.251582 | 4.0762727 | 0.042083262 | 0.673332199 |
| 11.284 | 4.2403352 | 4.021134333 | 0.053028498 | 0.848455963 |
| 11.884 | 4.237018415 | 3.987613624 | 0.060592537 | 0.969480593 |
| 11.984 | 4.236463517 | 3.981846315 | 0.061903979 | 0.990463658 |
| 12.084 | 4.2357 | 3.975845 | 0.063226844 | 1.011629509 |
| 12.284 | 4.23491 | 3.963256003 | 0.066199209 | 1.059187337 |

Table A.4: The eigenmode analysis table for the 4GHz quasi-elliptic filter for the hybrid method (finding $iris_3$ when $L_2 = 22.96$).

| Iris Width (mm) | $f_e(GHz)$ | $f_m(GHz)$ | $k_e$ | M |
|---|---|---|---|---|
| 12.2 | 4.411191015 | 4.199522558 | 0.049134285 | 0.786148564 |
| 12.6 | 4.40923807 | 4.178081124 | 0.05379783 | 0.860765286 |

Table A.5: The K-impedance method table for the 10GHz dualband filter.

| Iris Width (mm) | $Z_{11}$ | $Z_{12}$ | $X_s$ | $X_p$ | $\phi$ | K |
|---|---|---|---|---|---|---|
| 0 | 0.149413 | 0 | 0.149413 | 0 | -0.2966 | 0 |
| 3.62 | 0.295785 | 0.081851 | 0.213934 | 0.081851 | -0.5718 | 0.0753 |
| 3.66 | 0.299059 | 0.084849 | 0.21421 | 0.084849 | -0.5776 | 0.0779 |
| 3.7 | 0.303967 | 0.088108 | 0.215859 | 0.088108 | -0.5863 | 0.0807 |
| 3.82 | 0.316063 | 0.097993 | 0.21807 | 0.097993 | -0.6073 | 0.0892 |
| 4.22 | 0.364509 | 0.137764 | 0.226745 | 0.137764 | -0.6884 | 0.1218 |
| 4.62 | 0.421748 | 0.188593 | 0.233155 | 0.188593 | -0.7771 | 0.1608 |
| 4.66 | 0.428801 | 0.194647 | 0.234154 | 0.194647 | -0.7875 | 0.1652 |
| 4.78 | 0.450117 | 0.213642 | 0.236475 | 0.213642 | -0.8182 | 0.1788 |
| 4.82 | 0.457923 | 0.2204 | 0.237523 | 0.2204 | -0.8292 | 0.1834 |
| 5.42 | 0.596977 | 0.348012 | 0.248965 | 0.348012 | -1.0011 | 0.2623 |
| 5.54 | 0.633078 | 0.381439 | 0.251639 | 0.381439 | -1.0391 | 0.28 |
| 5.58 | 0.645274 | 0.393043 | 0.252231 | 0.393043 | -1.0513 | 0.286 |
| 5.62 | 0.658303 | 0.405294 | 0.253009 | 0.405294 | -1.064 | 0.2921 |
| 5.82 | 0.741029 | 0.481338 | 0.259691 | 0.481338 | -1.1392 | 0.3264 |
| 5.86 | 0.755947 | 0.495673 | 0.260274 | 0.495673 | -1.1513 | 0.3325 |

| | | | | | | |
|---|---|---|---|---|---|---|
| 6.02 | 0.823579 | 0.560546 | 0.263033 | 0.560546 | -1.2024 | 0.3582 |
| 6.62 | 1.183306 | 0.912387 | 0.270919 | 0.912387 | -1.3901 | 0.4592 |
| 6.82 | 1.363792 | 1.090248 | 0.273544 | 1.090248 | -1.4509 | 0.4935 |
| 6.86 | 1.40518 | 1.13097 | 0.27421 | 1.13097 | -1.4628 | 0.5002 |
| 6.9 | 1.450391 | 1.175548 | 0.274843 | 1.175548 | -1.4752 | 0.5072 |
| 7.02 | 1.594963 | 1.319744 | 0.275219 | 1.319744 | -1.5089 | 0.5281 |
| 7.22 | 1.905327 | 1.627302 | 0.278025 | 1.627302 | -1.5661 | 0.5618 |
| 7.82 | 4.01349 | 3.7291 | 0.28439 | 3.7291 | -1.7194 | 0.6589 |
| 8.02 | 5.969063 | 5.682744 | 0.286319 | 5.682744 | -1.764 | 0.6888 |
| 8.22 | 11.014487 | 10.728155 | 0.286332 | 10.728155 | -1.8037 | 0.7184 |

Table A.6: The eigenmode analysis table for the 10GHz dualband filter filter for the hybrid method (finding $Iris_{36}$ when $L_3 = 9.46mm$).

| Iris Width (mm) | $f_e(GHz)$ | $f_m(GHz)$ | $k_e$ | M |
|---|---|---|---|---|
| 1.46 | 10.6811538 | 10.62603383 | 0.005173803 | 0.103476068 |
| 3.46 | 10.64228557 | 10.43655316 | 0.01951842 | 0.3903684 |
| 3.86 | 10.63081334 | 10.35277145 | 0.026496243 | 0.52992485 |
| 5.46 | 10.59447565 | 9.898396971 | 0.067855446 | 1.357108911 |

# Appendix B

Table B.1: Coefficients for the modified wheeler expression. [54]

| Layout | $K_1$ | $K_2$ |
|---|---|---|
| Square | 2.34 | 2.75 |
| Hexagonal | 2.33 | 3.82 |
| Octagonal | 2.25 | 3.55 |

Table B.2: Coefficients for the current sheet expression. [54]

| Layout | $c_1$ | $c_2$ | $c_3$ | $c_4$ |
|---|---|---|---|---|
| Square | 1.27 | 2.07 | 0.18 | 0.13 |
| Hexagonal | 1.09 | 2.23 | 0 | 0.17 |
| Octagonal | 1.07 | 2.29 | 0 | 0.19 |
| Circle | 1 | 2.46 | 0 | 0.2 |

Table B.3: Coefficients for the data-fitted monomial expression. [54]

| Layout | $\beta$ | $\alpha_1(d_{out})$ | $\alpha_2(\omega)$ | $\alpha_3(d_{avg})$ | $\alpha_4(n)$ | $\alpha_5(s)$ |
|---|---|---|---|---|---|---|
| Square | $1.62 * 10^{-3}$ | -1.21 | -0.147 | 2.40 | 1.78 | -0.030 |
| Hexagonal | $1.28 * 10^{-3}$ | -1.24 | -0.174 | 2.47 | 1.77 | -0.049 |
| Octagonal | $1.33 * 10^{-3}$ | -1.21 | -0.163 | 2.43 | 1.75 | -0.049 |